Numéro d'ordre : Année 2012

THÈSE

présentée devant

L'Institut National des Sciences Appliquées de Lyon

pour obtenir

LE GRADE DE DOCTEUR

ÉCOLE DOCTORALE : ÉLECTRONIQUE, ÉLECTROTECHNIQUE, AUTOMATIQUE
FORMATION DOCTORALE : SCIENCES DE L'INFORMATION, DES DISPOSITIFS ET DES SYSTÈMES

par

Ting LI

Contributions to Mean Shift filtering and segmentation, Applications to MRI ischemic data

Jury :

Philippe Bolon	Professeur (LISTIC, Annecy)	Président
Marlène Wiart	Chargé de Recherche (CNRS)	Examinateur
Ludovic Macaire	Professeur (LAGIS, Lille)	Rapporteur
Pierre Gouton	Professeur (Le2i, Dijon)	Rapporteur
Thomas Grenier	Maître de Conférences (INSA de lyon)	Co-directeur de thèse
Hugues Benoit-Cattin	Professeur (INSA de lyon)	Directeur de thèse

INSA Direction de la Recherche - Ecoles Doctorales – Quinquennal 2011-2015

SIGLE	ECOLE DOCTORALE	NOM ET COORDONNEES DU RESPONSABLE
CHIMIE	**CHIMIE DE LYON** **http://www.edchimie-lyon.fr** Insa : R. GOURDON	M. Jean Marc LANCELIN Université de Lyon – Collège Doctoral Bât ESCPE 43 bd du 11 novembre 1918 69622 VILLEURBANNE Cedex Tél : 04.72.43 13 95 directeur@edchimie-lyon.fr
E.E.A.	**ELECTRONIQUE, ELECTROTECHNIQUE, AUTOMATIQUE** **http://edeea.ec-lyon.fr** Secrétariat : M.C. HAVGOUDOUKIAN eea@ec-lyon.fr	M. Gérard SCORLETTI Ecole Centrale de Lyon 36 avenue Guy de Collongue 69134 ECULLY Tél : 04.72.18 60 97 Fax : 04 78 43 37 17 Gerard.scorletti@ec-lyon.fr
E2M2	**EVOLUTION, ECOSYSTEME, MICROBIOLOGIE, MODELISATION** **http://e2m2.universite-lyon.fr** Insa : H. CHARLES	Mme Gudrun BORNETTE CNRS UMR 5023 LEHNA Université Claude Bernard Lyon 1 Bât Forel 43 bd du 11 novembre 1918 69622 VILLEURBANNE Cédex Tél : 04.72.43.12.94 e2m2@biomserv.univ-lyon1.fr
EDISS	**INTERDISCIPLINAIRE SCIENCES-SANTE** **http://ww2.ibcp.fr/ediss** Sec : Safia AIT CHALAL Insa : M. LAGARDE	M. Didier REVEL Hôpital Louis Pradel Bâtiment Central 28 Avenue Doyen Lépine 69677 BRON Tél : 04.72.68 49 09 Fax :04 72 35 49 16 Didier.revel@creatis.uni-lyon1.fr
INFOMATHS	**INFORMATIQUE ET MATHEMATIQUES** http://infomaths.univ-lyon1.fr	M. Johannes KELLENDONK Université Claude Bernard Lyon 1 INFOMATHS Bâtiment Braconnier 43 bd du 11 novembre 1918 69622 VILLEURBANNE Cedex Tél : 04.72. 44.82.94 Fax 04 72 43 16 87 infomaths@univ-lyon1.fr
Matériaux	**MATERIAUX DE LYON** Secrétariat : M. LABOUNE PM : 71.70 –Fax : 87.12 Bat. Saint Exupéry Ed.materiaux@insa-lyon.fr	M. Jean-Yves BUFFIERE INSA de Lyon MATEIS Bâtiment Saint Exupéry 7 avenue Jean Capelle 69621 VILLEURBANNE Cédex Tél : 04.72.43 83 18 Fax 04 72 43 85 28 Jean-yves.buffiere@insa-lyon.fr
MEGA	**MECANIQUE, ENERGETIQUE, GENIE CIVIL, ACOUSTIQUE** Secrétariat : M. LABOUNE PM : 71.70 –Fax : 87.12 Bat. Saint Exupéry mega@insa-lyon.fr	M. Philippe BOISSE INSA de Lyon Laboratoire LAMCOS Bâtiment Jacquard 25 bis avenue Jean Capelle 69621 VILLEURBANNE Cedex Tél :04.72.43.71.70 Fax : 04 72 43 72 37 Philippe.boisse@insa-lyon.fr
ScSo	**ScSo*** M. OBADIA Lionel Sec : Viviane POLSINELLI Insa : J.Y. TOUSSAINT	M. OBADIA Lionel Université Lyon 2 86 rue Pasteur 69365 LYON Cedex 07 Tél : 04.78.69.72.76 Fax : 04.37.28.04.48 Lionel.Obadia@univ-lyon2.fr

*ScSo : Histoire, Geographie, Aménagement, Urbanisme, Archéologie, Science politique, Sociologie, Anthropologie

Acknowledgments

I would like to acknowledge the following people for their role in the completion of this thesis:

In the first place I would like to thank Hugues Benoit-Cattin for his supervision, advice and guidance from the very early stage of this research. It was always inspirable and fruitful to discuss with you since you always explain difficult concepts in simply way, our meetings are always rich in ideas, jokes and laughs. Thanks for your devotion of time and effort in correcting my innumerable mistakes in this thesis. Thank you for helping me produce a thesis I can be proud of.

My sincere and deeply thanks go to Thomas Grenier, generously accompanying me along this academic path as well as making me more rigorous and more patient. Your meticulous style has always been my study model which direct me from the fur of the image processing into the profound informatics halls. Your patience in teaching and knowledgeable in researching give me endless inspiration. I have been so lucky to have you as co-supervisor. You were always here for me, ready to listen, patient to explain and find solutions.

I gratefully acknowledge Robert Goutte who kindly corrected my langues errors, helped me with discussion and gave me a lot of support. I would like to thank Delfine Charpigny, for incomputable help and concerning over 3 years of sharing an office.

To the role model for hard workers in the lab, Tristan Glatard, I am proud to record that I had several opportunities to work with an exceptionally experienced scientist like him. I would like to thank Sorina Camarasu, for being the first person who taught me how to use EGEE. Many thanks go in particular to Rafael Silva, Sarra Ben Fredj, Ibrahim Kallel, I am so grateful for the work collaboration with you.

To Fabien Chauveau and Tae-Hee Cho, it is a pleasure to collaborate with you. I am thankful for always helping me out in providing medical data and solving my medical problems. I would like to express my deep acknowledgement to Obioma Chigozie Udobata who encourage and help me with the writing and polishing of thesis. I particularly jealous of his ability to learn and his endurance in facing stubborn problems.

This three years of thesis in Creatis have been also very easy because of the ambiance that my colleges, Jean-Loic Rose, Chantal Muller, Muriel Cathaud, etc, brought in this place.

Words fail me to express my appreciation to my boyfriend Senbin Chen whose love, dedication, and persistent confidence in me. Specially, I would like to acknowledge my parents, Luxiang Song, Zhonglin LI, they deserve special mention for their inseparable support and love.

Ting LI

Abstract

Medical studies increasingly use multi-modality imaging, producing multidimensional data that bring additional information that are also challenging to process and interpret. As an example, for predicting salvageable tissue, ischemic studies in which combinations of different multiple MRI imaging modalities (DWI, PWI) were used produced more conclusive results than studies made using a single modality. However, the multi-modality approach necessitates the use of more advanced algorithms to perform otherwise regular image processing tasks such as filtering, segmentation and clustering. A robust method for addressing the problems associated with processing data obtained from multi-modality imaging is *mean shift* which is based on feature space analysis and on non-parametric kernel density estimation and can be used for multi-dimensional filtering, segmentation and clustering.

In this thesis, we sought to optimize the *mean shift* process by analyzing the factors that influence it and optimizing its parameters. We examined the effect of noise and blur in processing the feature space and how *mean shift* can be tuned for optimal de-noising and also to reduce blurring. The large success of *mean shift* is mainly due to the intuitive tuning of bandwidth parameters which describe the scale at which features are analyzed. Based on the univariate Plug In (PI), that is a kernel density estimation bandwidth selectors approach successfully applied to *mean shift* filtering, we propose the use of multi-variate PI for *mean shift* filtering. We assess the interest of using diagonal and full bandwidth matrix with experiment on synthesized and natural images.

We propose a new and automatic volume-based segmentation framework which combines *mean shift* filtering and *region growing* segmentation as well as *probability map* optimization. The framework is theoretically studied using synthesized MRI images. Testing is then extended to real MRI data obtained from rats and humans with the aim of predicting the evolution of the ischemic penumbra several days following the onset of ischemia using only information obtained from the very first scan. The results obtained is an average DICE of 0.8 for the rat MRI image scans and 0.53 for the human MRI image scans; the reference images for both cases are manually segmented

by a team of medical expert. In addition, according to the DICE measurement, the most relevant combination of parameters for the MRI modalities is determined.

Keyword

mean shift filtering, *region growing* segmentation, *probability map*, bandwidth matrix optimization, MRI, ischemia.

Résumé

De plus en plus souvent, les études médicales utilisent simultanément de multiples modalités d'acquisition d'image, produisant ainsi des données multidimensionnelles comportant un grand nombre d'informations dont l'interprétation et le traitement deviennent délicats. Par exemple, les études sur l'ischémie cérébrale, se basant sur la combinaison de plusieurs images IRM provenant de différentes séquences d'acquisition pour prédire l'évolution de la zone nécrosée, donnent de bien meilleurs résultats que celles basées sur une seule image. Ces approches nécessitent cependant la mise en oeuvre d'algorithmes complexes pour réaliser les opérations de filtrage, de segmentation et de classification.

Une des approches robustes pour répondre à ces problèmes de traitements de données multidimensionnelles est le *mean shift*. Cette approche est basée sur l'analyse de l'espace des caractéristiques et l'estimation non-paramétrique par noyau de la densité de probabilité. Dans cette thèse, nous étudions les paramètres qui influencent les résultats du *mean shift* et nous cherchons à optimiser leur choix. Nous examinons notamment l'effet du bruit et du flou dans l'espace des caractéristiques et comment le *mean shift* doit être paramétré pour optimiser le débruitage et la réduction du flou. Le succès du *mean shift* est principalement dû au réglage intuitif de ses paramètres. Ces paramètres représentent l'échelle à laquelle le *mean shift* analyse chacune des dimensions. La méthode du *plug-in* (PI) monodimensionnel est fréquemment utilisée en filtrage *mean shift* pour, dans le cadre de l'estimation non-paramétrique par noyau, approximer le paramètre d'échelle optimal. Nous proposons l'utilisation multidimensionnelle du PI pour le filtrage *mean shift* et nous évaluons l'intérêt des matrices d'échelle diagonales et pleines calculées à partir des règles du PI multidimensionnelle sur des images de synthèses et naturelles.

Enfin, nous proposons une méthode de segmentation automatique et volumique combinant le filtrage *mean shift* et la croissance de région ainsi qu'une optimisation basée sur les cartes de probabilité. Cette approche est d'abord étudiée sur des données synthétiques. Elle est ensuite mise en oeuvre sur des données réelles issues d'études sur l'ischémie cérébrale chez le rat et

l'homme. L'objectif est d'étudier l'efficacité de l'approche proposée à prédire l'évolution de la zone de pénombre plusieurs jours après l'accident vasculaire et ce, à partir des IRM réalisées peu de temps après la survenue de cet accident. Par rapport aux segmentations manuelles réalisées par des experts médicaux plusieurs jours après l'accident, les résultats obtenus sur les données de rats mesurés avec le critère de DICE sont prometteurs (DICE$= 0.8$). Ces mêmes résultats sont plus mitigés sur les données humaines (DICE$= 0.53$). Toujours en utilisant le coefficient DICE, nous déterminons la combinaison d'images IRM conduisant à la meilleure prédiction.

Mots clé

filtrage *mean shift*, segmentation par *croissance de région*, *carte de probabilité*, optimisation matrice d'échelle, IRM, ischémie cérébrale.

Contents

List of figures **xvii**

List of Tables **xix**

I GENERAL INTRODUCTION **1**

1 PhD context and objectives **3**
1.1 Introduction . . . 3
1.2 Structure of the thesis . . . 6

2 Mean Shift and Mean Shift Filtering **9**
2.1 Introduction . . . 9
2.2 *Mean shift* State of the Art . . . 10
2.2.1 History and applications . . . 10
2.2.2 Other Feature Space Filtering Approaches . . . 10
2.3 Feature Space Representation . . . 11
2.4 From Kernel Density to Gradient Density Estimation . . . 12
2.4.1 Probability density function . . . 12
2.4.2 Kernel Density Estimation . . . 13
2.4.3 Choice of kernel . . . 13
2.4.4 Expression of Gradient Density Estimation . . . 14
2.5 *Mean shift* Algorithm . . . 15
2.5.1 Intuitive description of mean shift . . . 15
2.5.2 Theoretical description of mean shift . . . 15
2.6 Procedure of *mean shift* filtering . . . 16
2.7 Procedure of *mean shift* clustering . . . 17
2.7.1 Introduction . . . 17
2.7.2 Segmentation or cluster delineation step . . . 18
2.8 Drawbacks of *mean shift* . . . 19
2.9 Conclusion . . . 19

II METHODOLOGICAL CONTRIBUTION on MEAN SHIFT FILTERING 21

3 Introduction of Methodological Contribution 25

4 Blurring and noise effect on Mean Shift Filtering 27
4.1 Introduction . . . 27
4.2 Data and materials . . . 28
4.3 Effect of noise and blurring in feature space . . . 28
4.3.1 Only noise effect in feature space . . . 29
4.3.2 Only blurring effect in feature space . . . 29
4.3.3 Mixed Noise and blurring effect in feature space . . . 30
4.4 Image Quality Assessment . . . 32
4.4.1 PSNR . . . 32
4.4.2 SSIM . . . 32
4.5 Exhaustive search for MS . . . 33
4.6 Results and discussion . . . 33
4.6.1 Only noise effect on MSF . . . 33
4.6.2 Only blurring effect on MSF . . . 34
4.6.3 Mixed blurring and noise on MSF . . . 35
4.7 Conclusion . . . 36

5 Bandwidth optimization on Mean Shift Filtering 37
5.1 Introduction . . . 37
5.2 Error criteria . . . 38
5.3 Data . . . 41
5.3.1 Synthesized Tito image . . . 41
5.3.2 Synthesized MRI image . . . 41
5.3.3 Natural images . . . 42
5.4 Description of and experiment . . . 43
5.4.1 PI bandwidth selectors . . . 43
5.4.2 Exhaustive search . . . 44
5.5 Results and discussion . . . 44
5.5.1 Illustration of bandwidth influence on MSF . . . 44
5.5.2 PI results . . . 45
5.6 Conclusion . . . 49

6 From Grid-sample method to Probability-Map method 51
6.1 Introduction . . . 51
6.2 Grid sample-method for segmentation framework . . . 51
6.2.1 Pre-processing . . . 52
6.2.2 Mean shift filtering . . . 52
6.2.3 Region growing segmentation . . . 53
6.2.4 Bandwidth optimization of MS and RG . . . 54
6.2.5 Post-processing . . . 56
6.2.6 Result of Cartesian-Grid based framework . . . 56
6.2.7 Properties of Cartesian-Grid based framework . . . 56
6.3 Probability map method . . . 57
6.3.1 Framework of *PM* method . . . 57
6.3.2 Principle of probability map method . . . 58
6.3.3 Random Number Generators . . . 59

6.3.4 Experiments and results . . . 61
6.4 Conclusion . . . 64

7 Conclusion of Methodological Contribution 67

III APPLICATION to MEDICAL ISCHEMIC DATA 69

8 Introduction of medical application part 73

9 Medical Context and Objectives 75
9.1 Introduction . . . 75
9.2 What is Stroke? . . . 75
9.2.1 Definition and causes of stroke . . . 75
9.2.2 Diagnosis methods . . . 76
9.2.3 Therapy protocols . . . 76
9.2.4 Summary of definitions . . . 77
9.3 Basics of MRI . . . 78
9.4 Diffusion-Weighted Imaging . . . 78
9.5 Perfusion-Weighted Imaging . . . 79
9.5.1 Bolus-contrast tracking . . . 79
9.5.2 First pass technique . . . 79
9.5.3 Converting time-concentration curves into Perfusion parameter maps . . . 80
9.5.4 Perfusion Parameters . . . 82
9.6 Objective and strategy . . . 83
9.6.1 Automatic estimation of final infarct . . . 83
9.6.2 Optimal predictor of multiple MRI parameters . . . 83
9.7 Conclusion . . . 84

10 Global Framework 85
10.1 Introduction . . . 85
10.2 State of art on ischemic segmentation . . . 85
10.3 Proposed global framework . . . 86
10.3.1 Input data in feature space . . . 87
10.3.2 Pre-processing . . . 87
10.3.3 CGNG for *mean shift* and *region growing* . . . 88
10.3.4 QRNG with *PM* . . . 88
10.3.5 Seeds selection in *region growing* segmentation . . . 89
10.3.6 Post-processing . . . 89
10.4 Segmentation validation criteria . . . 89
10.4.1 Sensitivity and specificity . . . 90
10.4.2 ROC curve . . . 90
10.5 Conclusion . . . 90

11 Data and Materials 91
11.1 Introduction . . . 91
11.2 Rats' data . . . 91
11.2.1 Description of rats' data . . . 91
11.2.2 Information about MRI acquisition [Chauveau 11] . . . 92
11.2.3 Derivation of multi-parametric maps on rats . . . 93

11.2.4 Properties of rats' data 94
11.3 Humans' data 95
11.3.1 I-KNOW database 95
11.3.2 Derivation of multi-parametric maps on human 95
11.3.3 Properties of human's data 96
11.4 Conclusion 97

12 Results **99**
12.1 Introduction 99
12.2 Results of rats data 99
12.2.1 Final infarct segmentation by using CGNG 100
12.2.2 *PM* by using QRNG 102
12.3 Results of patients' data 105
12.3.1 Final segmentation 105
12.3.2 Analysis of probability map 107
12.4 Conclusion 108

13 Conclusion and perspectives **111**
13.1 Conclusion 111
13.2 Perspectives 112

IV CONCLUSION and PERSPECTIVES **115**

14 General Conclusion and Perspectives **117**
14.1 Plan of Contribution 118
14.2 Perspectives 118

Annexes **123**

A Effect of PCA on *mean shift* **123**

V Bibliography **125**

Bibliographie **127**

List of Figures

1.1 Multi-modality maps, (a) is the noncontrast-enhanced CT, (b) shows T2-weighted FLAIR image and (c) is PET/CT data. . . . 3
1.2 Multi-modality maps with the ischemic lesion at hour 0 (IKNOW38), the ischemic lesions are delineated by red color. . . . 4
1.3 Synthesized RGB color data in feature space. . . . 5

2.1 Synthesized RGB color data and corrupted data. . . . 12
2.2 Intuitive description of Mean Shift. . . . 15

4.1 Synthesized RGB data and its properties. . . . 28
4.2 Noise effect on synthesized RGB data in feature space, the noisy images are observed with the same color map because the values after noise are over 255. . . . 29
4.3 Blurring effect on synthesized data in feature space. . . . 30
4.4 Influence of noise on synthesized data with fixed blurring $\mathbf{B}[15, 5]$ in feature space, the corrupted images are observed with the same color map because the values after noise are over 255. . . . 31
4.5 Influence of blurring on synthesized data with fixed noise $\sigma_N = 30$ in feature space, the corrupted images are observed with the same color map because the values after noise are over 255. . . . 31
4.6 PSNR and SSIM evolution according to various noise on MSF. . . . 34
4.7 PSNR and SSIM evolution according to various blurring on MSF. . . . 34
4.8 PSNR and SSIM evolution according to various noise with $\mathbf{B}[15, 3]$ on MSF. . . . 35
4.9 PSNR and SSIM evolution according to various blurring with fixed noise ($\sigma_N = 30$) on MSF. . . . 36

5.1 Synthesized Tito data and its properties. . . . 41
5.2 Synthesized MRI data and its properties. . . . 42
5.3 Feature space representation of synthesized MRI data. . . . 42
5.4 Natural RGB images. . . . 43

5.5 Mean Shift filtering results for corrupted MRI according to different bandwidth parameters. (a) is the original MRI data (e) is corrupted data with $\mathbf{B}[63, 1]$; The reference PSNR is computed by corrupted image and original image; (b),(c) and (d) are filtered results obtained from the fixed h_s=2 but different h_r along the range $[1, 255]$; the PSNR is computed by filtered image and original image; (c) is the optimal *mean shift* filtered result with optimal PSNR equal to 26.19dB; (f),(g) and (h) are filtered results obtained from the fixed h_r=80 but different h_r along the range [1,5]. 45
5.6 PSNR assessment according to h_s and h_r. 46
5.7 Detailed PSNR assessment according to h_s=1 to 10 and h_r=5 to 100. 46
5.8 PSNR evolution against h_s and h_r 47
5.9 PSNR and SSIM calculation by PI methods on Lena. 47
5.10 PSNR and SSIM calculation by PI methods on Mandrill. 47
5.11 PSNR and SSIM calculation by PI methods on Peppers. 48
5.12 PSNR and SSIM calculation by PI methods on Lake. 48
5.13 PSNR and SSIM calculation by PI methods on Tito. 48
5.14 PSNR and SSIM calculation by PI methods on MRI ($\sigma = 10$). 49

6.1 Reference white matter segmentation of original labeled MRI image. 52
6.2 Framework of MSRG-based segmentation. 52
6.3 Procedures of RG segmentation. 53
6.4 White matter segmentation of original labeled MRI image by using only RG. . . 55
6.5 Bandwidth optimization of MS and RG with DICE. 55
6.6 White matter segmentation of corrupted MRI image by using MS and RG. . . . 56
6.7 Framework of probability map 57
6.8 Illustration of the three studied random number generators. 59
6.9 Probability map of white matter segmentation for original labeled MRI image by using only RG. 61
6.10 Probability map of white matter segmentation of corrupted MRI image by using MS and RG. 62
6.11 Probability map of different random generators. 63
6.12 Optimal DICE obtained with various random sample numbers 65

9.1 Stroke ischemia. 76
9.2 Dynamic evolution of brain ischemia. 77
9.3 DWI(a) and ADC parameters(b) showing core of infarct in acute stroke (Hour 0). 79
9.4 Time course of a typical enhanced dynamic susceptibility contrast (DSC) imaging experiment. 80
9.5 Time concentration tracer curve turned into a measure of perfusion. 81

10.1 Global work flow for predicting the infarct. 87
10.2 Statistical Error Description. 89

11.1 Ischemia on rat's brain. 92
11.2 Multiparametric MRI acquisition of rats study. 93
11.3 Rat data description along time. 94
11.4 ADC at day 0 with reference infarct (seven slices of rat pMCAO2). 94
11.5 peak and TTP at day 0 with reference infarct(seven slices of rat pMCAO2). . . 94
11.6 T2 anatomical image at day 0, day 4 and day 12 with reference infarct (seven slices of rat pMCAO2). 94

11.7 Human data description along time. 96
11.8 Human ischemic multi-modal MRI parameters illustration (11th slice of patient171). 96

12.1 ADC, peak and TTP (with manually selected seeds) after using brain mask (seven slices of rat pMCAO2). 100
12.2 Optimal final infarct segmentation of 'pMCAO2' with ADC and peak. 101
12.3 Optimal predictor of different combination of multi-modal MRI parameters based on ROC curve before polynomial regression (pMCAO4). 102
12.4 Optimal predictor of different combination of multi-modal MRI parameters based on ROC curve (pMCAO4). 103
12.5 *PM* for predicting infarct of pMCAO2 with three combinations. 103
12.6 Convergence of bias and variance of *PM* by using bootstrap method (rat pMCAO2). 104
12.7 Infarct segmentation of combination of 5 parameters (Patients171). 106
12.8 DICE for each slices of figure 12.7, the yellow region is the true segmented points, the red region is over-segmented points and the white region is under-segmented points (Patients171). 106
12.9 *PM* of multi-parameters: TTP and MTT for 20 slices with reference segmented results at days 30 (Patients171). 107
12.10 *PM* of multi-parameters: ADC and DWI for 20 slices with reference segmented results at days 30 (Patients171). 107
12.11 *PM* of multi-parameters: TTP, MTT and CBF for 20 slices with reference segmented results at days 30 (Patients171). 107
12.12 *PM* of multi-parameters: TTP, MTT and DWI for 20 slices with reference segmented results at days 30 (Patients171). 108
12.13 *PM* of multi-parameters: TTP, MTT, CBF, ADC and DWI with reference segmented results at days 30 (Patients171). 108
12.14 Threshold of *PM* for various combination of multi-parameters (Patient171). . . . 109

13.1 ROC curves of 'pMCAO4' reflecting performance of algorithm with DICE. . . . 112

List of Tables

5.1 Comparison of optimal PI results and optimal Exhaustive Search results on PSNR. 49

6.1 Scale parameter ranges for MS and RG for CGNG. 55
6.2 Scale parameter ranges for MS and RG. 63
6.3 Time-consuming for different type of random generators. 64

10.1 Scale parameter ranges of CGNG for medical data. 88
10.2 Scale parameter ranges of QRNG for medical data. 88

11.1 Information of the rats. 91

12.1 Proposed framework compared with 'onlyRG' framework according to DICE* coefficient. 101
12.2 Comparison of different combination of multi-model MRI parameters on rats according to optimal DICE coefficient by using proposed framework. 101
12.3 Comparison of different combination of multi-model MRI parameters on human according to optimal DICE coefficient by using proposed framework. 106

List of symbols and abbreviations

Methodological part

MS	Mean Shift
RG	Region Growing
PDF	Probability density function
KDE	Kernel density estimation
iid	independent and identically-distributed
MSE	Mean Square Error
PSNR	Peak Signal Noise Ratio
SSIM	Structural Similarity Image Measurement
MS	Mean Shift
RG	Region Growing
PM	Probability Map
MISE	Mean Integrated Square Error
AMISE	Asymptotic Mean Integrated Squared Error
CGNG	Cartesian-Grid Number Generator
PRNG	Pseudo-Random Number Generator
QRNG	Quasi-Random Number Generator
PCA	Principle Component Analysis
$\hat{f(\mathbf{x})}$	density estimator
R^d	d-dimensional feature space
$\mathbf{H}$	bandwidth matrix
K	kernel function
$K_{\mathbf{H}}$	kernel function based on bandwidth matrix $\mathbf{H}$
$\Gamma(.)$	gamma function
$\nabla \hat{f}(\mathbf{x})$	gradient of the density estimator
σ_N	standard deviation of noise
$\mu_{\mathbf{x}}$	mean of the $\mathbf{x}$
$\sigma_{\mathbf{xy}}$	cross correlation
$\overline{it}$	mean number of iterations
$\mathbf{H}_{MS}$	bandwidth matrix of MS
$\mathbf{H}_{RG}$	bandwidth matrix of RG
hs_{MS}	spatial bandwidth value of MS
hr_{MS}	range bandwidth value of MS
hs_{RG}	spatial bandwidth value of RG
hr_{RG}	range bandwidth value of RG

Medical application part

CT	Computerize Tomography
MRI	Magnetic Resonance Imaging
DWI	Diffusion Weighted Imaging
PET	Positron Emission Tomography
ADC	Apparent Diffusion Coefficient
PWI	Perfusion Weighted Imaging
DSC	Dynamic Susceptibility Contrast
AIF	Arterial Input Function
tPA	tissue Plasminogen Activator
RF	Radiomagnetic field
CSF	Cerebrospinal fluid
FLAIR	Fluid-attenuated inversion-recovery
TR	Repetition time
TE	Echo times
SE	Spin Echo
GE	Gradient Echo
ADC	Apparent Diffusion Coefficient
EPI	Echo Planar Imaging
TTP	Time To Peak
CBF	cerebral blood flow
rCBV	relative cerebral blood volume
MTT	Mean Transit Time
Tmax	Time of arrival
MCA	Middle Cerebral Artery
ECA	External Carotid Artery
ROI	Region of Interest

I GENERAL INTRODUCTION

Chapter 1

PhD context and objectives

1.1 Introduction

Medical image processing plays an important role in clinical diagnosis and scientific research. Medical studies are increasingly using multi-modality imaging, *e.g.* a combination of different imaging modalities like computerized tomography (CT), magnetic resonance imaging (MRI) etc, which produces multidimensional data that bring additional information but are also challenging to process and interpret.

Figure 1.1 is an example of multi-modality maps from "Wayne Forrest, AuntMinnieEurope.com". It is a 56-year-old patient with glioblastoma multiforme on the right side in the frontal area close to interhemispheric fissure.

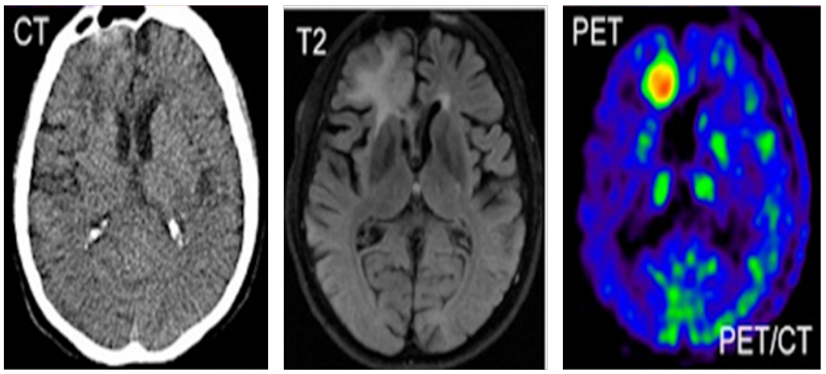

(a) CT (b) T2 (c) PET/CT

Figure 1.1: Multi-modality maps, (a) is the noncontrast-enhanced CT, (b) shows T2-weighted FLAIR image and (c) is PET/CT data.

Figure 1.2 shows another example of multi-modality maps from the 'I-KNOW database' consisting of real images of people who have suffered stroke (http://www.i-know-stroke.eu/).

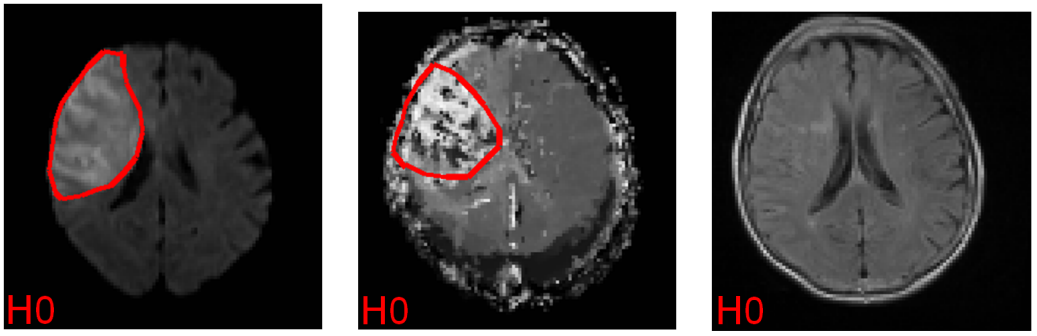

(a) DWI (b) PWI (c) T2

Figure 1.2: Multi-modality maps with the ischemic lesion at hour 0 *(IKNOW38), the ischemic lesions are delineated by red color.*

Processing such multi-dimensional data requires the use of advanced image processing algorithms such as multidimensional filtering, segmentation and clustering to extract relevant information and to discover new knowledge.

In certain situations where doctors need to "look inside the human body" before decisions regarding any form of treatment can be made, medical imaging is indispensable. One such example is the case of a stroke. Stroke is the third leading cause of death in industrialized countries and the first cause of long-term adult disability, and is therefore a crucial health care issue. Ischemic stroke (85% of total stroke) is caused by the occlusion of a cerebral artery. The success of thrombolysis therapy is highly time dependent; consequently, accurate diagnosis of the ischemic condition must be done within a limited time window (4.5 hours) if irreversible damage are to be limited.

Medical Imaging plays a central role in estimation and diagnosis of patients with a stroke or cerebral ischemia [Fisher 03, Hjort 05] and can be useful before and after the occurrence of a stroke. Multi-modality MRI maps provide doctors with information they need to select the appropriate therapy for treatment after the occurrence of a stroke. However, the traditional, time-tested method of manually processing and analyzing imaging data by medical professionals can be time intensive, impractical when several volumes are to be analyzed and subject to variabilities related to the subjectivity of the professional performing the analysis. In addition, the professional will not be able to make effective use of latent information which may be contained or deduced from the raw images. Thus, automatic segmentation of the ischemic region based on multi-modality MRI maps has increasingly become an area of intensive research for many researchers in recent years. In addition, for the available MRI modalities, researchers are faced with the difficult problem of identifying the characteristic parameters of the process, choosing the optimal parameters and finding their optimal values.

An important approach for the processing of multi-modality MRI images is feature space analysis.

A feature space is defined as an abstract space where each pattern sample is represented as a

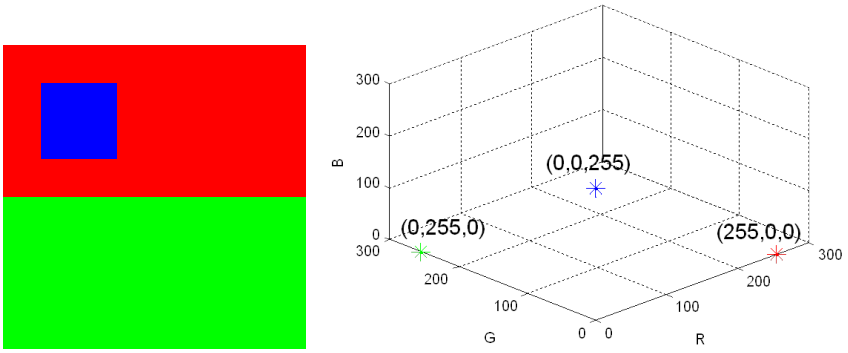

(a) Original data. (b) FS of original data.

Figure 1.3: Synthesized RGB color data in feature space.

point in an d-dimensional space (*e.g.* in figure 1.3 the Red (R), Green (G) and Blue (B) colors could be presented as the three features of the color image in three dimensional feature space). The dimension of the feature space is determined by the number of features used to describe the patterns.

Once transformed into the feature space representation, we can conveniently apply various image processing techniques to perform processes such as classification, filtering, segmentation etc. It is often advantageous that the segmentation or clustering algorithm includes spatial information into the construction of the feature space. When spatial information is taken into consideration, similar features can be grouped together, which allows the use of density estimation for finding patterns to realize segmentation and clustering.

An important feature space analysis technique which is based on non-parametric kernel estimation is *mean shift*. *Mean shift* is an increasingly popular image processing technique which can be used to implement filtering [Comaniciu 02], clustering and segmentation [Comaniciu 03] in the feature space. *Mean shift* was successfully applied to medical image segmentation and filtering in [Tek 01, Grenier 05a, Grenier 06]. In this these, based on *mean shift* algorithm, a global framework is employed for quantifying the ischemic region and estimating relevant optimal combinations of multi-modality MRI maps.

Mean shift has some desirable properties compared to other feature space analysis techniques such as density based clustering and K-means clustering such as not requiring prior knowledge of the number of clusters. It also has good de-noising properties [Comaniciu 02]. Comaniciu et al proved that, under certain conditions, *mean shift* algorithm will converge to the nearest mode of the steady-state probability density function (PDF), so the *mean shift* algorithm can be used to detect the existence of the pdf modes and can be employed for filtering or clustering.

Since it is based on *mean shift*, it was necessary to more fully explore its limitations and find ways to compensate for them. For example, filtering and de-noising steps in image processing often involve some amount of blurring and mean shift can be designed to reduce the blurring effect. However, it is important to know the limit of the de-noising performance and the extent to which *mean shift* can reduce the blurring effect.

The large success of *mean shift* is largely due to the intuitive tuning of bandwidth parameters which determine the scale at which features are analyzed. However, without prior knowledge, no rule is known to determine the optimal bandwidth matrix for *mean shift*. In [Wand 95], the statistical framework provided optimizations of the bandwidth matrix for kernel density estimation according to the underlying data. The *plug-in* (PI) method is one of the most efficient rules having good theoretical and practical properties for one dimension spaces. Thus, the *plug-in* rule has been widely used as a one-dimensional bandwidth selector for *mean shift* application on gray level images[Comaniciu 01, Grenier 06]. Nevertheless, no one has extended and used multi-dimensional *plug-in* for bandwidth matrix estimation on *mean shift* filtering of multi-dimensional images (*e.g.* color images).

Many *mean shift* applications used a two-valued bandwidth matrix: one value for the spatial feature and the other for the range feature. Such bandwidth matrices are isotropic for each feature. Here, we also deal with anisotropic range matrix, i.e. one scale value for each feature.

In order to tackle the limiting factors described above, in this thesis, improvements to the mean shift process and its application on medical images are proposed by implementing the following steps:

1. firstly, we focus on the noise and the blurring effect in the feature space to well understand the advantages and limitations of *mean shift* algorithm.
2. secondly, we study the influence of bandwidth parameters on *mean shift* by researching all possible bandwidth parameters in order to have a global view of its evolution. Then, we try to propose a bandwidth estimation method in multi-dimensional case on *mean shift* to automatically obtain the optimal global bandwidth parameters.
3. thirdly, by using the *mean shift* filtering, we propose a new automatic segmentation framework considering optimization of bandwidth parameters. The feasibility and robustness of this new framework should be verified based on synthesized data.
4. finally, we employ the proposed segmentation framework on medical application to solve the specific problems.

Additionally, we verified that applying Principle Component Analysis (PCA) transformation is useless for *mean shift* if no dimension reduction is done [Li 11]. The verification and explanation are in Appendix A.

1.2 Structure of the thesis

This thesis consists of 13 chapters divided into five parts:

1. Introduction: we introduce the context and objectives in chapter 1 as well as the *mean shift* method used for the thesis in chapter 2.
2. Theoretical contribution on *mean shift*: in chapter 4, we discuss the effects of noise and blurring on the *mean shift* process; in chapter 5, we propose multi-dimensional *plug-in* method to estimate the optimal global bandwidth parameters on *mean shift* filtering; in chapter 6,

we propose a new probability map method for region clustering and segmentation without using a reference image.

3. Application to medical data: in chapter 8, we summarized the application to medical data; the medical context and objectives are introduced in chapter 8; based on the medical context, we proposed our framework in chapter 10; chapter 11 presents the data and materials we used; the results and conclusions are discussed in chapter 12 and chapter 13.
4. Conclusion: we generalize the conclusion and perspectives in chapter 14.

Chapter 2

Mean Shift and Mean Shift Filtering

2.1 Introduction

Mean shift is a well known method based on feature space analysis. This method is based on a non-parametric kernel-based estimator of the data density gradient. *Mean shift filtering* is not a direct clustering method, but acts as a forerunner of clustering (a merging step should be added). However, *mean shift* is usually associated to a clustering approach. We will use *mean shift* filtering terms when no merging step is implemented.

In section 2.2, we retrospectively examine the history of *mean shift* and its development during recent years.

Section 2.3 introduces the Feature Space, *i.e.* the multidimensional space used by *mean shift*.

In section 2.4, we present the Kernel Density Estimation and the gradient density estimation based on the Parzen window. We also remind some properties of kernels used.

In section 2.5, we describe the basic idea and theoretical principle behind *mean shift* algorithms. This algorithm aims at associating each sample to its local maximum by an iterative search until convergence process. We introduce procedures of *mean shift filtering* in section 2.6. *Mean shift* clustering is explained in section 2.7.

Mean shift is commonly the algorithm of choice in the field of data clustering as it is well adapted to a rather small number of dimensions (< 6), and it does not require any information about the number of clusters we need to obtain. The choice of bandwidth is crucially important in determining the performance of *mean shift*. Especially for multivariate data, the correlation among dimensions needs to be carefully taken into account. The drawbacks of *mean shift* will be discussed in the last section 2.8.

2.2 *Mean shift* State of the Art

2.2.1 History and applications

Mean shift was first proposed in [Fukunaga 75]. It initially failed to catch the attention of the scientific community despite its high efficiency in locating the modes until 1995 when Cheng published an important literature in [Cheng 95]. In this paper, Cheng defined a family of Yizong Cheng kernels. He also set a weight coefficient function, giving the various importance of different samples, which greatly extends the application of *mean shift*. Comaniciu then successfully applied *mean shift* in analysis of feature space, especially on image smoothing and segmentation problems [Comaniciu 99]. Moreover, Comaniciu and others proofed in [Comaniciu 02] that *mean shift* algorithm under certain conditions, will converge to the nearest point of the steady-state probability density function. Hence, it can be used to detect the existence of the modes of the probability density function.

Furthermore, Carreira-Perpinan [Carreira-Perpinan 07] proved that *mean shift* with a Gaussian kernel corresponds to the Expectation Maximization (EM) algorithm and can speed up the convergence rate of *mean shift*.

Recently, Fashing and Tomasi [Fashing 05] developed the understanding that *mean shift* is a bound optimization which is equivalent to Newton's method in the case of piecewise constant kernels. Also, they have also proved that for all kernels the mean shift procedure is a quadratic bound maximization.

From an information theory perspective, [Rao 09] develops a new understanding of *mean shift* algorithms by stating that Gaussian blurring *mean shift* (GBMS) directly minimizes the Renyi's quadratic entropy and thereby is unstable by definition. Moreover, Gaussian *mean shift* (GMS) minimizes the Renyi's cross entropy where the local stationary solutions are modes of the data set.

In recent times, considerable interest has been shown in applying *mean shift* to problems in computer vision, based mainly on the work of Comaniciu and Meer in areas like discontinuity-preserving smoothing, segmentation [Comaniciu 03], and tracking [Gorry 07]. The idea of *mean shift* based tracking has also been extended by accounting for a variable-bandwidth mean shift in [Comaniciu 01]. Related to this, Collins [Collins 03] has looked into the problem of tracking blobs across scale space which accounts for variation in the scale of the kernel.

Mean shift was also successfully applied to medical image segmentation and filtering [Tek 01, Grenier 05a, Grenier 06, Arnaldo 09].

2.2.2 Other Feature Space Filtering Approaches

Many papers have illustrated the robustness of *mean shift* [Cheng 95, Fashing 05] and its superiority over classical filtering methods such as anisotropic diffusion and bilateral filtering [Barash 04].

Buades [Buades 05] introduces the non-local means (*NL-means*) approach that is one of the best de-noising approach (without assumption on image and noise). This approach is based on image blocks: similar image blocks are searched in the image and the central pixel of a block is

filtered according to the value of all central pixels of similar blocks.

Based on a close idea, Dabov [Dabov 07] proposes the BM3D: an image de-noising strategy based on an enhanced sparse representation in transform domain. The enhancement of the sparsity is achieved by grouping similar 2D image blocks in 3-D arrays called "groups". Then a special procedure (collaborative filtering) applied to deal with these groups and filtered it. As the blocks are overlapping, for each pixel, they obtain many different estimates which need to be combined.

A recent study of Chatterjee [Chatterjee 10] details various de-noising techniques and compares them to a theoretical limit derived from the Mean Square Error (MSE).

Mean shift is not the best de-noising approach. Therefore, compared to NL-means and BM3D, *mean shift* is a straightforward approach that allows not only image de-noising but also filtering and clustering (in this case, a merging step is needed), its computational complexity is tractable and the influence of the tuning parameters are simple to understand.

2.3 Feature Space Representation

Multidimensional data has become increasingly important in fields such as medical imaging.

An efficient way to represent multidimensional data is the use of feature space techniques [Scholkopf 99]. It provides a reliable enough representation of the input data and allows processes to be controlled by a few number of tuning parameters corresponding to understandable measures in the input domain. An example of a tuning parameter is the scale parameter also called bandwidth parameter and commonly summarized in a matrix.

Mean shift is a non-parametric feature-space analysis technique. The main idea behind *mean shift* is to process the pixels in the d-dimensional feature space as an empirical PDF where dense regions in the feature space correspond to local maximum or modes of the underlying distribution. In the following figure, we illustrate the representative description of feature space by using the diffusion process for modeling the noise and blurring process.

The synthesized data used comprises a set of 3 color clusters (see Figure 2.1(a)) that gives clean data i.e. noise free data. A corrupted data is obtained by blurring using a Gaussian shaped kernel $[63, 63]$ with $\sigma = 1$, and then adding Gaussian noise with $\sigma = 10$. The corrupted data is then restored using *mean shift* filtering and the resultant data is shown in Figure 2.1(c). Figure 2.1(d) and (e) are the feature space representations of the original synthesized data and the corrupted data while 2.1(f) is the restored data after *mean shift* processing. The feature space representation shows which image point is to be classified as belonging to a specific red, green, or blue cluster. After blurring and noise addition, the cluster become more disperse and more difficult to separate. By using *mean shift* filtering, the three clusters are classified to the specific cluster.

This illustration allows us to visualize a feature space and understand blurring and noise effects in such a feature space. Also, it allows one to assess the ability of *mean shift* filtering to remove the noise and retrieve the original classes (or clusters) in the feature space.

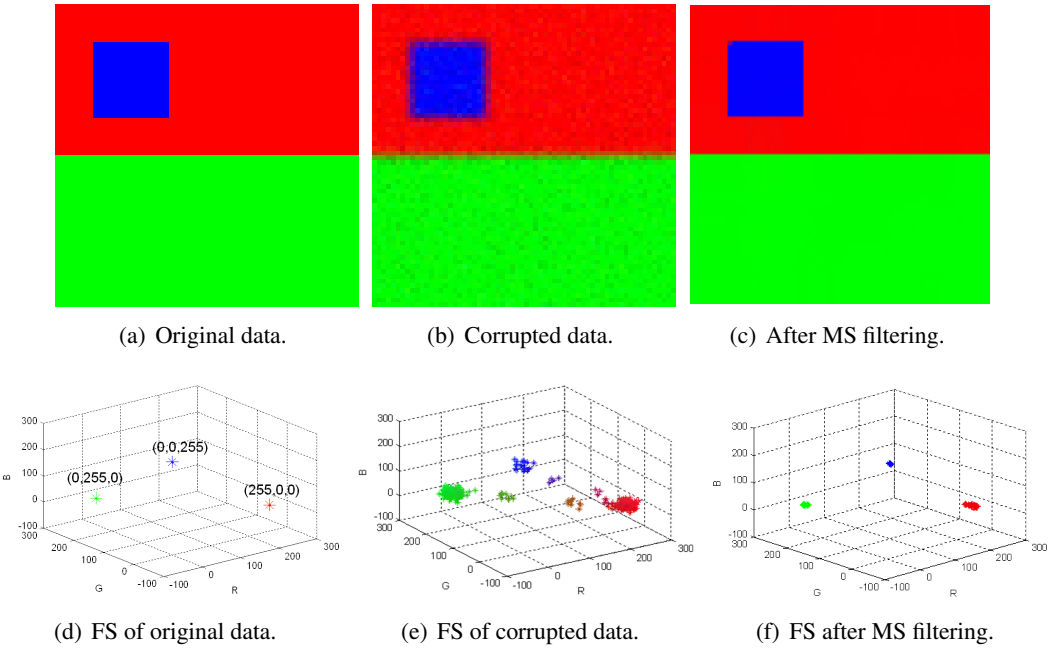

(a) Original data. (b) Corrupted data. (c) After MS filtering.

(d) FS of original data. (e) FS of corrupted data. (f) FS after MS filtering.

Figure 2.1: Synthesized RGB color data and corrupted data.

2.4 From Kernel Density to Gradient Density Estimation

2.4.1 Probability density function

Application of mathematical principles and statistical analysis to digital image processing can reveal important information. The Probability Density Function (PDF) is a fundamental concept in statistical analysis which plays an important role in image processing. Given the probability density function $f(x)$ of a random variable x, the probability that the value of x will fall within a given interval $[a, b]$ is expressed as:

$$P(a < x < b) = \int_a^b f(x)dx \tag{2.1}$$

In an image, the pixels intensities can be seen as a series of observations assumed to be a sample from an unknown PDF. Density estimation is the problem of modeling a density given a finite number of observations drawn from that PDF. It can be categorized into two basic approaches: parametric density estimation and non-parametric density estimation.

Parametric density estimation normally refers to parameter estimation for a given form of PDF. As an example, we optimize mean and variance of a Gaussian distribution in the Maximum Likelihood sense by fitting the model of the data set. Compared to the parametric density estimation, non-parametric density estimation does not rely on data belonging to any particular distribution and has no fixed structure function. Most of our attention, in this thesis, will be on non-parametric density estimation.

Histogram [Wand 95, Parzen 62] is the simplest and most popular form of non-parametric density estimation. It only requires two parameters to be defined: bin width and starting position

of the first bin. However, they are exactly the source of its drawbacks. The final shape of the density estimation depends on the starting points of the bins. The choice of bin locations will create discontinuities of the estimate. It will make the use of density estimation very difficult to acquire the structure of the data. In multi-dimensional space, more serious discontinuities appear as the number of bins grows exponentially with the number of dimensions.

Kernel density estimation (KDE), which is also called Parzen Window method, is another approach used to estimate the unknown density function in probability theory. It is one of the methods of non-parametric tests proposed by Rosenblatt [Rosenblatt 56] and Emanuel Parzen [Parzen 62].

2.4.2 Kernel Density Estimation

Let x_i, $i = 1, 2...n$ be a data set of n independent and identically-distributed (iid) samples of a random variable in $\mathbb{R}$. The monovariate kernel density estimator $\hat{f}$ computed at the point $x \in \mathbb{R}$ is given by [Parzen 62]:

$$\hat{f}(x) = \frac{1}{nh} \sum_{i=1}^{n} \frac{1}{h} K(\frac{x - x_i}{h}) \tag{2.2}$$

where K is a monovariate kernel which is assumed to be a PDF and h is the bandwidth value.

We extend the kernel density estimator to a multivariate situation. Let $\mathbf{x}_i$, $i = 1, 2...n$ be a data set of n independent and identically-distributed (iid) samples of a random variable in the d-dimensional feature space $\mathbb{R}^d$, $\hat{f}$ computed at the point $\mathbf{x} \in \mathbb{R}^d$ is given by:

$$\hat{f}(\mathbf{x}; \mathbf{H}) = \frac{1}{n} \sum_{i=1}^{n} K_{\mathbf{H}}(\mathbf{x} - \mathbf{x}_i) \tag{2.3}$$

where $\mathbf{H}$ is a $d \times d$ symmetric positive definite matrix called the bandwidth matrix. The choice of $\mathbf{H}$ is crucially important in determining the performance of $\hat{f}$. Also, $K_{\mathbf{H}}$ is a d-variate kernel function which is detailed in the following section.

$$K_{\mathbf{H}}(\mathbf{x}) = |\mathbf{H}|^{-1/2} K\left(\mathbf{H}^{-1/2}\mathbf{x}\right) \tag{2.4}$$

2.4.3 Choice of kernel

Normally K is a d-variate radially symmetric kernel function satisfying the following properties:

$$\int K(\mathbf{x})\, d\mathbf{x} = \mathbf{1}; \int \mathbf{x} K(\mathbf{x}) d\mathbf{x} = 0; \lim_{\|\mathbf{x}\| \to \infty} \|\mathbf{x}\|^d K(\mathbf{x}) = 0; \int \mathbf{x}\mathbf{x}^T K(\mathbf{x}) d\mathbf{x} = c\mathbf{I} \tag{2.5}$$

where c is a constant that makes K integrate to one. In other words, any probability density that is square integrable can be selected as the kernel K. Conditions on the multivariate kernel K and bandwidth matrix $\mathbf{H}$ to guarantee the asymptotic unbiasedness, the mean-square consistency and the uniform consistency can be found in [Fukunaga 75].

In the following discussion, we only use the spherical Epanechnikov kernel K_E^S which satisfies the previous conditions and which yields to the optimal spherically symmetric multivariate kernel

according to the asymptotic mean integrated square error.

$$K_E^S(\mathbf{x}) = \begin{cases} 1/2.v_d^{-1}(d+2)(1-\mathbf{x}^T\mathbf{x}) & \text{if } \|\mathbf{x}\| < 1 \\ 0 & \text{otherwise} \end{cases} \tag{2.6}$$

where $v_d = 2\pi^{d/2}/\{d\Gamma(d/2)\}$ is the volume of the unit d-dimensional sphere with $\Gamma(.)$ the gamma function.

2.4.4 Expression of Gradient Density Estimation

As we do not know the true PDF, we have to rely on nonparametric techniques to obtain density gradient estimates. We assume that the straightforward density estimation procedure is a differentiable function of PDF taking the gradient of the density estimator, see the equation 2.7:

$$\nabla\hat{f}(\mathbf{x}) = \frac{1}{n}\sum_{i=1}^{n}\nabla K_{\mathbf{H}}(\mathbf{x}-\mathbf{x}_i) \tag{2.7}$$

The expression of gradient estimation depends on the gradient of kernel, with the formation of $K_{\mathbf{H}}$ given by equation 2.4, the gradient of kernel is presented as (see the equation 2.8):

$$\nabla K_{\mathbf{H}}(\mathbf{x}) = |\mathbf{H}|^{-1/2}.\nabla K(\mathbf{H}^{-1/2}\mathbf{x}) \tag{2.8}$$

We can notice that multivariate kernels are often radially symmetric functions. Therefore, they can be expressed with a special class of radially symmetric univariate kernels $k(x)$, for $x \geq 0$, called profile, as in the following equation:

$$K(\mathbf{x}) = C_{k,d}.k(\mathbf{x}^T\mathbf{x}) \tag{2.9}$$

Thus the equation 2.8 is presented as equation 2.10 (with $k^{'}$ the derivation of function k):

$$\nabla K_{\mathbf{H}}(\mathbf{x}) = 2C_{k,d}.|\mathbf{H}|^{-1/2}.\mathbf{H}^{-1}.\mathbf{x}.k^{'}(\mathbf{x}^T\mathbf{H}^{-1}\mathbf{x}) \tag{2.10}$$

This allows us to rewrite the equation of the gradient estimation in equation 2.11:

$$\hat{\nabla}f(\mathbf{x}) = \frac{2.C_{k,d}.\mathbf{H}^{-1}}{n.|\mathbf{H}|^{1/2}}\sum_{i=1}^{n}(\mathbf{x}-\mathbf{x}_i).k^{'}((\mathbf{x}-\mathbf{x}_i)^T\mathbf{H}^{-1}(\mathbf{x}-\mathbf{x}_i)) \tag{2.11}$$

By taking $g(x) = -k^{'}(x)$ with Epanechnikov kernel K_E^S and some further algebraic manipulations, we obtained the following expression:

$$\hat{\nabla}f(\mathbf{x}) = \frac{2.C_{k,d}.\mathbf{H}^{-1}}{n.|\mathbf{H}|^{1/2}}\sum_{i=1}^{n}g(d^2(\mathbf{x},\mathbf{x}_i,\mathbf{H})).\left[\frac{\sum_{i=1}^{n}g(d^2(\mathbf{x},\mathbf{x}_i,\mathbf{H})).\mathbf{x}_i}{\sum_{i=1}^{n}g(d^2(\mathbf{x},\mathbf{x}_i,\mathbf{H}))} - \mathbf{x}\right] \tag{2.12}$$

where $d(\mathbf{x},\mathbf{x}_i,\mathbf{H}) = ((\mathbf{x}-\mathbf{x}_i)^T\mathbf{H}^{-1}(\mathbf{x}-\mathbf{x}_i))^{-1/2}$ is the Mahalanobis distance. The first term is

proportional to the density estimate at $\mathbf{x}$. The second term is called the *mean shift* vector which shifts towards the direction of maximum increase in density and converges to the local maximum or modes (weighted average). That is how *mean shift* got its name [Fukunaga 75, Cheng 95, Fashing 05, Grenier 06].

2.5 *Mean shift* Algorithm

2.5.1 Intuitive description of mean shift

Mean shift regards feature space as a empirical PDF. Each pixel of the image is considered as a vector $\mathbf{x}$ in the feature space. According to the application, this vector can be built from different features like the spatial position, the color components, normal vectors, ... *Mean shift* considers this set of vectors as sampled from the underlying PDF. If dense regions (also called clusters) exist, they should correspond to local maximum (also called mode) of the PDF. We can identify these clusters with relation to given modes using *mean shift*. In summary, *mean shift* is a clustering algorithm that finds the modes of the estimated density $\hat{f}(\mathbf{x})$.

Figure 2.2 presents basic idea behind *mean shift*. For each pixel, *mean shift* defines a window around it and computes the centroid of the data points in the fixed window. Then it shifts the center of the window to the centroid as the new initial window and computes the mean value iteratively until it arrives to the final centroid. In other words, the window shifts to a more denser region of the data set after each iteration until convergence. The convergence means the distance between previous mean and present mean is smaller than a given threshold.

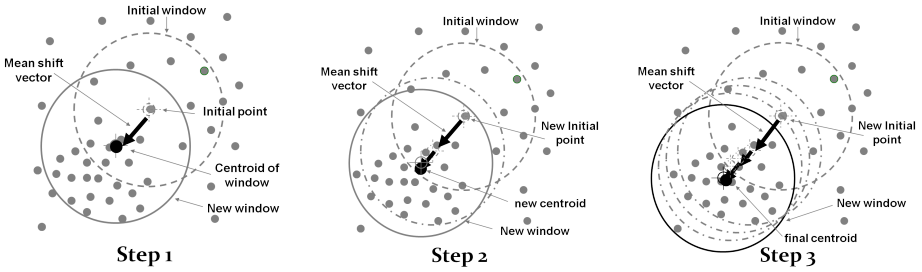

Figure 2.2: Intuitive description of Mean Shift.

2.5.2 Theoretical description of mean shift

As explained before, *mean shift* algorithm can be considered as a gradient ascent on the density function. This problem can be written as:

$$\nabla \hat{f}(\mathbf{x}) = 0 \tag{2.13}$$

Using Parzen windowing (a non-parametric kernel-based probability density function estimator), Fukunaga introduced in [Fukunaga 75] a gradient ascent algorithm that solves iteratively equation (2.13). The quantity $m(\mathbf{x})$ is called the *mean shift* vector(see the equation 2.14).

$$m(\mathbf{x}) = \mathbf{x}^{[t+1]} - \mathbf{x}^{[t]} = \frac{\sum_{i=1}^{n} g\big(d^2\big(\mathbf{x}^{[t]}, \mathbf{x}_i, \mathbf{H}\big)\big) .\mathbf{x}_i}{\sum_{i=1}^{n} g\big(d^2\big(\mathbf{x}^{[t]}, \mathbf{x}_i, \mathbf{H}\big)\big)} - \mathbf{x}^{[t]} \tag{2.14}$$

where t is the iteration variable, d is the Mahalanobis distance, $\mathbf{x}^{[0]}$ is set to a given $\mathbf{x}_i$ and $g(.)$ is a weight function deriving from the kernel function. In this work, the Epanechnikov kernel is employed thus $g(.) = -k'(.)$ which is a rectangular function.
Mean shift procedure can be summarized as, for a point $\mathbf{x}$,

1. Set $\mathbf{x}^{[0]}$ to the value of $\mathbf{x}$,
2. From equation 2.14, compute the *mean shift* vector $m(\mathbf{x}^{[t]})$,
3. Update $\mathbf{x}^{[t]}$ to $\mathbf{x}^{[t+1]}$ by shifting the density estimation window by $m(\mathbf{x}^{[t]})$,
4. Repeat till convergence: when $d\big(\mathbf{x}^{[t]}, \mathbf{x}^{[t+1]}, \mathbf{H}\big)$ is smaller than a given threshold value.

Thus, the $\mathbf{x}^{[t+1]}$ is the corresponding mode of the initial point $\mathbf{x}$.

2.6 Procedure of *mean shift* filtering

Our final segmentation approach includes two steps: *mean shift* filtering and clustering. In this section, we address the *mean shift* filtering step.

The modes obtained during the *mean shift* filtering represent the local features of images, and it will make clustering becomes much easier. Indeed the principle of mean shift filtering is a procedure of clustering which iteratively search for the modes. However, in the case of clustering, a second step is necessary, as it appears that using the mean shift filtering may not always reduce information enough, but may give rather close but different local maxima. *Mean shift* filtering is not a direct clustering method, but acts as a prelude to clustering [Comaniciu 02, Grenier 06]. In the following, we summarize the *mean shift* filtering procedures that will be employed in the thesis.

We use the joint spatial-range domain. Let us denote by $\mathbf{x}_s$ the spatial position and by $\mathbf{x}_r$ the range vector (*i.e.* the pixel values), then the vector $\mathbf{x}$ in the joint spatial-range domain is defined as: $\mathbf{x} = (\mathbf{x}_s, \mathbf{x}_r)$. As this vector, the bandwidth matrix $\mathbf{H}$ consists of two scale matrices: $[\mathbf{H}_s, \mathbf{H}_r]$, where $\mathbf{H}_s$ is spatial bandwidth matrix and $\mathbf{H}_r$ is range bandwidth matrix. The common bandwidth matrix $\mathbf{H}$ can be defined as

$$\mathbf{H} = \begin{bmatrix} \mathbf{H}_s & 0 \\ 0 & \mathbf{H}_r \end{bmatrix} \tag{2.15}$$

For a large number of *mean shift* applications, the two scale matrices $\mathbf{H}_s$ and $\mathbf{H}_r$ are diagonal. Indeed, the bandwidth matrix $\mathbf{H}$ is expressed as:

$$\mathbf{H} = \begin{bmatrix} {h_s}^2.\mathbf{I}^p & 0 \\ 0 & {h_r}^2.\mathbf{I}^q \end{bmatrix} \tag{2.16}$$

where h_s is the scalar value of spatial bandwidth, h_r is the scalar value of range bandwidth, $\mathbf{I}$ is the identity matrix, p is the number of spatial dimension (and so $\mathbf{x}_s \in \mathbb{R}^p$, $\mathbf{I}^p$ is a $p \times p$ matrix) and q is the number of range dimension of an image (and so $\mathbf{x}_r \in \mathbb{R}^q$, $\mathbf{I}^q$ is a $q \times q$ matrix). As example, for a RGB image, p is equal to 2 and q is equal to 3.

In order to preserve results from spatial discontinuity, as we would like to identify regions in the image, it is possible to include the space coordinates as parameters of the feature space. The expression of the kernel in one dimensional situation then becomes:

$$K(\mathbf{x}) = [\mathbf{x}_s \ \mathbf{x}_r] = \frac{c}{(h_s)^p.(h_r)^q} K\left(\left\|\frac{\mathbf{x}_s}{h_s}\right\|^2\right).K\left(\left\|\frac{\mathbf{x}_r}{h_r}\right\|^2\right) \tag{2.17}$$

A color image which includes three feature space components is taken here to illustrate the procedures of *mean shift* filtering algorithm. Let $\{\mathbf{x}_i\}_{i=1,2...n}$ and $\{\mathbf{z}_i\}_{i=1,2...n}$ the original and the filtered image points in the d-dimensional feature space, respectively. The *mean shift* filtering algorithm can be summarized as:

1. Initialize $\mathbf{x}^{[0]}$ to a given $\mathbf{x}_i$,
2. Initialize a bandwidth matrix $\mathbf{H} = \begin{bmatrix} {h_s}^2 & 0 & 0 & 0 & 0 \\ 0 & {h_s}^2 & 0 & 0 & 0 \\ 0 & 0 & {h_r}^2 & 0 & 0 \\ 0 & 0 & 0 & {h_r}^2 & 0 \\ 0 & 0 & 0 & 0 & {h_r}^2 \end{bmatrix}$,
3. Using equation (2.14), to compute $\mathbf{x}^{[t+1]}$ until convergence when $d\left(\mathbf{x}^{[t]}, \mathbf{x}^{[t+1]}, \mathbf{H}\right)$ is smaller than a given threshold value,
4. Assign to $\mathbf{z}_i$ the spatial position of $\mathbf{x}_i$ and the range values of $\mathbf{x}^{[t+1]}$, *e.g.* $\mathbf{z}_i = \left(\left(\mathbf{x}_i\right)_s, \left(\mathbf{x}^{[t+1]}\right)_r\right)$,
5. Repeat the above steps for each point $\mathbf{x}_i$ of the image.

The asymptotic time complexity of a naive *mean shift* implementation [1] is $O(n^2.{h_s}^2.\overline{it})$ where n is the number of data points in the data set, h_s is the spacial bandwidth parameter, and $\overline{it}$ is the average number of iterations [Li 10]. A large number of improvements have been made to the initial *mean shift* algorithm to improve its computational time [Domï£¡nguez 03, Carreira-Perpiï£¡ï£¡n 06, Wang 07, Freedman 09]. In the following, we use the naive implementation of *mean shift*.

2.7 Procedure of *mean shift* clustering

2.7.1 Introduction

Mean shift, if considered as its initial formulation [Fukunaga 75, Cheng 95], is a filtering approach. Based on equation 2.14, each processed point evolves iteratively to a new position and finally reach its closest mode. When using *mean shift* filtering, we expect that all filtered points $\mathbf{y}$ of a given object converge to a unique mode, assuming that the feature of the considered object is a single mode in the feature space. Thus, the clustering step (also known as merging or fusion

1. Considering a spatial-range separable kernel and a spatially bounded kernel.

step) is trivial and only consists into labelling all clusters... If we consider the well-used joint spatial-range domain as the feature space, this assumption is generally false for two reasons.

The first reason is link to the numerical precision and time consuming constraint during *mean shift* filtering step. The iterative process ends when the *mean shift* vector $\mathbf{y}^{[t+1]} - \mathbf{y}^{[t]}$ is smaller than a given threshold. This criterion does not ensure all the point convergence to the same local mode with an average distance error equal to the threshold value. Moreover, in some cases (i.e. unbounded kernels) this criterion is true after too much iteration and therefore the process is often stopped after a given number of iterations. The final points are not closed to each other with the desired distance.

The second reason comes from the use of the spatial feature. Consider a point $\mathbf{y}$ belonging to a homogeneous region. This point $\mathbf{y}$ is filtered by *mean shift* using a bounded kernel (corresponds to the general case and ensures the convergence of *mean shift* procedures) and a bandwidth matrix that limits the analysis to points belonging to the same homogeneous region. This point $\mathbf{y}$ is a mode since it will not evolve after the first iteration as all samples considered to compute its new position have the same range value than the point $\mathbf{y}$ (so all samples have the same weight) and, in average, their spatial mean (barycentre) is equal to the processed point $\mathbf{y}$. So, a homogeneous region of the input image consists of many modes having the same range value but different spatial positions.

Thank to these reasons, a segmentation step is needed to merge the filtered points together. This merging step can be introduced after the filtering step [Comaniciu 02, Grenier 06, Hong 07].

2.7.2 Segmentation or cluster delineation step

After the well cited *mean shift* filtering step, Comaniciu proposed to use a region adjacency graphs approach [Comaniciu 02] to segment color images. The clusters delineation in the joint domain is done by grouping together all the filtered points which are closer than h_s in the spatial domain, and h_r in the range domain. This process is applied for points, generating hundreds of clusters. So the authors proposed an optional step that eliminates the regions containing less than a given amount of pixels.

Hong [Hong 07] improves this step by employing new aspects: i) a global optimization criterion for the modes merging step to get a total energy-based segmentation and ii) an elimination of texture patches in order to remove small regions and refine the segmentation.

Considering our application, we use another approach based on the region growing scheme and a set of initial seeds. We need to produce binary segmentations: object of interest and background. The seeds are set in the object. This approach will be detailed in section 6.2.3.

Other segmentations methods for color images are detailed in the chapter five of the book [Fernandez-Maloigne 12]. For the general context of data clustering, the book [Gan 07] is a huge review of old to recent algorithms.

2.8 Drawbacks of *mean shift*

In contrast to K-$means$ clustering approach, *mean shift* does not need any assumption on number of clusters and shape of distribution. However, its performance highly relies on selection of scale parameters. The modes found do not adequately present the dense regions of the data set if a poor bandwidth estimate is used. Moreover, as selection of bandwidth parameters is an iterative process, *mean shift* suffered a problem of computational time as well [Li 10].

Bandwidth is the only parameter to tune through *mean shift* processing. Bandwidth selection has been applied most successfully for unidimensional data while for multidimensional data its development and implementation have been relatively limited. As for one dimension, bandwidth selection is the single value tuning case but more complex for multi-dimensional case as the bandwidth tuning change to the choice of each value in a matrix. Its selection is more difficult since the matrix contains different diagonal term and some of off-diagonal term which need to be taken into account [Duong 03, Chacï£¡n 09]. *Mean shift* may not work well in higher dimensions. For higher number of dimensions, the space can become sparse enough to compromise a proper *mean shift* convergence: many points will be considered by *mean shift* as local maxima increasing the number of clusters.

2.9 Conclusion

In this chapter, we pay attention to presenting *mean shift* which is a robust method in feature space. Moreover, we detailed the *mean shift* filtering procedures and its limitations.

In the next part, in order to improve *mean shift*, we will discuss the properties, *e.g.* noise, blur, correlation and color space, which could influence *mean shift* and how the *mean shift* affected by these factors.

The bandwidth selection is the only essential parameter which need to tune through *mean shift* filtering. A fixed bandwidth matrix selector for *mean shift* by using plug-in methods is developed. At the present time, most of the researchers concentrate on the restricted case of diagonal matrices for multivariate bandwidth selectors. Few consider about the unconstrained bandwidth case. In the following, we will discuss about the full matrix bandwidth in 1- and $3-$dimensional case. The higher dimension will be discussed in the future. We also take into account the effect of correlation among different dimensions.

II METHODOLOGICAL CONTRIBUTION on MEAN SHIFT FILTERING

Résumé

Les travaux méthodologiques de cette thèse se focalisent sur le filtrage *mean shift* qui est une méthode de filtrage cherchant à associer, à chaque point de l'image, la valeur la plus probable (mode) de la densité de probabilité. Cette approche est basée sur l'estimation non-paramétrique par noyau de la densité de probabilité et permet de travailler dans l'espace des caractéristiques : un espace multidimensionnel ou les échantillons (les pixels pour le traitement d'image) sont représentés par un point. Pour le traitement d'image, cet espace est généralement constitué de deux types de caractéristiques : une pour la position spatiale du pixel dans l'espace ; une pour les valeurs des intensités du pixel.

Les performances du filtrage *mean shift* sont très dépendantes des choix successifs à faire lors de la définition de l'espace des caractéristiques et de l'estimation non-paramétrique. Bien que les facteurs influençant ces performances soient connus, peu d'études ont cherché à les comprendre et à les optimiser dans le contexte général du traitement d'image ou en imagerie médicale dans le cadre du traitement de données multidimensionnel. Dans cette partie, nous étudierons ces facteurs.

Le chapitre 4 se focalise sur l'impact du bruit et du flou (filtrage passe bas) des images d'abord sur l'espace des caractéristiques, puis sur le filtrage *mean shift*. Cette étude se base sur une image synthétisée et les deux mesures utilisées pour quantifier ces impacts sont le PSNR et le SSIM (une mesure basée sur le système de vision humain). Par rapport à ces deux critères, on montre que le *mean shift* est robuste au bruit mais moins à la correction du flou.

La détermination des paramètres d'échelle fait l'objet du chapitre 5. Les paramètres d'échelle sont représentés par une matrice. Une méthode fréquemment utilisée dans les travaux sur les *mean shift* pour déterminer ces paramètres est la méthode du *plug-in*. Cette méthode permet, dans le contexte de l'estimation non paramétrique par noyau, de minimiser l'erreur quadratique moyenne asymptotique intégrée de l'estimation. Cependant cette approche est utilisée sans preuve en filtrage *mean shift* et seulement en monodimensionnel, c'est à dire jamais dans le cadre multidimensionnel où les matrices d'échelle sont diagonales ou pleines. De plus, cette approche ne permet pas d'op-

timiser le paramètre d'échelle spatial. Ces points constituent les développements proposés dans ce chapitre. Appliqué au filtrage *mean shift*, nos résultats montrent que : i) la méthode du *plug-in* multidimensionnel permet d'obtenir de meilleures performances que le *plug-in* monodimensionnel ; ii) dans le cadre multidimensionnel, les matrices diagonales donnent des résultats comparables à ceux obtenus avec des matrices pleines et que ces résultats sont proches des optima obtenus par une recherche exhaustive des paramètres d'échelle ; iii) le choix des paramètres d'échelle spatiales conditionne les performances du filtrage *mean shift* lorsque les paramètres d'échelle des intensités sont déterminés par l'approche du *plug-in*.

Dans le chapitre 6, nous proposons une nouvelle approche de segmentation reposant sur le filtrage *mean shift* et sur la croissance de région dont la connaissance précise des paramètres d'échelle de chaque méthode n'est plus nécessaire. Cette approche semi-automatique (le choix des intervalles pour les paramètres d'échelle ainsi que les germes initiaux de la croissance de région sont nécessaires) se base sur la création d'une carte de probabilité des segmentations effectuées. Par un simple seuillage, cette carte permet d'obtenir une segmentation moyenne. Nous vérifions les performances de cette approche et nos hypothèses en analysant les résultats obtenus sur une image de synthèse. Cette approche sera évaluée dans la partie III dans le contexte de l'ischémie cérébrale.

Chapter 3

Introduction of Methodological Contribution

Although some of the factors that influence the performance of *mean shift* are known, no study has set out to thoroughly investigate and optimize them in the context of general image processing and in the framework of multi-dimensional medical image processing. In part II, we aim at optimizing the *mean shift* process by analyzing the factors that influence it and optimizing its parameters.

In the chapter 4, we discuss the influence of noise and blurring on the *mean shift* process.

In chapter 5, a multi-parametric bandwidth estimation Plug-In method is employed on *mean shift* to automatically obtain the optimal global bandwidth parameters.

For the purpose of segmentation and clustering, in chapter 6, a new automated segmentation framework which combines *mean shift* filtering and *region growing* segmentation based on regular-grid sampling is proposed.

Chapter 4

Blurring and noise effect on Mean Shift Filtering

4.1 Introduction

Image restoration is one of the classical problems in image processing. Normally the degradation of an image is due to blurring effect and noise problem. It is formulated as:

$$\mathbf{I}(x,y) = \int\int \mathbf{J}(x,y)\, b(x,y;i,j) didj + \eta(x,y) \tag{4.1}$$

where $\mathbf{I}(x,y)$ is the observation, $\mathbf{J}(x,y)$ is the original clean image, degraded by blurring kernel $b(x,y;i,j)$, where i and j are integration variables linked to x and y, and $\eta(x,y)$ is the noise.

The image de-noising [Kervrann 06, Dabov 07, Kurimo 09] and de-blurring [Puetter 05, He 09] problems have been intensively investigated in a large number of research. However, their relative effect on image quality has not been studied in the same extent.

Mean shift is an advanced filtering algorithm processing multidimensional data in the feature space. This chapter is committed to understand the influence of noise and blurring on *mean shift* filtering algorithm.

Moreover, a debated issue for de-noising problem is to ask if there is a limit for de-noising performance [Chatterjee 10]. In this chapter, we also study this problem specifically for *mean shift* to know what is the limit of *mean shift* algorithm and how it can be improved.

We organized this chapter as follows: Firstly, the synthesized data is introduced in section 4.2. The noise and blurring effect on the synthesized data will be observed and discussed in feature space in section 4.3. In additional to the traditional image quality assessment PSNR, another

more human vision based assessment SSIM is explained in section 4.4 to realize the evaluation of image quality. In order to understand the *mean shift* restoration effect influenced by different characteristics of observation, *i.e.* the blurring, noise, the manually blurring and adding noise are performed on the synthesized data. A detailed *mean shift* filtering method is introduced in section 2.6 of chapter 2. We conduct this experiment and show results in section 4.6. At last, we present the conclusion in section 4.7.

4.2 Data and materials

In this section, we present the synthesized RGB data which consists in 3 simple R, G, B clusters. It is employed to illustrate the noise and blurring effect in feature space. Furthermore, it is used to discuss the influence of noise and blurring on *mean shift* filtering.

The synthesized RGB 3 clusters data, with size 64×64, is presented in chapter 2.3 for illustrating feature space. It is reused here to introduce effect of noise and blur based on feature space analysis.

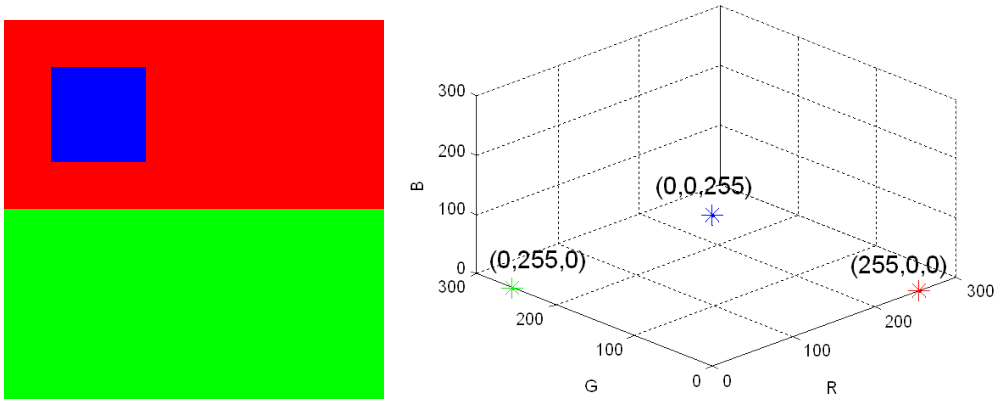

(a) RGB image. (b) Feature space.

Figure 4.1: Synthesized RGB data and its properties.

Figure 4.1(a) shows the synthesized RGB image. When there is no blurring and no noise, the synthesized RGB data in feature space is presented as 3 separated clusters in figure 4.1(b).

4.3 Effect of noise and blurring in feature space

In this section, we remind the synthesized RGB 3 clusters image to introduce influence of different noise and blurring as well as the influence of mixed blurring and noise on *mean shift* filtering in feature space. We consider the case of additional white Gaussian noise and Gaussian kernel blurring, although other noise distributions are equally applicable.

4.3.1 Only noise effect in feature space

The synthesized RGB image is corrupted by an additive uncorrelated Gaussian noise with zero mean and variance set to σ_N. We generate the uncorrelated gaussian noise which is added separately for each dimension of the image. Figure 4.2 presents the noise influence on synthesized RGB image when applied various noise with (a) $\sigma_N = 5$, (b) $\sigma_N = 20$, and (c) $\sigma_N = 50$. Due to an increasing noise effect, it can be shown in feature space that the original centered features gradually disperse (see figure 4.4 (d), (e) and (f)).

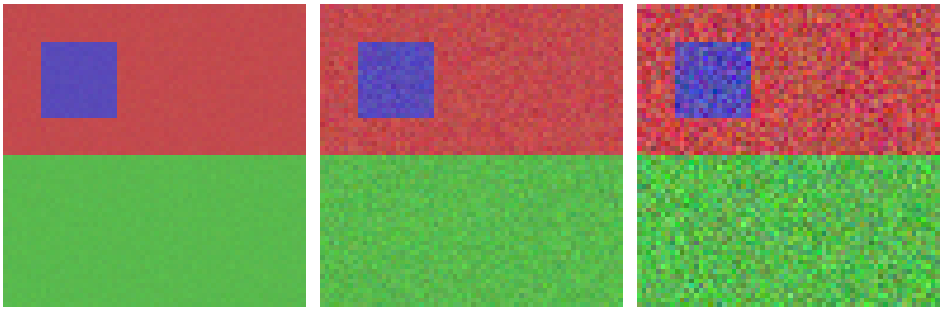

(a) Noisy image ($\sigma_N = 5$.) (b) Noisy image ($\sigma_N = 20$.) (c) Noisy image ($\sigma_N = 50$.)

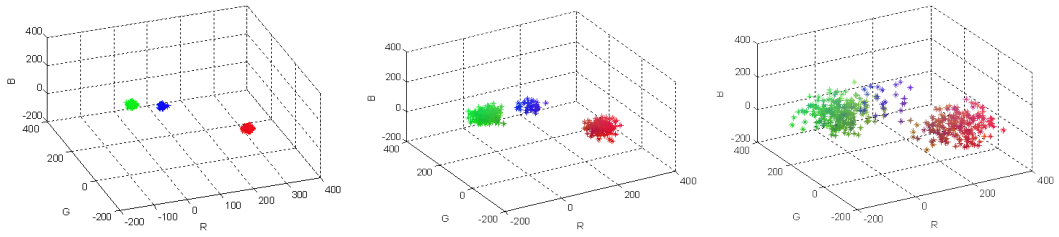

(d) Feature space ($\sigma_N = 5$.) (e) Feature space ($\sigma_N = 20$.) (f) Feature space ($\sigma_N = 50$.)

Figure 4.2: Noise effect on synthesized RGB data in feature space, the noisy images are observed with the same color map because the values after noise are over 255.

In this thesis, we only use the classically used Gaussian noise [1]. This noise is also used here to mimic the noise coming from MRI acquisition system [Nishimura 96]. MRI images are suffered by random noise and partial volume effect which limit the accuracy of any quantitative measurements for therapy and diagnosis. The noise assessment in MRI usually assumed as zero mean and Gaussian distributed [Aja-Fernandez 08].

4.3.2 Only blurring effect in feature space

The synthesized RGB image is blurred using a Gaussian lowpass filter. The Gaussian filter $\mathbf{B}[r_B, \sigma_B]$ is applied to the image by convolution of a square mask $[r_B, r_B]$ which coefficients value depend on σ_B.

Figure 4.3 shows the blurring influence on synthesized RGB image when applied Gaussian kernel with the mask size r_B=15 and various standard deviation: (a) $\sigma_B = 1$, (b) $\sigma_B = 3$, and (c)

1. Salt and pepper noise and outliers points, also present in our data, will be pre-processed (see chapter 10) using a dimension by dimension median filter.

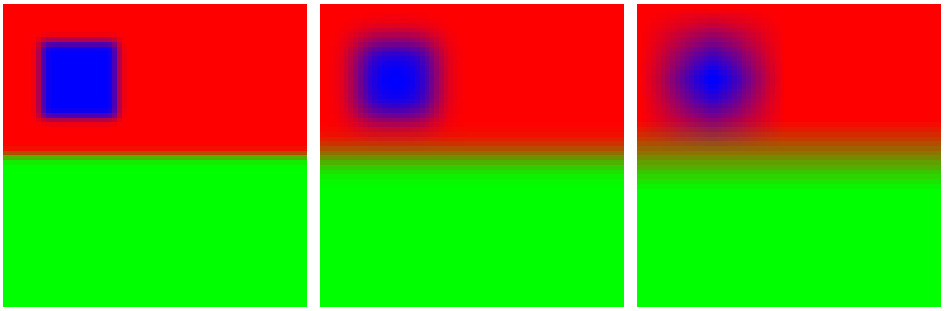

(a) Blurring image ($\sigma_B = 1.$)

(b) Blurring image ($\sigma_B = 3.$)

(c) Blurring image ($\sigma_B = 7.$)

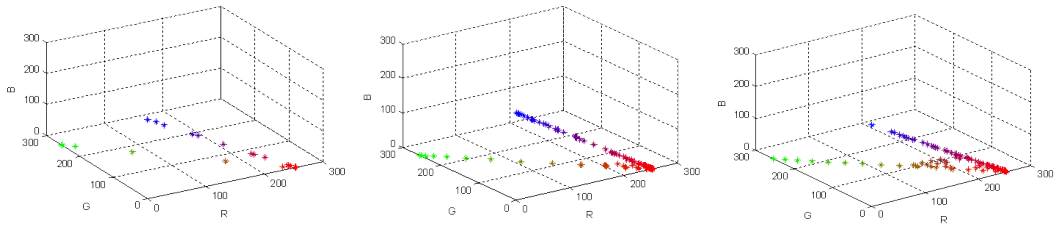

(d) Feature space ($\sigma_B = 1.$)

(e) Feature space ($\sigma_B = 3.$)

(f) Feature space ($\sigma_B = 7.$)

Figure 4.3: Blurring effect on synthesized data in feature space.

$\sigma_B = 7$. Due to an increasing blurring effect, the features move closer to each other and become more and more inseparable (from figure 4.3 (d), (e) to (f)).

4.3.3 Mixed Noise and blurring effect in feature space

This section, we discuss the mixed noise and blurring situation in order to simulate the real image which normally contains noise and blurring simultaneously.

As you can see, the figure4.4 (a), (b) and (c) are firstly blurred with identify Gaussian kernel $r_B = 15$ and $\sigma_B = 5$ (notated $\mathbf{B}[15, 5]$) and then are noised with various Gaussian noise: (a) $\sigma_N = 5$, (b) $\sigma_N = 20$, and (c) $\sigma_N = 50$. Figure 4.4(d), (e) and (f) are the feature space representations.

The figure 4.5 (a), (b) and (c) are first blurred with a Gaussian kernel (r_B=15) with various standard deviation: (a) $\sigma_B = 1$, (b) $\sigma_B = 3$ and (c) $\sigma_B = 7$, then adding the same Gaussian noise ($\sigma_N = 30$).

With both noise and blurring influence, the feature clusters are more complex to analyze. Apparently, between any two clusters, the more blurring and noise you have, the more difficulties you have to recognize the boundary. In the next section, the feasibility and robustness of *mean shift* filtering experiments are performed on various noise and blurring effect.

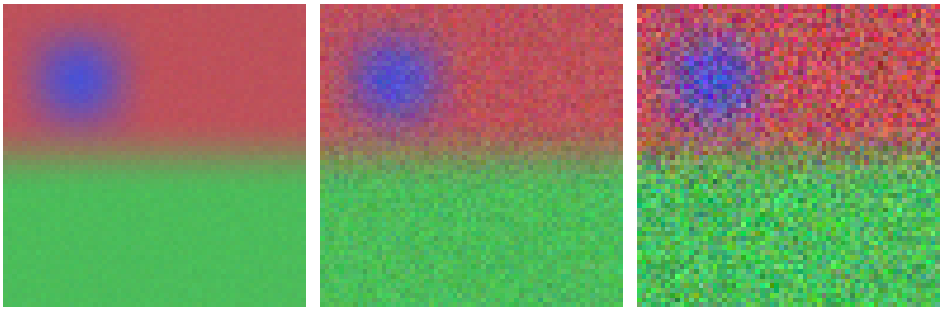

(a) Corrupted image ($\sigma_N = 5.$) (b) Corrupted image ($\sigma_N = 20.$) (c) Corrupted image ($\sigma_N = 50.$)

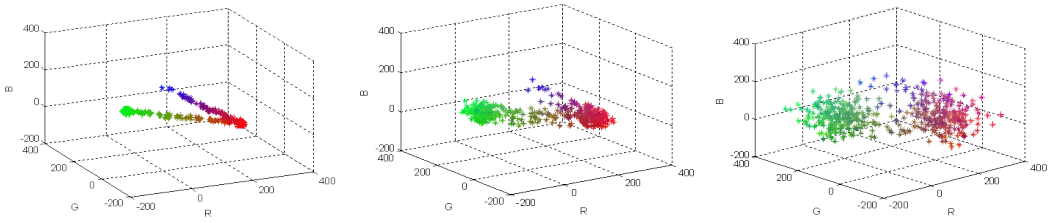

(d) Feature space ($\sigma_N = 5.$) (e) Feature space ($\sigma_N = 20.$) (f) Feature space ($\sigma_N = 50.$)

Figure 4.4: Influence of noise on synthesized data with fixed blurring $\boldsymbol{B}[15, 5]$ in feature space, the corrupted images are observed with the same color map because the values after noise are over 255.

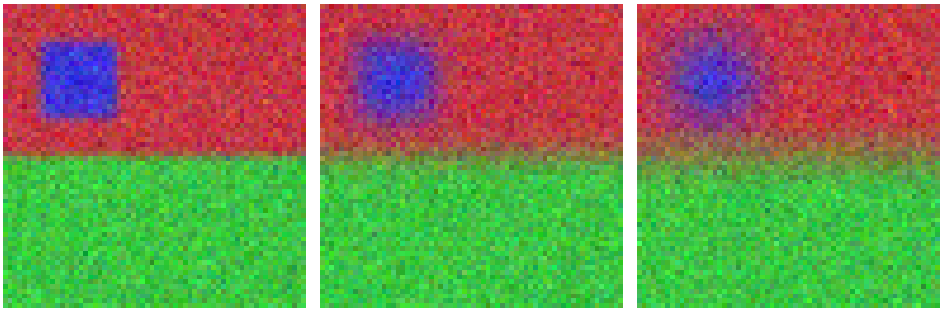

(a) Corrupted image ($\sigma_B = 1.$) (b) Corrupted image ($\sigma_B = 3.$) (c) Corrupted image ($\sigma_B = 7.$)

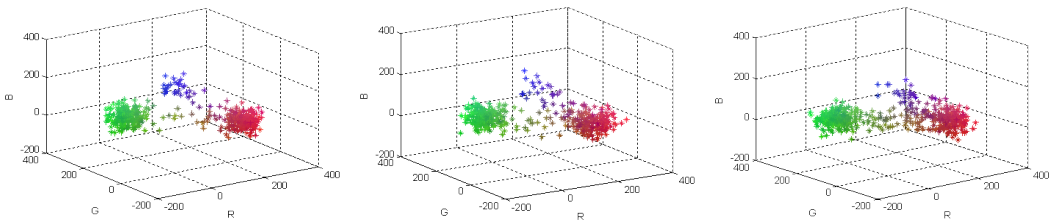

(d) Feature space ($\sigma_B = 1.$) (e) Feature space ($\sigma_B = 3.$) (f) Feature space ($\sigma_B = 7.$)

Figure 4.5: Influence of blurring on synthesized data with fixed noise $\sigma_N = 30$ in feature space, the corrupted images are observed with the same color map because the values after noise are over 255.

4.4 Image Quality Assessment

4.4.1 PSNR

The assessment of the filtering quality is performed using the Peak Signal Noise Ratio (PSNR) (eq. 4.3) for each *mean shift* filtered image and the original uncorrupted image (without noise and in the original range space). Let $\mathbf{X}$ and $\mathbf{Y}$ be two images of n pixels, as example the reference image (i.e. without noise) and the obtained image.

Since the Mean Square Error (MSE) is defined as:

$$MSE(\mathbf{X},\mathbf{Y}) = \frac{1}{n}\sum_{i=1}^{n} \|(\mathbf{x}_i)_r - (\mathbf{y}_i)_r\|^2 \tag{4.2}$$

where $(\mathbf{x}_i)_r$ is the d-component range vector of a pixel i of an image $\mathbf{X}$ and $range$ is the peak value of images. The PSNR (in dB) is computed as follow:

$$PSNR(\mathbf{X},\mathbf{Y}) = 10.\log_{10}\left(\frac{range^2}{MSE}\right) \tag{4.3}$$

The higher the PSNR is, the better the filtering quality is.

The reference PSNR^{ref} is also computed from noisy data and original data. This reference value (linked to σ^2 of the Gaussian noise added) allows us to evaluate the improvement of the filtering step.

4.4.2 SSIM

Besides the error sensitivity approach PSNR which is a normalized mathematical difference measurement to quantify image degradations, a universal structural similarity image measurement SSIM [Wang 02, Wang 04, Wang 09] based on the human vision system and degradation of structural information is applied here. The distortion metric is defined as a combination of three components: luminance distortion, contrast distortion, loss of correlation. Let $\mathbf{X}$ and $\mathbf{Y}$ be two gray level images of n pixels, the x_i and y_i are the values of each pixel of $\mathbf{X}$ and $\mathbf{Y}$, the fidelity index SSIM is then given by:

$$SSIM(\mathbf{X},\mathbf{Y}) = \frac{2\,\mu_{\mathbf{x}}\mu_{\mathbf{y}}}{\mu_{\mathbf{x}}^2+\mu_{\mathbf{y}}^2}\cdot\frac{2\,\sigma_{\mathbf{x}}\,\sigma_{\mathbf{y}}}{\sigma_{\mathbf{x}}^2+\,\sigma_{\mathbf{y}}^2}\cdot\frac{\sigma_{\mathbf{xy}}}{\sigma_{\mathbf{x}}\sigma_{\mathbf{y}}} \tag{4.4}$$

where

$$\mu_{\mathbf{x}} = \frac{1}{n}\sum_{i=1}^{n} x_i, \qquad \mu_{\mathbf{y}} = \frac{1}{n}\sum_{i=1}^{n} y_i$$

$$\sigma_{\mathbf{x}}^2 = \frac{1}{n-1}\sum_{i=1}^{n}(x_i-\mu_{\mathbf{x}})^2, \qquad \sigma_{\mathbf{y}}^2 = \frac{1}{n-1}\sum_{i=1}^{n}(y_i-\mu_{\mathbf{y}})^2$$

$$\sigma_{\mathbf{xy}} = \frac{1}{n-1}\sum_{i=1}^{n}(x_i-\mu_{\mathbf{x}})(y_i-\mu_y)$$

where $\mu_{\mathbf{x}}$ and $\mu_{\mathbf{y}}$ are respectively the means of $\mathbf{x}$ and $\mathbf{y}$, $\sigma_{\mathbf{x}}$ and $\sigma_{\mathbf{y}}$ are respectively the local standard deviations of $\mathbf{x}$ and $\mathbf{y}$, and $\sigma_{\mathbf{xy}}$ is the cross correlation of $\mathbf{x}$ and $\mathbf{y}$ after removing their means.

The dynamic range of SSIM is $[0, 1]$. The first component in equation 4.4 measures how close the mean luminance of both images are. The second component measures how similar the contrast of both images are and the third component detects the degree of linear correlation between the two images.

For color image, we firstly calculate the SSIM for each dimension, then compute the mean of SSIM obtained from each dimension as the global SSIM.

4.5 Exhaustive search for MS

Instead of selecting objectively bandwidth matrix, we employ the exhaustive search (ES) method which sweeps all the possible bandwidth matrix for selecting the bandwidth matrix of *mean shift* filtering. We search the optimal bandwidth matrix using only two values (h_s for spatial bandwidth parameter and h_r for range bandwidth parameter) which are extensively used in *mean shift* applications. Here, h_s varies from 1 to 10 using an interval of 1 and h_r varies from 10 to 250 using an interval of 10. The optimal PSNR (PSNR^*_{MS}) and optimal SSIM(SSIM^*_{MS}) are obtained by calculating the filtered results with the clean reference input data.

4.6 Results and discussion

In this section, we discuss the experimental results where we calculate PSNR and SSIM of various blurring and effect influence on *mean shift* filtering. To start this section, we firstly introduce results obtained on only noise evolution and only blurring evolution. We then show results obtained using mixed noise and blurring.

The *mean shift* filtering is performed on synthesized RGB image. For *mean shift* filtering, we employ a similarity measurement the Mahalanobis distance and Epanechnikov kernel. As a vector, the bandwidth matrix $\mathbf{H}$ consists of two kinds of values: h_s for the spatial scale and h_r for the range scales [Grenier 06]. Also, the Cartesian-Grid based method for selecting bandwidth is applied for acquiring a series of filtered results. Here, h_s varies from 1 to 12 using an interval of 2 and h_r varies from 10 to 240 using an interval of 20.

Here, we assume that the uncorrupted data is available in order to estimate how well the synthesized noised and blurring data can be ideally denoised and deblurred. The PSNR^{ref} and SSIM^{ref} are computed from various noised images with the uncorrupted one. A series of PSNR_{MS} and SSIM_{MS} are computed from the filtered results with the uncorrupted image. The '$*$' in PSNR^*_{MS} and SSIM^*_{MS} means optimal one as well as in (h^*_s, h^*_r), it means optimal bandwidth parameter.

4.6.1 Only noise effect on MSF

The noise influence on MSF is discussed in this subsection according to PSNR and SSIM.

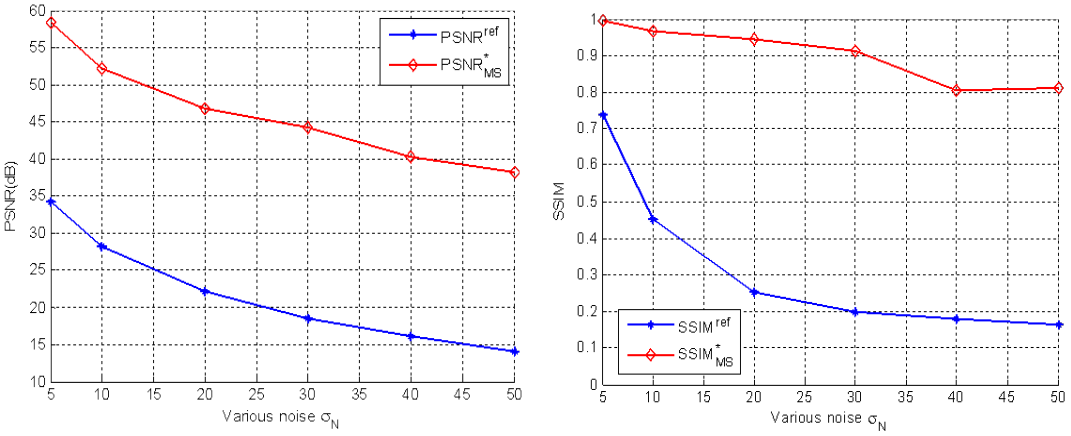

(a) PSNR. (b) SSIM.

Figure 4.6: PSNR and SSIM evolution according to various noise on MSF.

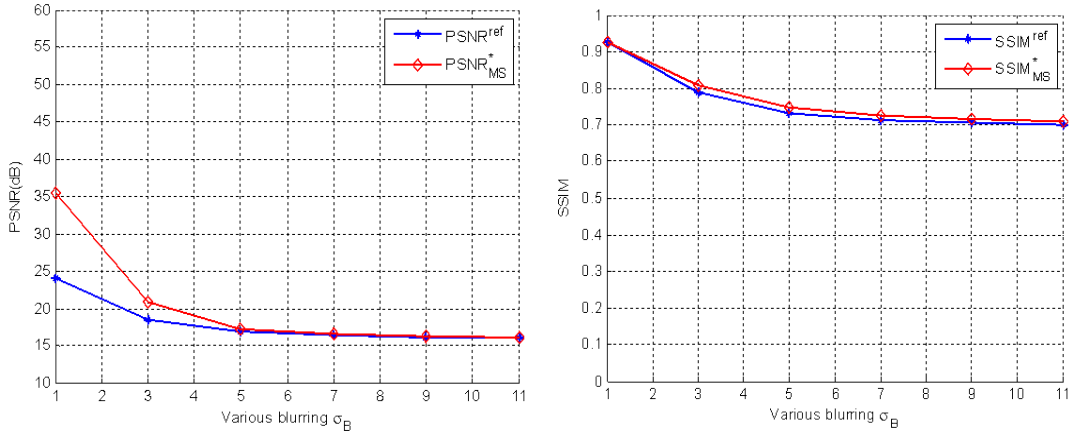

(a) PSNR. (b) SSIM.

Figure 4.7: PSNR and SSIM evolution according to various blurring on MSF.

From figure 4.6 (a), we can see that PSNR^{ref} decreases as the larger of the variance of noise. As the increase of noise, the obtained PSNR$^{*}_{MS}$ also decreases. The *mean shift* performs well as difference between PSNR^{ref} and PSNR$^{*}_{MS}$ remains constant along the increase of the variance of noise.

From figure 4.6 (b), the SSIM^{ref} also decreases as the increase of noise but decreases sharper compared to PSNR^{ref} before $\sigma_N = 20$. It shows that the SSIM is more sensible to the noise effect than PSNR from vision perceived preservation. The optimal SSIM$^{*}_{MS}$ decrease slightly and linearly as the increase of noise except for one value ($\sigma_N = 40$).

4.6.2 Only blurring effect on MSF

Another experiment is performed on various blurring effect on MSF (see figure 4.7).

One can note the low value of the PSNR measured for small σ_B values. Even if such blur impact a few amount of pixels, the intensities modifications impact well the PSNR value (the

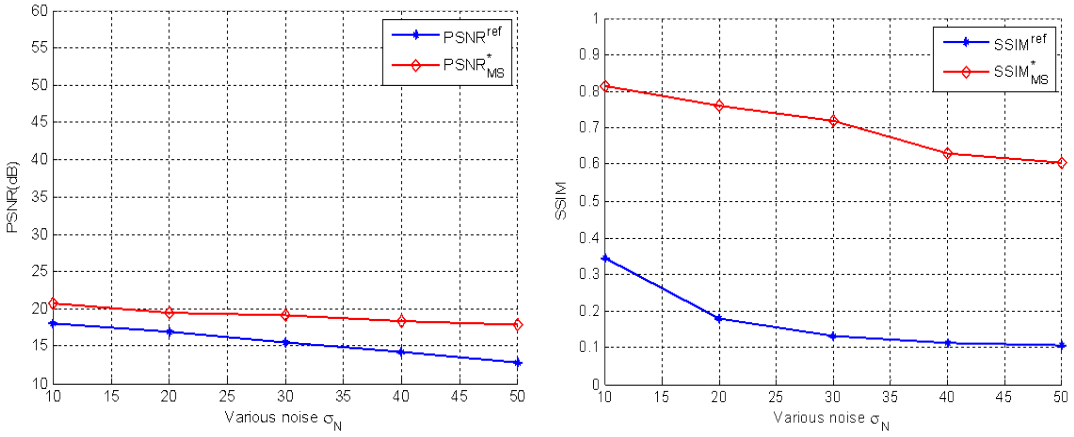

(a) PSNR. (b) SSIM.

Figure 4.8: PSNR and SSIM evolution according to various noise with $\boldsymbol{B}[15, 3]$ *on MSF.*

MSE increase drastically). With the increase of blurring, the quality of image is getting worse as shown by PSNR^{ref} and SSIM^{ref}. The PSNR^{*}_{MS} improves a lot until $\sigma_B = 3$ but improves slightly after. The improvement of *mean shift* filtering is worse and worse gradually arrive to 0 limit compared to PSNR^{ref}. The improvement is not so obvious based on PSNR^{*}_{MS} and SSIM^{*}_{MS} observations. It shows the limitation of *mean shift* filtering to recover blurring effect.

4.6.3 Mixed blurring and noise on MSF

Since the natural restoration refers noise and blurring effect at the same time. Here, we discuss the mixed influence of noise and blurring on *mean shift* filtering.

The synthesized RGB image is firstly Gaussian blurred with kernel $r_B = 15$ and standard deviation $\sigma_B = 3$ (noted as $\mathbf{B}[15, 3]$), then Gaussian noised with various standard deviation(see figure 4.8).

In another way, the synthesized RGB image is firstly Gaussian blurred with $r_B = 15$ and various standard deviation from $\sigma_B = 1$ to $\sigma_B = 11$, then Gaussian noised with ($\sigma_N = 30$). Figure 4.8 shows the PSNR^{*}_{MS} and SSIM^{*}_{MS} performance according to various blurring effect on *mean shift* filtering.

Based on both PSNR and SSIM, compared to only noise and only blurring situation, the mixed noise and blurring is more complex which make the improvement of *mean shift* decrease along with the increase of noise and blurring.

From figure 4.8(a) and figure 4.9(a), along the increase of noise and blurring, the feature space becomes more and more inseparable. The improvement of filtering quality goes up with increase in the noising and goes down with increase in the blurring according to PSNR assessment. This proves that *mean shift* is very robust and efficient on noise variation but has the limitation with a certain blurring effect.

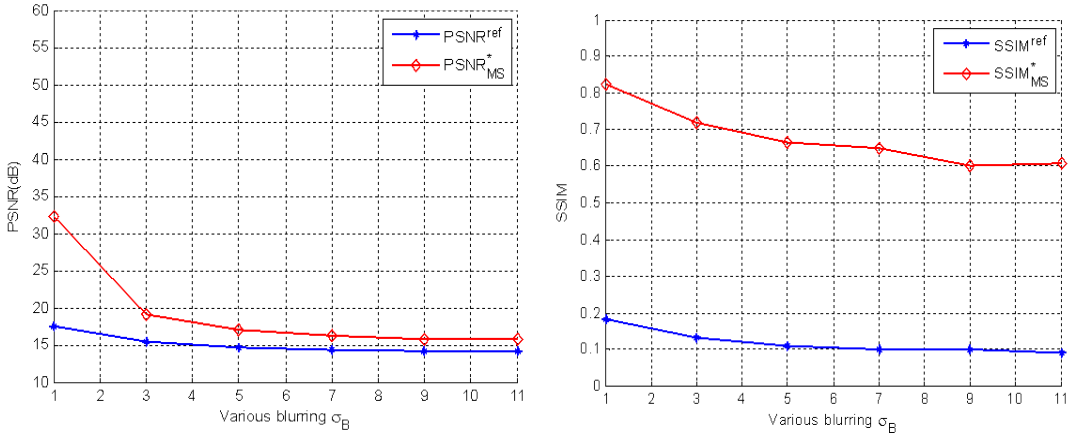

(a) PSNR. (b) SSIM.

Figure 4.9: PSNR and SSIM evolution according to various blurring with fixed noise $(\sigma_N = 30)$ *on MSF.*

4.7 Conclusion

In this section, we give the summary of conclusions as follows:

1. Both the noise and blurring influence are studied separately based on the synthesized three clusters data in the feature space. Also, the mixed effect of noise and blurring is studied to better understand their relative influence in feature space.
2. By summarizing optimal *mean shift* filtered results on various noise and blurring corrupted data, we conclude *mean shift* filtering is robust and efficient on noise effect but not so feasible on recovering blurring effect.
3. Besides measurement PSNR, the SSIM is employed for quantifying the *mean shift* filtering results from the perceived aspect. It is observed that PSNR and SSIM appear to improve after *mean shift* filtering. Thus, both of these two measurements will be used in the future work.

Chapter 5

Bandwidth optimization on Mean Shift Filtering

5.1 Introduction

Non-parametric kernel density estimation is a standard method in data-analysis. However, how to assess the quality of the estimation, how to select the optimal bandwidth matrix are still the debated points to the type of orientation of the kernel density function. Inspired by expanding Mean Integrated Square Error (MISE), Rudemo [Rudemo 82] and Bowman [Bowman 84] proposed the Least Squared Cross-Validation (LSCV) which can be minimized to estimate bandwidth. Zhang [Zhang 06] provided Markov chain Monte Carlo (MCMC) algorithms to estimate optimal bandwidth matrices for multivariate kernel density estimation. Scott, Tapia and Thompson [Scott 77] proposed *Plug-In* (PI) bandwidth selector which focuses on plugging to estimate of unknown quantities for obtaining estimated $\mathbf{H}$. Jones [Jones 96, Sheather 91] suggested PI method as being the best in terms of overall performance.

Mean shift procedures can be considered based on gradient ascent on the kernel density estimation to iteratively find the modes. During the procedures of *mean shift* filtering, bandwidths matrices including spatial bandwidth and range bandwidth are the most essential parameters used for mode detection [Comaniciu 02]. The bandwidth matrix $\mathbf{H}$ consists of two kinds of values: $\mathbf{H}_s$ for the spatial scale and $\mathbf{H}_r$ for the range scales. One dimensional *Plug-In* method (PI_{1D}) [Jones 96] for optimizing $\mathbf{H}_r$ had been applied to *mean shift* in several works as [Comaniciu 01, Comaniciu 03, Grenier 05b]. In these works, based on one dimensional case, authors assume that optimal range scale bandwidth matrices of density estimation give optimal results for *mean shift*

approaches.

However, there is no multivariate PI method using for *mean shift* approaches. PI_{1D} method is employed for multi-dimensional case in each dimension [Hong 07] which does not take into account correlation among dimensions. In this chapter, we proposed the bandwidth matrix estimation method based on multi-variate (PI_{ND}) for *mean shift* filtering.

Besides the matrix presented as $\mathbf{H}_r = {h_r}^2.\mathbf{I}^q$ in section 2.6, most of multivariate bandwidth selectors of kernel density estimation are focused on diagonal matrix (*e.g.* natural color images):

$$\mathbf{H}_r = \begin{bmatrix} {h_1}^2 & 0 & 0 \\ 0 & {h_2}^2 & 0 \\ 0 & 0 & {h_3}^2 \end{bmatrix} \tag{5.1}$$

Few studies focus on the class of full matrix:

$$\mathbf{H}_r = \begin{bmatrix} {h_1}^2 & {h_{12}}^2 & {h_{13}}^2 \\ {h_{12}}^2 & {h_2}^2 & {h_{23}}^2 \\ {h_{13}}^2 & {h_{23}}^2 & {h_2}^2 \end{bmatrix} \tag{5.2}$$

The purpose of this section is to concentrate how the PI bandwidth selector performs in relation to real color images and synthesized data set and the difficulties of PI method at hand. Firstly, the PI_{1D} method is employed one dimension to one dimension for *mean shift* bandwidth estimations. We perform multivariate bandwidth PI method for optimizing $\mathbf{H}_r$ using diagonal matrix (noted as PI_{Diag}) and full matrix (noted as PI_{Full}). The exhaustive search is employed for selection of $\mathbf{H}_s$.

We organize this chapter as follows: firstly, section 5.2 introduces the PI method and error criteria used for optimizing the bandwidth matrix. Secondly, the data and various PI experiments are described in section 5.3 and section 5.4. Thirdly, in section 5.5, a synthesized example of bandwidth influence on *mean shift* filtering is illustrated. Also, various PI results on natural images and synthesized images are described. Finally, we summarize the conclusion in section 5.6.

5.2 Error criteria

The bandwidth matrix plays a vital role in the performance of the kernel density estimators as well as in *mean shift* filtering. Thus we must have suitable error criteria to measure if the selected bandwidths give the optimal performance. The performance is conducted by the closeness of a kernel density estimate $\hat{f}\left(\mathbf{x};\mathbf{H}\right)$ to its target density $f(\mathbf{x})$. The Integrated Squared Error (ISE) is a common used global error criterion described as follows:

$$ISE\left\{\hat{f}(\cdot;\mathbf{H})\right\} = \int_{R^d}\left[\hat{f}\left(\mathbf{x};\mathbf{H}\right) - f(\mathbf{x})\right]^2 d\mathbf{x} \tag{5.3}$$

An alternative version is the Mean Integrated Squared Error (MISE) since ISE is a random variable,

$$MISE\left\{\hat{f}(\cdot;\mathbf{H})\right\} = \mathrm{E}\int_{R^d}\left[\hat{f}\left(\mathbf{x};\mathbf{H}\right) - f(\mathbf{x})\right]^2 d\mathbf{x} \tag{5.4}$$

There are also many possibilities that may be used, such as the Mean Integrated Absolute Error (MIAE) and the Mean Hellinger Distance (MHD). However, the MISE is the most frequently used and the most mathematically tractable criteria. It also allows to see the variance-bias trade off (see equation 5.5) that occurs when selecting a bandwidth.

$$MISE\left\{\hat{f}(\cdot;\mathbf{H})\right\} = Var\left\{\hat{f}(\cdot;\mathbf{H})\right\} + Bias^2\left\{\hat{f}(\cdot;\mathbf{H})\right\} \tag{5.5}$$

Here, we choose MISE because it is easy to analyze. Thus, we need to optimize the bandwidth by finding the value of $\mathbf{H}$ which minimizes the MISE.

$$\mathbf{H}_{MISE} = \underset{\mathbf{H}\in\mathbb{H}}{\arg\min}\, MISE\hat{f}(\cdot;\mathbf{H}) \tag{5.6}$$

The denoted $\mathbf{H}_{MISE}$ is the optimal bandwidth with respect to MISE. Mathematically speaking, $\mathbf{H}$ which belongs to $\mathbb{H}$ is a real symmetric positive definite matrix $\mathbf{H} = \mathbf{A}\mathbf{A}^T$. In a summary, MISE measures how well $\hat{f}$ estimate the true density f according to selection of bandwidth. However, it is difficult to find $\mathbf{H}_{MISE}$ because MISE does not have a closed form. To solve this problem, the Asymptotic Mean Integrated Squared Error (AMISE) is proposed in [Wand 95] to asymptotically approximate the MISE for large sample sets.

Wand's assumptions on f, $\mathbf{H}$ and K for the AMISE approximations are:

1. Each entry of the Hessian matrix $\mathcal{H}_f(.)$ of f is piecewise continuous and square integrable.
2. $\mathbf{H} = \mathbf{H}_n$ is a sequence of bandwidth matrices such that $n^{-1}\left|\mathbf{H}\right|^{-1/2}$ and all entries of $\mathbf{H}$ approach zero as $n \to \infty$.
3. K is a bounded, compactly supported d-variate kernel satisfying equation 2.5 discussed in section 2.4.3.

Then the AMISE of the multivariate kernel density estimator is given by

$$\begin{aligned} AMISE\left\{\hat{f}(.;\mathbf{H})\right\} &= n^{-1}\left|\mathbf{H}\right|^{-1/2} R(K) \\ &+\frac{1}{4}\mu_2(K)^2 \int \mathrm{tr}^2\left\{\mathbf{H}\mathcal{H}_f(\mathbf{x})\right\} d\mathbf{x} \end{aligned} \tag{5.7}$$

where $\mathcal{H}_f$ is the $d \times d$ Hessian matrix of f, $R(K) = \int K(\mathbf{z})^2 d\mathbf{z}$, $\mathrm{tr}(\mathbf{A})$ is the trace of the square matrix $\mathbf{A}$, n is the number of samples extracted from f and d is the number of dimensions. The first part in equation 5.7 corresponds to the integrated variance, while the second term corresponds to the integrated squared bias. AMISE is minimized by balancing variance and bias when selecting a bandwidth. Since results of $R(K)$ is a constant, the asymptotic variance decreases and asymptotic bias increases as $\mathbf{H}$ increases, which emphasizes again the important role the bandwidth plays in kernel density estimation.

As an example, for the univariate case $\mathbf{H}$ is set to h^2, the equation 5.7 is

$$AMISE\{\hat{f}(.;h)\} = n^{-1}h^{-1}R(K) + \frac{1}{4}h^4\mu_2(K)^2R(f^{(2)}) \tag{5.8}$$

where $f^{(2)}$ is the second derivative of f and $R(\cdot)$ is the general integrated squared density functional:

$$R(f^{(s)}) = \int f^{(s)}(x)^2 dx \tag{5.9}$$

Thus, the next step is to find an estimate of $R(f^{(2)})$, from the data and then find its minimizer *e.g.*

$$\hat{h}_{AMISE} = \arg\min_{h \in \mathbb{R}} AMISE(\hat{f}\cdot; h) = [\frac{R(K)}{n\mu_2(K)^2 R(f^{(2)})}]^{1/5} \tag{5.10}$$

which is called bandwidth selector.

Using integration by parts and under sufficient smoothness assumptions on f, we obtain:

$$R(f^{(s)}) = (-1)^s \int f^{(2s)}(x) f(x) dx \tag{5.11}$$

Thus, it is sufficient to calculate the estimation of functions of the form:

$$\Psi_r = \int f^{(r)}(x) f(x) dx \tag{5.12}$$

for r even as the sign of Ψ_{2s} is the same as that of $(-1)^s$ and $\Psi_r = 0$ if r is odd. The equation 5.12 could be transformed into:

$$\Psi_r = E\{f^{(r)}(X)\} \tag{5.13}$$

This motivates the estimator

$$\hat{\Psi}_r(g) = n^{-1} \sum_{i=1}^{n} \hat{f}^{(r)}(X_i; g) = n^{-2} \sum_{i=1}^{n} \sum_{j=1}^{n} L_g^{(r)}(X_i - X_j) \tag{5.14}$$

Here, g is a pilot bandwidth and L is kernel which are different from h and K. In terms of the Ψ_r function the AMISE-optimal bandwidth is:

$$h_{AMISE} = [\frac{R(K)}{n\mu_2(K)^2 \Psi_4}]^{1/5} \tag{5.15}$$

Replacement of Ψ_4 by the kernel estimator $\hat{\Psi}_4(g)$ arises the *Plug-In* rule:

$$\hat{h}_{PI} = [\frac{R(K)}{n\mu_2(K)^2 \hat{\Psi}_4(g)}]^{1/5} \tag{5.16}$$

However, the estimated bandwidth still depends on the choice of $\Psi_4(g)$ or pilot bandwidth g. One method of selecting g is continuing to use equation 5.14 for estimating $\Psi_4(g)$. With the same second-order kernel K in $\Psi_4(g)$, the estimation can be expressed with $\Psi_6(g)$. However, the rule for choosing $\Psi_6(g)$ still need using another kernel estimate and its optimal bandwidth depends on $\Psi_8(g)$. Therefore, this problem will not stop until we find the $\Psi_{n+2}(g)$ that could estimate $\Psi_n(g)$. That is why *Plug-In* get its name.

The problem can be solved by using a known *normal scale* bandwidth selector simply and quickly to estimate the Ψ_r function. A direct PI rule involving l successive kernel functional estimation is employed to select the $\hat{h}_{PI}$. Theoretical considerations [Wand 95], taking l to be at least 2 is a common choice. Moreover, after many derivations, the pdf is assumed to be gaussian distribution.

Finally, use the bandwidth $\hat{h}_{PI}$ to calculate $\Psi_8(g)$, then take this estimate iteratively to compute $\Psi_6(g)$, etc, then plug $\Psi_4(g)$ into equation 5.8 to obtain $\hat{h}_{AMISE}$.

The reader can consult [Wand 95] for univariate PI method and [Duong 03, Duong 07] for more details on multi-variate PI methods.

5.3 Data

Two synthesized data and four natural images (Lena, Mandrill, Peppers, Lake)are employed for the experiment of PI.

5.3.1 Synthesized Tito image

The synthesized data 'Tito' (see figure5.1)(a) is obtained form 8 classes of homogeneous color. The size of 'Tito' image is 512×512. Figure 5.1 shows the 8 clusters in the feature space.

The corrupted data is blurred with Gaussian shaped kernel $\mathbf{B}[63, 5]$, then corrupted by an additive uncorrelated Gaussian noise with $\sigma_N = 30$.

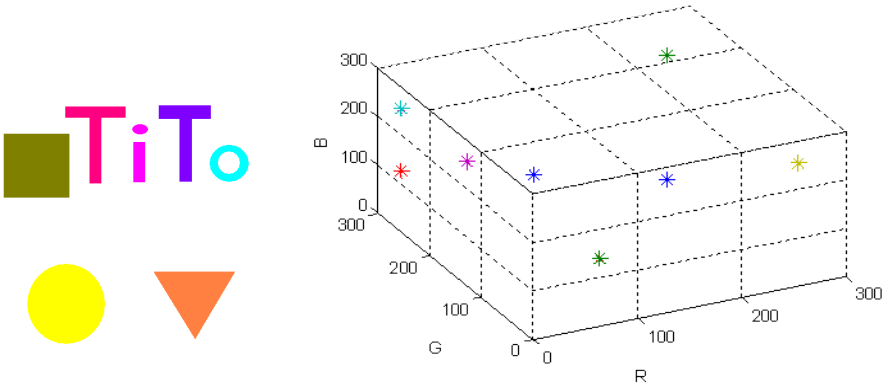

(a) Tito image. (b) Feature space.

Figure 5.1: Synthesized Tito data and its properties.

5.3.2 Synthesized MRI image

The synthesized MRI comprises a set of 10 clusters (see Figure 5.2(a)) that give the homogeneous tissue components, *e.g.* fat, white matter, cerebrospinal fluid, bone, etc. within each voxel, where each voxel may contains one or more tissue types as well as the geometric information (see Figure 5.2(b)). The T1, T2 and proton density used for the tissue types are from the Montreal

data set [Yoder 04]. The resolution of 'MRI' image is 256×256 pixels. The T1, T2, and proton density values are all normalized between [0,255].

(a) RGB coded image with T1, T2, proton density.

Tissue type	R: T_1 (ms)	G: T_2 (ms)	B: Proton density
Air	0	0	0
Connective	500	70	0.77
CSF	2569	329	1
Fat	350	70	1
Glial Matter	833	83	0.86
Gray Matter	833	83	0.86
Muscle	900	47	1
Skin	2569	329	1
Bone	0	0	0
White Matter	500	70	0.77

(b) The T1, T2 proton density used for the tissue types from the Montreal data set.

Figure 5.2: Synthesized MRI data and its properties.

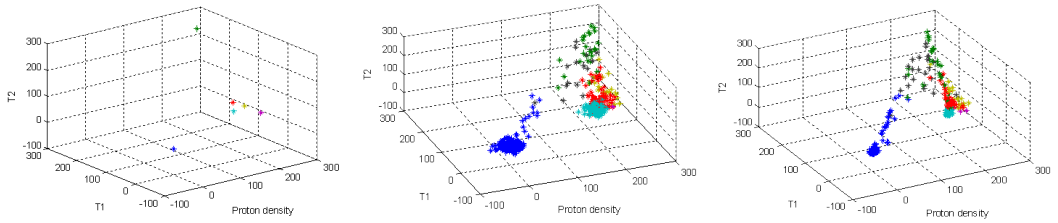

(a) Original data. (b) Corrupted data. (c) After mean shift filtering.

Figure 5.3: Feature space representation of synthesized MRI data.

Figure 5.3(a) shows original synthesized MRI which contains ten clusters corresponding to various tissues. We add blur and noise to simulate real image or medical image. The corrupted data (see Figure 5.3(b)) is obtained by firstly applying a blur effect with a Gaussian shaped kernel $\mathbf{B}[63, 1]$, then adding a Gaussian noise with $\sigma_N = 10$.

5.3.3 Natural images

In order to evaluate the robustness of *mean shift* against correlation and linear space transformations, we use natural color images. Each of them is a 3-dimensional vector as RGB.

The data set consists of a set of four well studied natural RGB color images with size 512×512 pixels (*e.g.* Lena, Mandrill, Peppers, Lake). These images are corrupted by an uncorrelated Gaussian noise with $\sigma_N = 30$.

(a) *Lena* (b) *Mandrill*

(c) *Peppers* (d) *Lake*

Figure 5.4: Natural RGB images.

5.4 Description of and experiment

5.4.1 PI bandwidth selectors

We use univariate PI bandwidth selector (PI_{1D}) dimensional by dimensional for color image in package "KernSmooth" (http://cran.r-project.org/). Additionally, we employ R package "ks" [Duong 07] which implements PI_{1D} concluding diagonal matrix (PI_{Diag}) and full matrix (PI_{Full}) for kernel density estimation, which is applied to multivariate (2 to 6) kernel discriminant analysis.

As example, in this study we will consider 2D RGB image. Then the bandwidth matrix is given by:

$$\mathbf{H} = \begin{bmatrix} \mathbf{H}_s & 0 \\ 0 & \mathbf{H}_r \end{bmatrix} \tag{5.17}$$

Note that commonly used scale matrices $\mathbf{H_s}$ for *mean shift* filtering approaches consist of two parameters only. The type of range bandwidth matrix $\mathbf{H_r}$ for PI method are categorized into three part:

1. PI for each dimension separately (PI_{1D}),
2. Diagonal matrix (PI_{Diag}),
3. Full matrix (PI_{Full}).

It is noted that PI method estimation is only for range parameters, thus we need to optimize spatial parameters by an exhaustive search (from 1 to 5 step 1).

In order to better estimate the $\mathbf{H_r}$, the number of samples n (in equation 5.7) is another factor which could influence the effect of PI method. During this experiment, we also conduct the PI experiments according to various number of samples.

5.4.2 Exhaustive search

The results of PI_{1D}, PI_{Diag}, PI_{Full} will be compared with the results of exhaustive search (ES) method. The exhaustive search which sweep over the possible spacial and range bandwidth parameters. The exhaustive search is detailed in section 4.5.

For each scale bandwidth parameters, the PSNR, SSIM are computed.

5.5 Results and discussion

5.5.1 Illustration of bandwidth influence on MSF

In this subsection, we firstly employ the simulated MRI data to illustrate how bandwidth matrix influence *mean shift* filtering. We assessed the filtered results of *mean shift* filtering by using PSNR. The spatial bandwidth and range bandwidth are discussed separately based on the exhaustive search bandwidth selection.

This data is degenerated by blurring ($\mathbf{B}[63, 1]$) and adding noise ($\sigma_N = 10$) , see the figure 5.5(a) is the original MRI data and figure 5.5(e) is corrupted data, figure 5.5(b),(c) and (d) are filtered results obtained from the fixed h_s=2 but different h_r along the range $[1, 255]$, (c) is the optimal *mean shift* filtered result with PSNR=26.19dB. Figure 5.5(f),(g) and (h) are filtered results obtained from the fixed h_r=80 but different h_r along the range $[1, 5]$.

It could be clearly seen that the data is deblurred and denoised. If bandwidth parameters are too large, filtering results will be over-smoothed and many details will be lost. If bandwidth parameters are too small, edges and details will be better preserved the better but the noise will be preserved which could be seriously influence the further segmentation step. Thus, the bandwidth parameters need to be adjusted carefully.

Figure 5.6 shows the different h_s evolution along the h_r from 20 to 240. As the increase of h_s, the PSNR value decrease gradually fast. Figure 5.7 extends h_s from 1 to 10 along h_r from 5 to 100. Here, according the analysis of spatial and range bandwidth parameters, we assumed the spacial bandwidth parameters to be small and we will use the value between 1 to 5 since after $h_s = 5$, the improvement is suffered a sharply decrease estimating by PSNR. For range bandwidth parameters, we will employ the value between 5 and 100. The experiments on synthesized MRI data illustrates the importance of bandwidth selection.

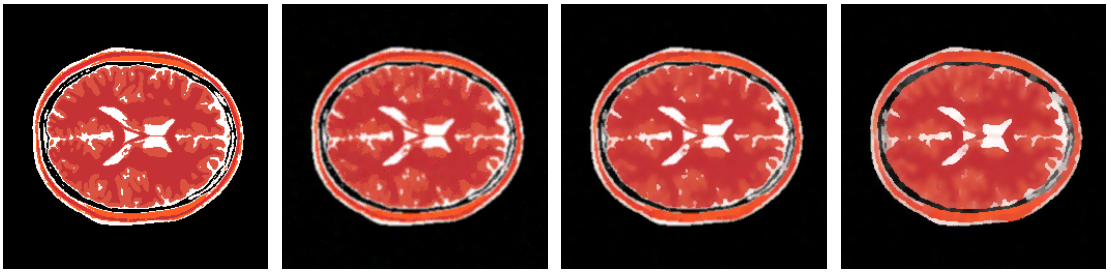

(a) Original MRI

(b) $PSNR = 26.10$ $h_s = 4, h_r = 20$

(c) $PSNR^* = 26.19$ $h_s = 4, h_r = 40$

(d) $PSNR = 25.49$ $h_s = 4, h_r = 80$

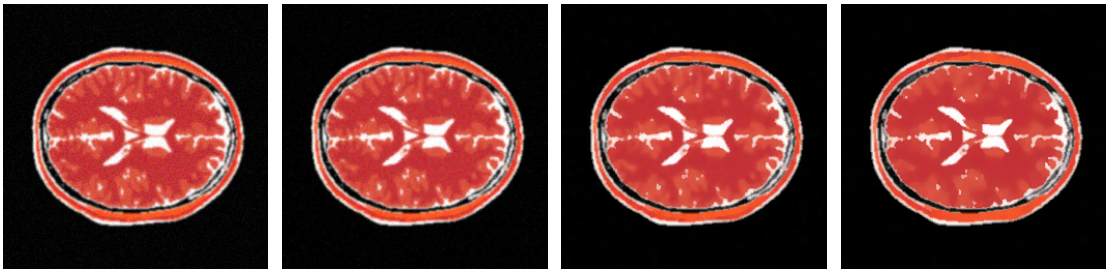

(e) Corrupted MRI PSNR^{ref} =18.73

(f) $PSNR = 26.03$ $h_s = 1, h_r = 40$

(g) $PSNR = 26.18$ $h_s = 3, h_r = 40$

(h) $PSNR = 26.18$ $h_s = 5, h_r = 40$

Figure 5.5: Mean Shift filtering results for corrupted MRI according to different bandwidth parameters. (a) is the original MRI data (e) is corrupted data with $\mathbf{B}[63, 1]$*; The reference PSNR is computed by corrupted image and original image; (b),(c) and (d) are filtered results obtained from the fixed* h_s*=2 but different* h_r *along the range* $[1, 255]$*; the PSNR is computed by filtered image and original image; (c) is the optimal mean shift filtered result with optimal PSNR equal to* 26.19*dB; (f),(g) and (h) are filtered results obtained from the fixed* h_r*=80 but different* h_r *along the range [1,5].*

Additionally, we study the evolution of the *mean shift* filtering results according to various setting of bandwidth parameters. The PSNR evolution against h_s and h_r for *mean shift* filtering results is shown in figure 5.8.

It is observed that PSNR evolution against h_s and h_r for *mean shift* filtering is smooth and no local maximum. That means it is possible to obtain the optimal parameters for **H**.

5.5.2 PI results

In this subsection, we compare the effect of PI method for PI$_{1D}$, PI$_{Diag}$ and PI$_{Full}$ according to various number of samples (100, 1000, 5000), and with the various spatial bandwidth value (1, 2, 3, 4, 5).

Figures 5.9, 5.10, 5.11 and 5.12 show the PI results on natural images. Figures 5.14 presents the PI results on synthesized images.

We compared the optimal PI results with the exhaustive search (ES) results, where the optimal PI results is obtained from n=100 and PI$_{Diag}$.

Compared with PSNR^{ref}, for range bandwidth optimization, both multi-variate PI method is able to improve the PSNR results without using exhaustive search. It is helpful to provide an estimation of range bandwidth matrix and it is efficient for *mean shift* filtering algorithm.

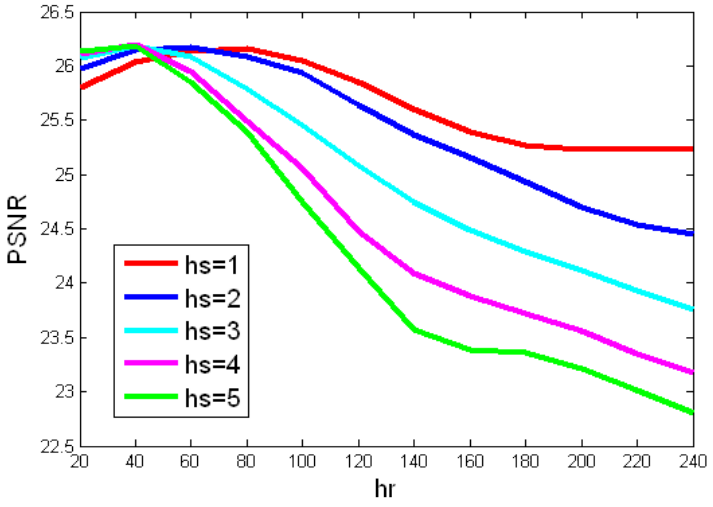

Figure 5.6: PSNR assessment according to h_s and h_r.

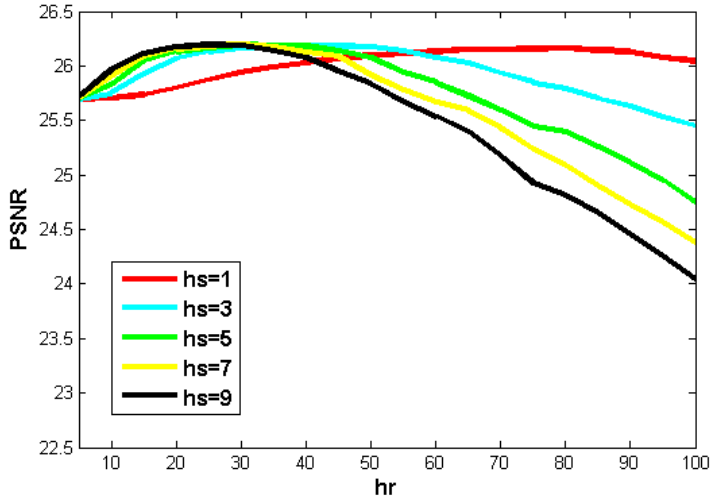

Figure 5.7: Detailed PSNR assessment according to h_s=1 to 10 and h_r=5 to 100.

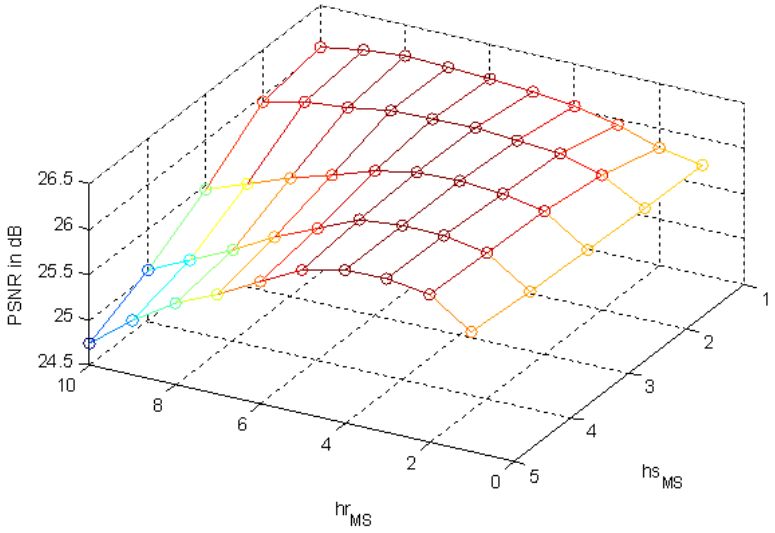

Figure 5.8: PSNR evolution against h_s and h_r

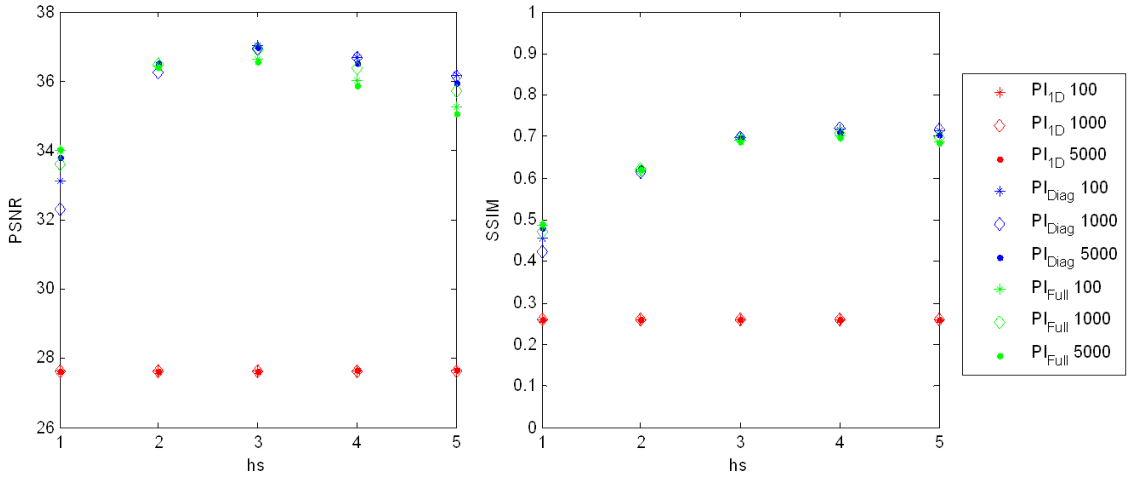

Figure 5.9: PSNR and SSIM calculation by PI methods on Lena.

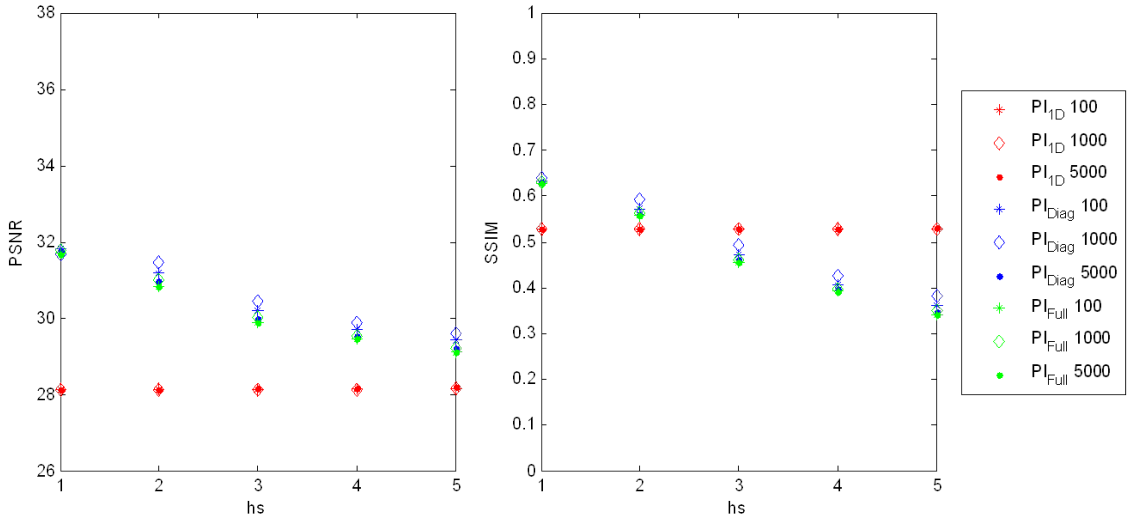

Figure 5.10: PSNR and SSIM calculation by PI methods on Mandrill.

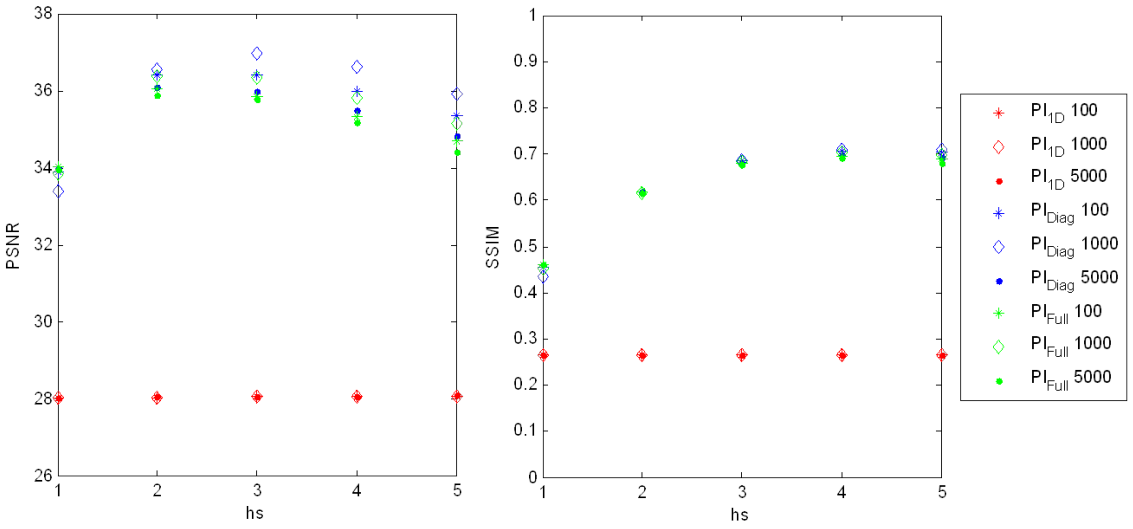

Figure 5.11: PSNR and SSIM calculation by PI methods on Peppers.

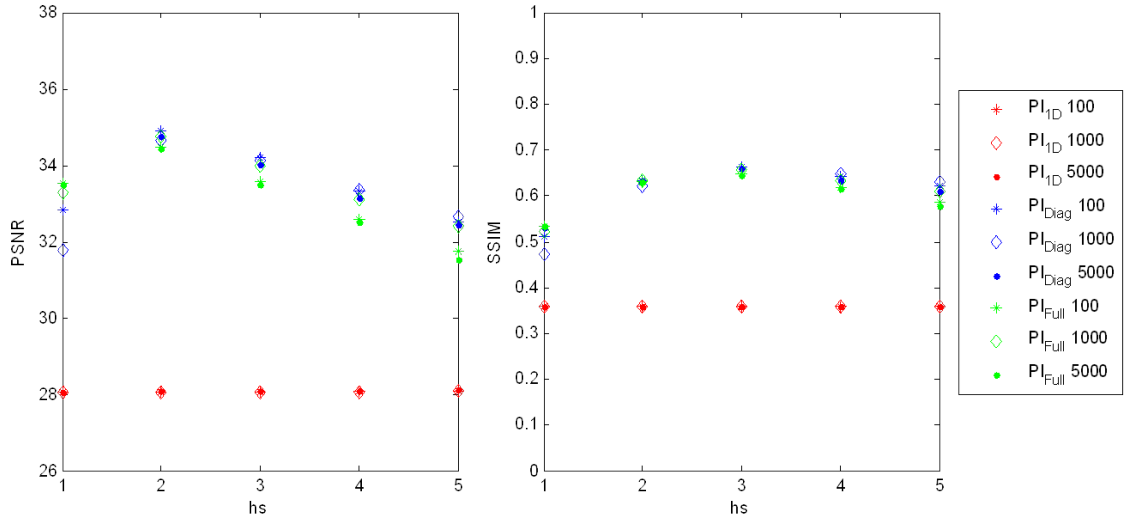

Figure 5.12: PSNR and SSIM calculation by PI methods on Lake.

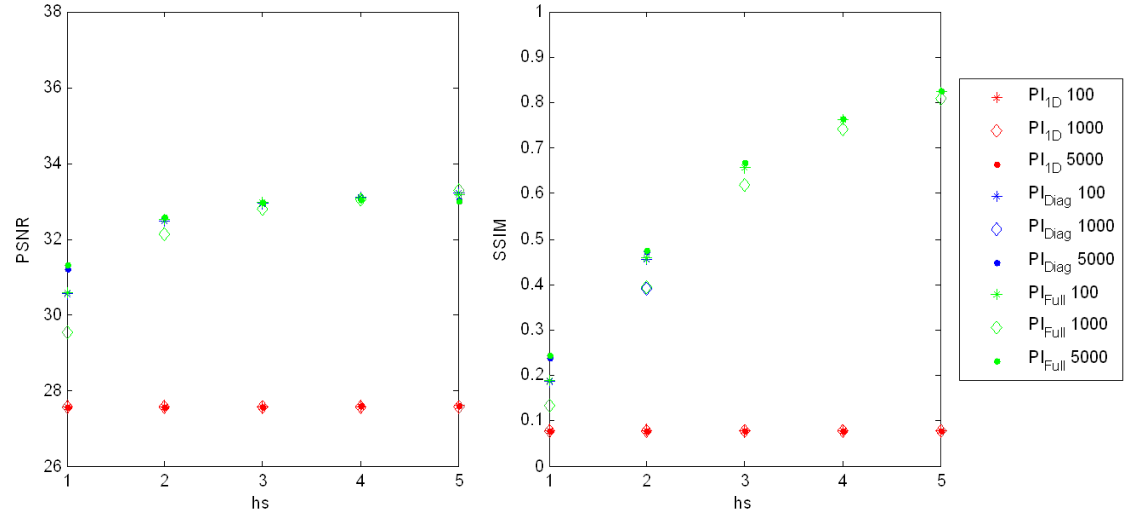

Figure 5.13: PSNR and SSIM calculation by PI methods on Tito.

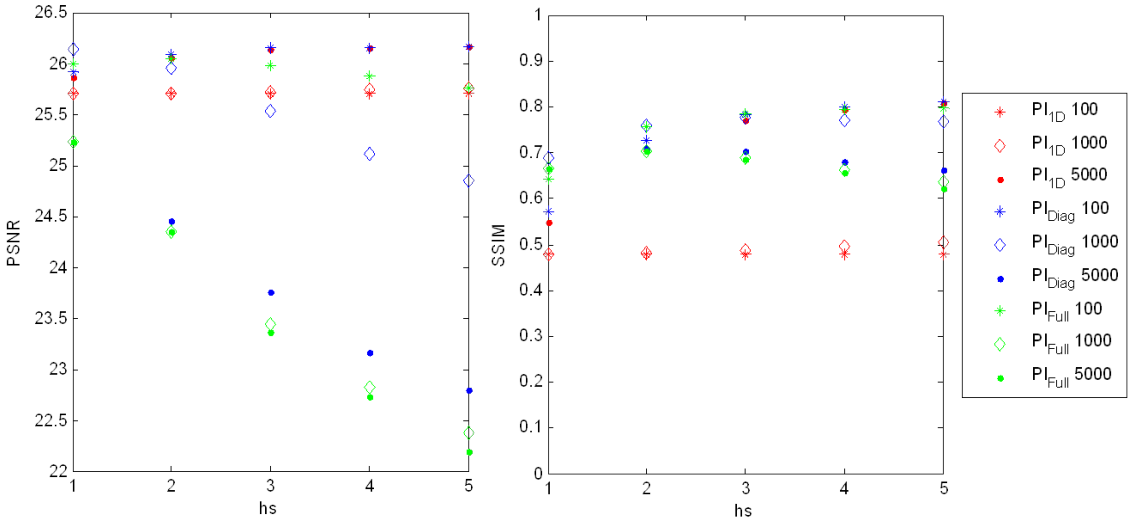

Figure 5.14: PSNR and SSIM calculation by PI methods on MRI ($\sigma = 10$).

Images	PSNR^{ref}	PI_{1D}	PI_{Diag}	PI_{Full}	PSNR^{*}_{ES}
Lena	27.62	27.65	37.03	36.65	37.05
Mandrill	28.13	28.16	31.80	31.70	31.95
Pepper	28.13	28.05	36.41	36.06	36.48
Lake	28.06	28.08	34.89	34.47	34.95
Tito	27.58	27.58	33.21	33.19	33.88
MRI	25.70	25.70	26.18	26.04	26.20

Table 5.1: Comparison of optimal PI results and optimal Exhaustive Search results on PSNR.

From the PSNR and SSIM with h_s evolution according to the various number of samples and various type of range bandwidth matrix PI selectors, we can conclude that:

1. PI rules not only depend on range bandwidth matrix, but also depend on h_s setting. Thus, *mean shift* filtering is very sensible to the selection of h_s. Normally h_s has a range from 1 to 5 for our natural image data set. The bigger h_s is, the more smoother the image is.
2. We tested various number of samples: 100, 1000, 5000, no big difference is observed among different number of samples.
3. PI_{1D} results are far away from real optimal bandwidth parameters. PI_{Diag} is the most common used and can obtain the promising estimated bandwidth parameters. PI_{Full} results are very close to the PI_{Diag}, and not always better than PI_{Diag} (not recommended).

5.6 Conclusion

In this chapter, we aim at optimizing the essential bandwidth matrix parameters of *mean shift* filtering by using PI method. Based on kernel density estimation, univariate PI method for estimating bandwidth matrix during *mean shift* on color noised images fails to improve image quality. Thus, we propose multi-variate PI method on estimating the bandwidth matrix for *mean shift* filtering according to diagonal matrix and full matrix. Experimental results show the efficiency and

the robustness to multi-variate PI method in *mean shift* filtering with diagonal matrix against the choice of number of samples and on the choice of h_s. This choice of h_s have been studied using an exhaustive search optimization. In the next chapter, we introduce a novel segmentation framework based on *mean shift* filtering free of original data knowledge and fine bandwidth matrix tunning.

Chapter 6

From Grid-sample method to Probability-Map method

6.1 Introduction

In this chapter, a new automated segmentation system which combines *mean shift* filtering and *region growing* segmentation based on regular-grid sample is proposed. Such a regular-grid based sample framework requires a reference to optimize the final segmentation results. Also, it takes huge time for conducting all the tuning parameters. Therefore, we propose a *PM* framework in order to tackle the need of reference and improve the time consuming.

This chapter is organized as follows: Section 6.2 describes the regular-grid based framework and analysis its performances on blurred and noised synthesized data. Section 6.3 presents the principle of *PM* framework, gives results of synthesized data, and comments the properties of such approach. We conclude with a brief discussion of these two approaches in section 6.4.

6.2 Grid sample-method for segmentation framework

An overview of the automated segmentation framework is presented in figure 6.2. The synthesized MRI data is employed for testing the robustness of the framework. The golden standard for segmenting white matter of the synthesized MRI is given in figure 6.1.

After some basic pre-processing procedures like registration and normalization of the input data, the main part of processing is focusing on the *mean shift* filtering which is detailed in section 6.2.2 and *region growing* segmentation which will be discussed in section 6.2.3. Two parametric

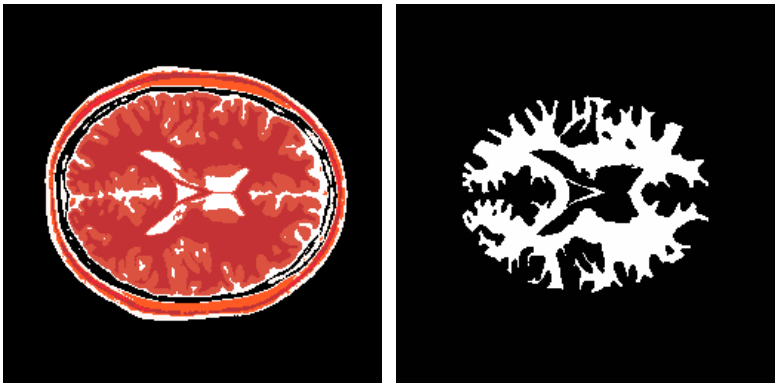

(a) Original MRI (b) White matter

Figure 6.1: Reference white matter segmentation of original labeled MRI image.

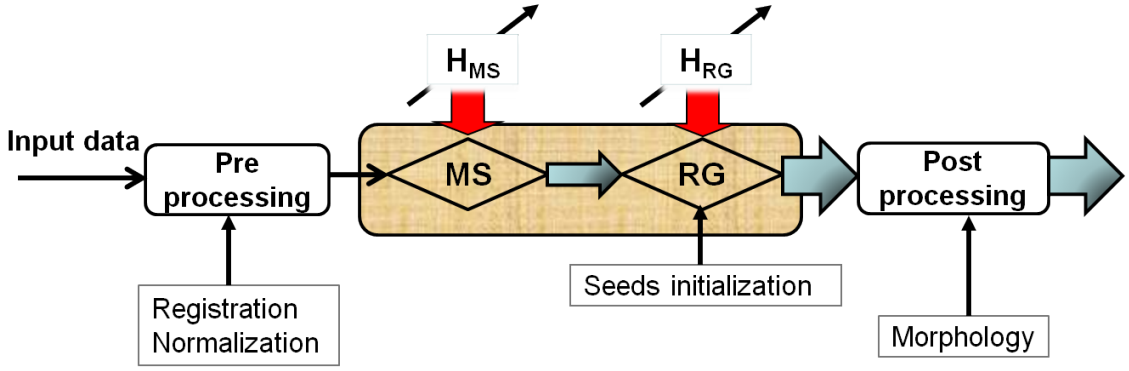

Figure 6.2: Framework of MSRG-based segmentation.

matrices are defined for *mean shift* filtering and *region growing* segmentation: $\mathbf{H}_{MS}$ and $\mathbf{H}_{RG}$.

Morphological based concerning is employed for the post-processing in order to prune the border and fill the holes of segmented results. According to tuning bandwidth parameters($\mathbf{H}_{MS}$,$\mathbf{H}_{RG}$), a series of output binary segmented images are obtained.

6.2.1 Pre-processing

The first step of figure 6.2 is pre-processing which includes registration and normalization. Registration and normalization platform which transform different sets of data into one coordinate system will be built first in order to compare or integrate the data obtained from these different measurements. Normalization is essential to quantify the range of bandwidth for *mean shift* filtering step. In our experiment, we normalized all the intensity value in the range $[0, 255]$.

6.2.2 Mean shift filtering

The *mean shift* filtering procedure is detailed in section 2.6 of chapter 2. The *mean shift* filtering step is necessary since the modes obtained during the filtering represent the local features of images, and will make segmentation much easier. Also, it enables to decrease the intensity

inhomogeneity.

For *mean shift* filtering, spatial information as well as intensity information are applied since synthesizing spatial statistical information with intensity values provides a means for improving the segmentation results. We illustrate the data points $\mathbf{x}$ with joint spatial-range domain $(\mathbf{x}_s, \mathbf{x}_r)$. Each data point becomes associated to a point of convergence which represents the local mode of the density in the feature space. Thanks to the *mean shift* filtering, a series of filtered results are obtained according to the different setting of bandwidth matrix $\mathbf{H}_{MS}$. The similarity measurement is Mahalanobis distance and kernel used is Epanechnikov kernel. For each *mean shift* filtering output, the vector $\mathbf{z}$ is presented for each pixel in the volume space after *mean shift* and as the input for *region growing* step.

As a vector, the bandwidth matrix $\mathbf{H}_{MS}$ consists of two kinds of values: hs_{MS} for the spatial scale and hr_{MS} for the range scales [Grenier 06]. We perform *mean shift* using only diagonal matrices which are extensively used in *mean shift* applications [Comaniciu 03, Hong 07].

6.2.3 Region growing segmentation

The segmentation procedure consists in grouping the close modes that were found with the *mean shift* filtering process, using a similarity criteria, and iteratively searching until the minimal cluster size is obtained. The *region growing* segmentation algorithm [Zucker 76, Grenier 06] starts with a set of points (known as 'seeds'), and regions are extended to adjacent points from these seeds under the condition of those neighboring pixels whose properties are most similar to the seeds. Once the similarity condition is met, the pixel is said to belong to the same region as one or more of its neighbors. The procedure is iteratively performed for each pixel with an initialized bandwidth and is terminated when no more pixel that can be added to the region.

The procedure of *region growing* will be presented as follows. Retrospectively reminding *mean shift* filtering data whose pixel presented as $\mathbf{z} = (\mathbf{z}_s, \mathbf{z}_r)$ as input of *region growing*. Let $\{\mathbf{z}_i\}_{i=1,2...n}$ and $\{\mathbf{p}_i\}_{i=1,2...n}$ the input of *region growing* and the segmented image points in the d-dimensional feature space, the *region growing* segmentation (see figure 6.3) is performed as follows:

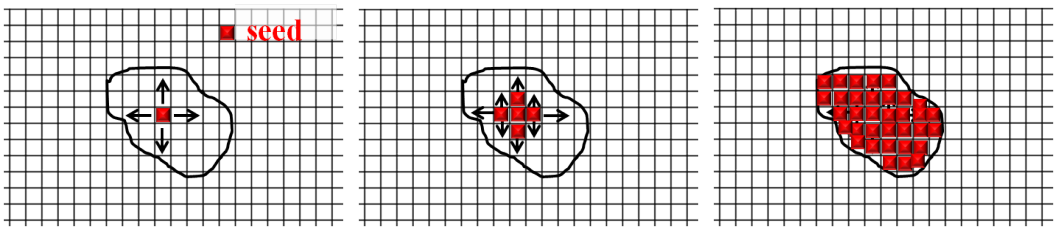

(a) *Step* 1. (b) *Step* 2. (c) *Step* 3.

Figure 6.3: Procedures of RG segmentation.

1. Initialize a set of seeds $\{\mathbf{z}_{seeds}\}_{r=1,2...n_{seeds}}$,
2. Choose a bandwidth matrix $\mathbf{H}_{RG}$. It consists of two kinds of values: hs_{RG} for the spatial scale and hr_{RG} for the range scales,

3. For each seeds $\mathbf{z}_{seeds}$, compute the Mahalanobis distance: $d^2_{\mathbf{H}} = (\mathbf{z}_i - \mathbf{z}_{seeds})^T \mathbf{H}^{-1}_{RG}(\mathbf{z}_i - \mathbf{z}_{seeds})$,
4. The output pixel after *region growing* can be presented as a binary variable $\mathbf{p}_i$, where value 1 represents targeted results which close to seeds and the value 0, which is the inverse situation. If $d^2_{\mathbf{H}} < 1$, assign to $\mathbf{p_i} = 1$, otherwise $\mathbf{p_i} = 0$, for acquiring an binary segmented image,
5. Replaced initial seeds $\{\mathbf{z}_{seeds}\}_{r=1,2...n_{seeds}}$ by this homogeneous regions $\{\mathbf{p}_i\}_{i=1,2...n}$,
6. Repeat the steps 2 to 5 for the new seeds $\{\mathbf{z}_{seeds}\}_{r=1,2...n_{seeds}}$ until no more pixels can be added to the segmented region $\{\mathbf{p}_i\}_{i=1,2...n}$.

The *region growing* is a rapid, robust and tunable parameters segmentation algorithm through a bandwidth parameters $\mathbf{H}_{RG}$. However, it also suffers from different problems of automatically selection of seeds and optimization of bandwidth matrix. The selection of seeds is crucial as it determines what is the feature of interest of the data and what is irrelevant. An obvious way to improve the *region growing* algorithm is to provide more effective pixel labelling technique and to automate the process of seed selection [Fan 05]. In this framework, a manual selection of seeds is employed for the sake of consideration of accuracy and time-consuming.

One can note that the merging step introduced by [Comaniciu 02] is not the same as the one describe here. The major reason is the objective. We need to obtain a binary segmentation. Indeed the locations of the seeds is of high importance as they are defining which features consist of the desired object.

We use the DICE criteria [Dice 45] to quantify segmentation results. Let $\mathbf{X}$ and $\mathbf{Y}$ be two binary images of n pixels. The DICE index is computed as:

$$\mathbf{DICE}(\mathbf{X}, \mathbf{Y}) = \frac{2.|\mathbf{X} \cap \mathbf{Y}|}{|\mathbf{X}| \cup |\mathbf{Y}|} \tag{6.1}$$

where $|\cdot|$ represents the cardinal of a set, *i.e.* it is the number of pixels equal to 'true' for a binary image. A DICE index equal to zero means these two images have no common members, and is equal to one if the images are identical.

The simple example of *region growing* segmentation results based on synthesized MRI data is presented in figure 6.4. The creation of synthesized MRI labeled image is described in chapter 2.3.

Figure 6.4 illustrates the *region growing* segmentation of white matter of labeled MRI image (a). Figure 6.4(b), (c) and (d) are segmented results obtained from the different bandwidth parameters. Perfect segmentation is obtained by figure 6.4(d) with DICE=1. The automatic work flow works ideally on white matter segmentation for the synthesized MRI data since there is no noise and no blurring effect.

6.2.4 Bandwidth optimization of MS and RG

In order to determine the best segmented results from *mean shift* and *region growing*, the adjustment of bandwidth $\mathbf{H}_{MS}$ and $\mathbf{H}_{RG}$ are employed in optimization step. From Figure 6.5,

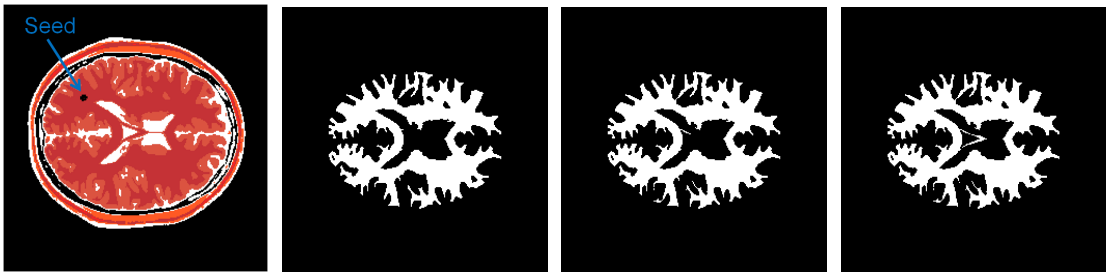

(a) Original MRI

(b) Final segmentation hs_{RG}=1,hr_{RG}=1 DICE=0.9945

(c) Final segmentation hs_{RG}=2,hr_{RG}=4 DICE=0.9966

(d) Final segmentation hs_{RG}=3,hr_{RG}=6 DICE=1

Figure 6.4: White matter segmentation of original labeled MRI image by using only RG.

Parameters	*Range*
hs_{MS}	1 to 5
hr_{MS}	5 to 100
hs_{RG}	1 to 3
hr_{RG}	1 to 10

Table 6.1: Scale parameter ranges for MS and RG for CGNG.

for each data set, an exhaustive parameter exploration was conducted, and the optimal parameters were supposed to be given by the sets of parameters (tuned up by $\mathbf{H}_{MS}$ and $\mathbf{H}_{RG}$) for which the DICE coefficient is respectively highest.

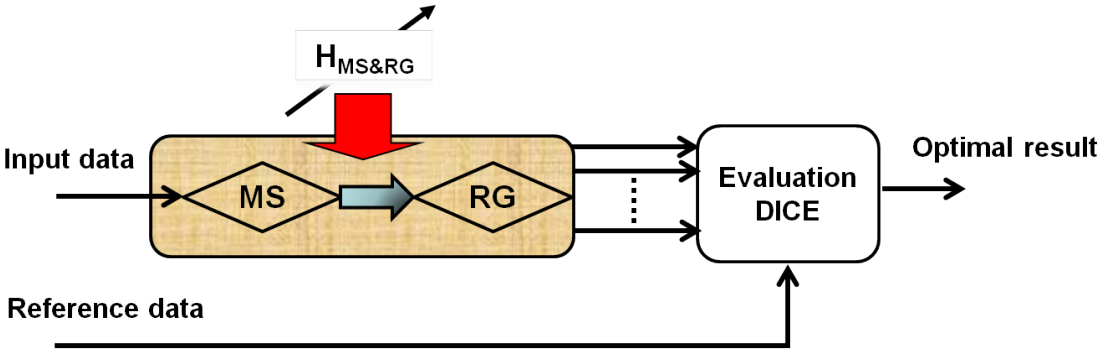

Figure 6.5: Bandwidth optimization of MS and RG with DICE.

In this thesis, we define a vector $\mathbf{h_b}$= [hs_{MS},hr_{MS},hs_{RG},hr_{RG}] which means a group of bandwidth parameters. Based on previous research on synthesized MRI image in figure 5.5, we limit the range of the each parameter as follows:

In figure 6.4, hs_{MS} varies from 1 to 5 using an interval of 0.5 and hr_{MS} varies from 20 to 100 using an interval of 20 based on the previous research in figure 5.5. hs_{RG} varies from 1 to 3 using an interval of 1 and hr_{RG} varies from 2 to 10 using an interval of 2. Regarding the way of selecting bandwidth, we nominate this framework "Cartesian-Grid based method". Additionally, we nominate such kind of number generator "Cartesian-Grid number generator" (CGNG).

6.2.5 Post-processing

Morphological mathematics is used for post-processing of the segmented results. One time dilating then one time erosion are applied for the binary segmented results with a 'disk' as structural element in order to fill broken areas. Experimentally, radius of 2 for structure element is a fixed parameter for whole results, the optimization performance could also be done for the better results.

6.2.6 Result of Cartesian-Grid based framework

In the following, the synthesized blurred $\mathbf{B}[63, 1]$ and noised $\mathbf{N}(\sigma_N = 10)$ MRI data is employed during this experiment to verify the robustness of the proposed automatic segmentation Cartesian-Grid based framework. According to adjustment of bandwidth (the same with figure 6.4), we select 750 groups of bandwidth parameters and obtain 750 segmented results by using Cartesian-Grid based framework.

Figure 6.6 shows two single segmented results obtained with two groups of parameters selection by using CGNG framework.

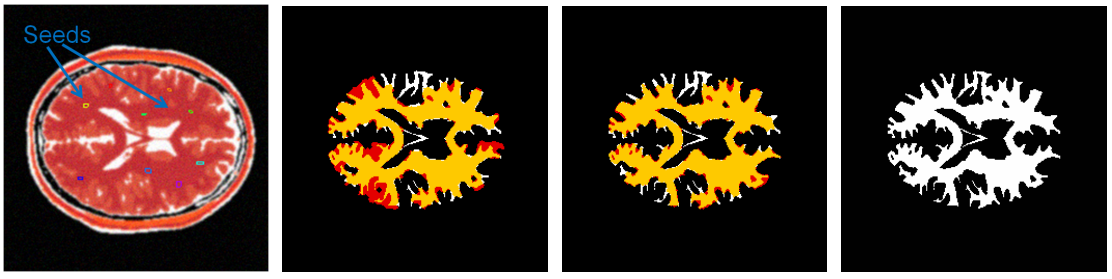

(a) Corrupted MRI PSNR=18.73.

(b) Final segmentation hs_{MS}=3,hr_{MS}=40 hs_{RG}=1,hr_{RG}=4 DICE=0.85.

(c) Final segmentation hs_{MS}=5,hr_{MS}=20 hs_{RG}=1,hr_{RG}=6 DICE*=0.91.

(d) White Matter.

Figure 6.6: White matter segmentation of corrupted MRI image by using MS and RG.

Figure 6.6(a) is original corrupted data. (b) and (c) are two segmented results obtained from various bandwidth parameters. The color is employed to better illustrate the over-segmentation and under-segmentation. The yellow part shows the intersection part of our segmented result and true reference, the white part presents the reference white matter, and the red part means over-segmentation. (c) is the optimal segmented result obtained by (hs_{MS},hr_{MS},hs_{RG},hr_{RG})=(5,20,1,6), the optimal DICE is equal to 0.91. (d) is the true reference white matter segmentation. Although corrupted by blurring and noise, the segmentation framework still acquired promising segmented result compared to reference segmentation.

6.2.7 Properties of Cartesian-Grid based framework

In this subsections, we discuss the limitations of Cartesian-Grid based framework:

1. Reference needed

It is emphasized that reference is employed for optimizing the bandwidth $\mathbf{H}_{MS}$ and $\mathbf{H}_{RG}$ after Cartesian-Grid based framework. It is more like a learning step to determine the optimal segmented result. In fact, the reference is not offered in the real case, such as medical infarct segmentation. Therefore, we have to face a problem: when there is no reference value, how could we find a segmentation result of the optimal solution?

2. Time consuming

   The results of *mean shift* filtering and *region growing* segmentation highly depend on various selection of bandwidth parameters. The CGNG-method is able to acquire promising filtering results based on synthesized corrupted MRI data whereas it is necessary to decide in advance what the interval should be, and all the grid points need to be used. Here, 750 jobs are performed for acquiring better segmentation result with DICE=0.91. The execution time of one job mostly depends on the parameter hs_{MS} and the average approximate time is 10 minutes for each group of parameters. Thus, the overall estimated time is 125 hours. These kind computing is too heavy for usual computing resources. Ordinary computing environment is not able to support so heavy computation. Parallel computation which lie on Cluster and EGEE Grid are employed in order to improve the computing efficiency.

To conclude, regarding the drawbacks of Grid-sample based framework as well as randomicity of *mean shift* and *region growing* parameters, we propose a new method which is based on probability map (PM).

6.3 Probability map method

6.3.1 Framework of *PM* method

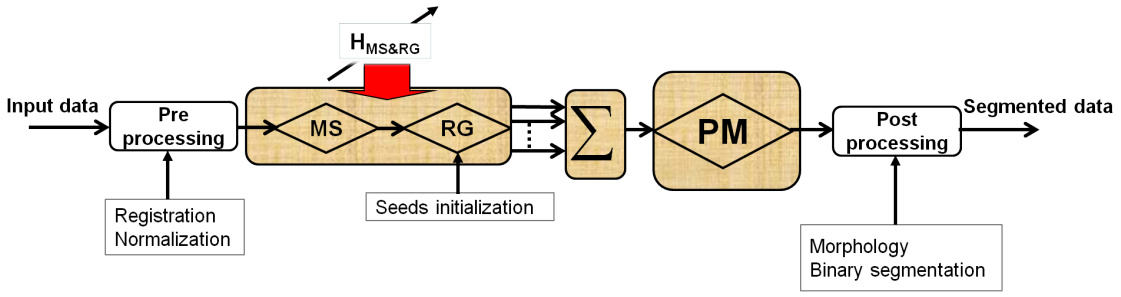

Figure 6.7: Framework of probability map

The probability map method is proposed here in order to give a probability compared with initialized seeds. By using simple threshold, the segmentation result would be easy obtained. At the same time, validation will be used to compute the optimal segmentation results by using golden standard reference with each output results after morphological procedure.

The *PM* method is fully based on probabilistic theory. By analogy with the idea of Monte Carlo, we assume that the PM is capable to provide probabilistic information of the final binary segmentation by using a set of adjustment of bandwidth. In other word, instead of knowing the

best solution, one can obtain a probability map which presents different possibility compared with the properties of the seeds. The PM-method can be viewed hypothetically as a problem of integral evaluation. Since Monte Carlo simulation is defined as to use random points for the numerical evaluation of a system [Kalos 08]. In section 6.3.2, we discuss the principle of PM and random sample generators in section 6.3.3. Also, we demonstrate the feasibility and verify this hypothesis of using PM in section 6.3.4.

6.3.2 Principle of probability map method

The integral of Lebesgue integrable function $f(x)$ can be expressed as the average or *expectation* of the function f evaluated at a random location. Consider an integral on the one-dimensional unit interval

$$I[f] = \int_0^1 f(x)dx = \overline{f} \tag{6.2}$$

Let x be a random variable that is uniformly distributed on the unit interval. Then

$$I[f] = E[f(x)] \tag{6.3}$$

For an integral on the unit cube $I^d = [0,1]^d$ in d dimensions,

$$I[f] = E[f(x)] = \int_{I^d} f(x)dx \tag{6.4}$$

in which $\mathbf{x}$ is a uniformly distributed vector in the unit cube.

The probability map is based on the probabilistic interpretation of an integral. Consider a sequence $\mathbf{p_i}$ sampled from the uniform distribution. In our application, if the output maps after global framework are presented as $\mathbf{p_i}$, where $i = 1, 2, ...N$ is the series of output according various bandwidth parameters of MS and RG extracting from $\mathbf{h_b}$ as input. Then an empirical approximation to the expectation is:

$$PM_N[f] = \frac{1}{N}\sum_{i=1}^{N} f(\mathbf{p_i}) \tag{6.5}$$

According to the strong Law of Large Number [Feller 68], this approximation is convergent with probability one, that is:

$$\lim_{N\to\infty} PM_N[f] \to I[f] \tag{6.6}$$

The PM, in fact calculates the average of the function at a set of randomly sampled points. This means that each point adds linearly to the accumulated sum that will become the integral.

In addition, it is unbiased, which means that the average of $I_N[f]$ is exactly $I[f]$ for all N, that is,

$$E[PM_N[f]] = PM[f] \tag{6.7}$$

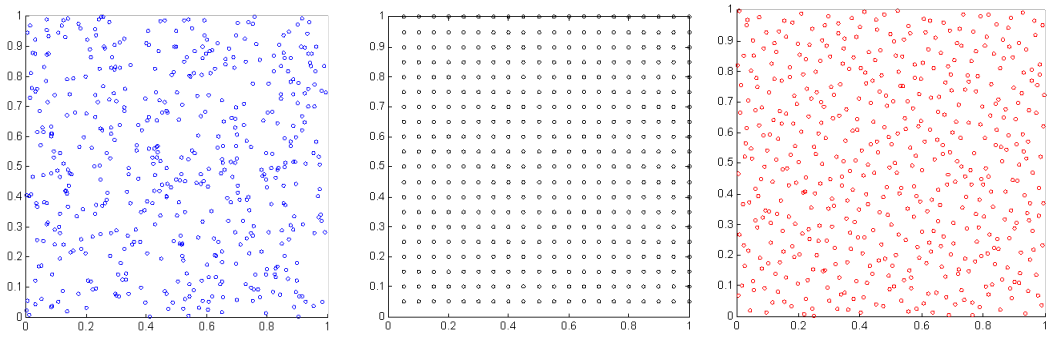

(a) $Pseudo-random$ (b) $Cartesian-grid$ (c) $Quasi-random$

Figure 6.8: Illustration of the three studied random number generators.

in which the average is over the choice of the $\mathbf{p}_i$. In other words, probability map is that how many times each pixel has been segmented. The value of probability map is between $[0, 1]$ with interpretations that the higher the value is, the more probable the underlying pixel to be in the final segmented region is.

6.3.3 Random Number Generators

It is crucial to decide in advance how many points to choose and how fine it is should be for the PM. Here, we discuss three types of random generators: Pseudo-Random Number Generator (PRNG) which is normal random sample generator method, Cartesian-Grid Number Generator (CGNG), which is the regular grid-based sample method and Quasi-Random Number Generator (QRNG) which is invented by Kuipers and Niederreiter for testing in the uniformity properties of numerical sequence [Kuipers 74, Niederreiter 92, Hua 81].

1. Pseudo-Random Number Generator(PRNG):

   Pseudo-random number is not a fake random numbers, where the "pseudo" has a regular means. It means that computer-generated pseudo-random numbers is not only random but also regular. How to understand it? PRNG complies with certain rules sometimes, but sometimes does not comply with any rules. Such as "There is no two leaves exactly the same shape", which is characteristic of things point to that random, but each leaves of trees have similar shape, which is of things in common, that regularity. From this perspective, you probably would accept the fact that: the computer can only generate pseudo-random number which can not produce absolute random number.

   Pseudo-random number (see figure6.8(a)) is generated by the determined algorithm and its distribution function could pass the relevant statistical tests. Different from random number, they are generated by the algorithm, rather than a true random process. In general, the PRNG methods are mainly the following three kinds [Diaz 10]:

   – Direct Method: which is based on the physical meaning of the distribution function generated. The shortcoming is that only applicable on some of the special distributions, such as the binomial distribution, Poisson distribution.

- Inversion Method: assuming U subject to $[0, 1]$ on an uniform distribution, so that $\mathbf{X} = F^{-1}(U)$, then X is the cumulative distribution function of F. This method is simple, easy programming, and wide applicability.
- Acceptance-Rejection Method: suppose you want to generate random numbers which PDF is $f(x)$, then firstly find a PDF of the random number generator $g(x)$ and a constant c, so that $f(x) \leq cg(x)$, then the receiver refused algorithm. As the average computing algorithm c times to get a want to generate random numbers, so the value of c must be as small as possible. Obviously, the shortcoming of this algorithm is the difficulties in determine values g and c.

The convergence rate of *PM* with PRNG method decreases with the increase of number of samples N at the rate of $O(N^{-1/2})$, since an additional factor of 4 increase in computational effort only offers an additional factor of 2 improvement in accuracy. The slow convergence rate result in the improvement of accuracy become very difficult. Also, the "clumping" phenomenon occurs in the figure 6.8(a) since the points are totally independent. This could become a limiting factor in accuracy of PM-based method, for the reason of the points could not cover all the region.

2. Cartesian-Grid Number Generator(CGNG):

   We can also sample points which depend on a Cartesian-grid which means we sample each grid point exactly once then the *PM* method effectively becomes a deterministic quadrature scheme, whose fractional error decreases at the rate of $O(N^{-1})$ or faster. CGNG (figure6.8(b)) fully satisfied the requirements of uniformity. However, the trouble with the CGNG approach is that it is necessary to decide in advance what the interval it should be, and all the grid points need to be used. It is therefore not possible to sample until some convergence criterion has been met.

3. Quasi-Random Number Generator(QRNG):

   The flaw of PRNG and CGNG is rooted in contradictions of "random" and "homogeneity". Therefore, the generator does not require a virtual reality of the new uniform, but strive to make samples of any size (especially in small samples) meet the low diversity. In other words, the cost of the expense of randomness, will be in exchange for improved uniformity. The Quasi-Random Number Generator (QRNG) [Kuipers 74, Niederreiter 92, Hua 81] could bridge the gap between the flexibility of random PRNG and the advantages of uniformed CGNG. The advantage of the uniformed QRNG is that the resulting samples tend to be more evenly distributed. The convergence rate get a better improvement which is $O((logN)^c N^{-1})$ (c is constant). Because of the correlations, the QRNG (see figure 6.8(c)) is mess versatile than PRNG.

   There are three kinds of quasi-random sequences which can be used to aid uniform distribution of random numbers generated, respectively, Halton sequence, Sobol sequence, Latin hypercube sequence. Here, the Halton sequence [Train 00] is employed for QRNG to obtain the low discrepancy samples.

   The Halton sequence is constructed according to a deterministic method that uses a prime

number as its base. As an example, let's take two dimensional case of the Halton sequence in space [0,1] based on 2 and 3. To generate the sequence S_a for 2, we start by dividing the interval $[0, 1]$ in half, then in fourths, eighths, etc, which generates:

$$S_a = 1/2, 1/4, 3/4, 1/8, 3/8, 5/8, 7/8, 1/16, 3/16, 5/16, \ldots \tag{6.8}$$

and to generate the sequence S_b for 3, we divide the interval $[0, 1]$ in thirds, then ninths, twenty-sevenths, etc, which generates:

$$S_b = 1/3, 2/3, 1/9, 2/9, 4/9, 5/9, 7/9, 8/9, 1/27, 2/27, \ldots \tag{6.9}$$

Then, we pair them up and get the sequence $\mathbf{S_c}$ of points in a unit square:

$$\mathbf{S_c} = (1/2, 1/3), (1/4, 2/3), (3/4, 1/9), (1/8, 2/9), \ldots \tag{6.10}$$

The linear correlation problem would appear between sequences generated from higher primes. In order to avoid such problems, various other methods such as, scramble, leak and skip have been proposed [Kuipers 74, Hua 81]. We obtain the $\mathbf{S_d}$, two dimensional Halton sequence after scramble, leak and skip processing:

$$\mathbf{S_d} = (1/4, 2/3), (1/8, 2/9), (1/2, 1/3), (3/8, 4/9) \ldots \tag{6.11}$$

6.3.4 Experiments and results

In this subsection, we present *PM* results for segmentation of white matter of labeled MRI image and corrupted MRI image. Also, we discussed the properties of *PM* based on three different random generators: CGNG, PRNG and QRNG.

– *PM* representation

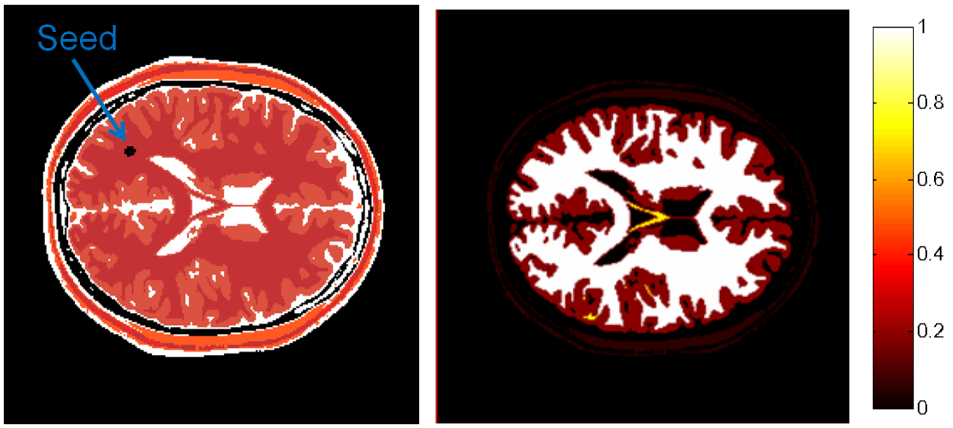

(a) Original MRI (b) Probability map

Figure 6.9: Probability map of white matter segmentation for original labeled MRI image by using only RG.

Figure 6.9 presents the *PM* for segmentation of white matter of labeled MRI image. Figure 6.9(a) is original MRI data and (b) is the *PM* based on CGNG with bandwidth parameters hs_{RG} varies from 1 to 5 using an interval of 2 and hr_{RG} varies from 10 to 50 using an interval of 10. The *PM* is obtained by using grid-based samples which has the probability meaning that the high value is, the high probability of the final segmented region is.

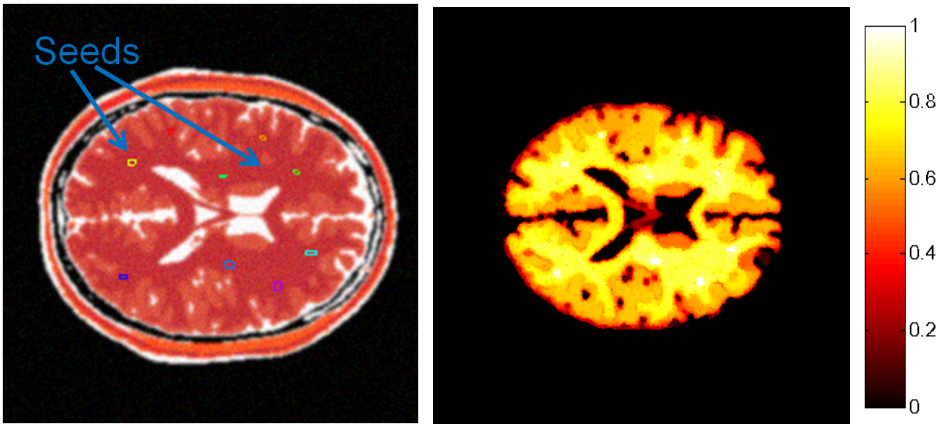

(a) Corrupted MRI $PSNR$=18.73 (b) Probability map

Figure 6.10: Probability map of white matter segmentation of corrupted MRI image by using MS and RG.

Another experiment is on the corrupted MRI data. Figure6.10(a) it the input data, (b) is the probability map based on CGNG with bandwidth parameters hs_{MS} varies from 1 to 5 using an interval of 2 and hs_{MS} varies from 40 to 120 using an interval of 40, hs_{RG} varies from 1 to 3 using an interval of 1 and hr_{RG} varies from 2 to 10 using an interval of 2.
The proposed segmentation system obtained promising segmentation results according to the DICE quantification. However, the values of interval for four parameters separately are difficult to choose. We implement the followed experiments based on CGNG, PRNG and QRNG by taking into account the precision of segmentation result as well as time-consuming. Also, the further tests will be not on original synthesized MRI data, but on the corrupted MRI synthesized since it is more close to the realistic model.

– comparison of *PM* based on CGNG, PRNG and QRNG
A set of 100, 500,750 groups of random samples are generated based on PRNG and QRNG in this work. The range of hs_{MS} and hr_{MS} for *mean shift* filtering as well as hs_{RG} and hr_{RG} for *region growing* segmentation is fixed in the table 6.2. Also, the CGNG is employed with hs_{MS} varies from 1 to 5 using an interval of 0.5 and hr_{MS} varies from 20 to 100 using an interval of 20; hs_{RG} varies from 1 to 3 using an interval of 1 and hr_{RG} varies from 2 to 10 using an interval of 2. 750 groups of grid-sample are employed here to perform the *PM*. For CGNG, we only employ 750 groups of random samples but not 100 and 500 since it is difficult to select the interval for each parameters.
Figure 6.11 illustrate the comparison of three random generators: (a) PRNG, (b) CGNG and (c) QRNG. In order to acquire a binary image of the whiter matter region, the threshold is employed for obtaining the final segmentation according the DICE coefficient. (d), (e) and

Parameters	*Range*
hs_{MS}	1 to 5
hr_{MS}	5 to 100
hs_{RG}	1, $\sqrt{2}$, 2, $\sqrt{3}$, 3
hr_{RG}	1 to 10

Table 6.2: Scale parameter ranges for MS and RG.

(f) are the optimal DICE separately obtained by different type of random generators. As follows we discuss the properties of them by taking into account the precision and time-consuming.

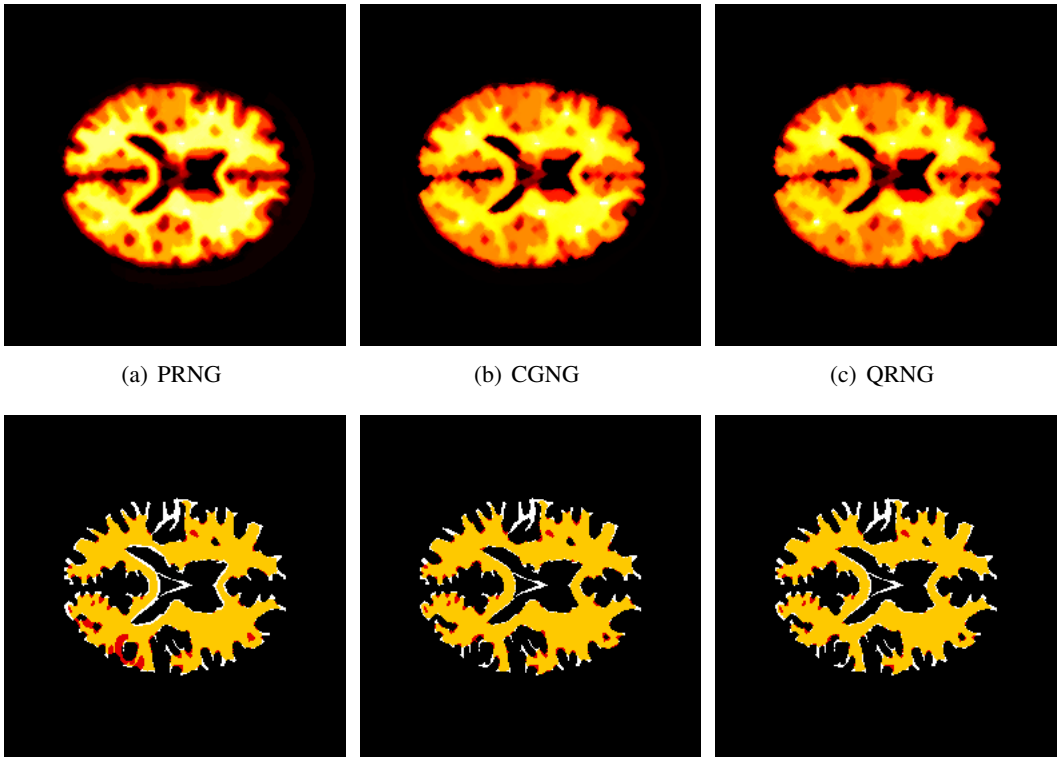

(a) PRNG (b) CGNG (c) QRNG

(d) DICE=0.87 (e) DICE=0.92 (f) DICE=0.91

Figure 6.11: Probability map of different random generators.

For best segmentation, the CGNG got the best result with DICE=0.92 which is better than QRNG with DICE=0.91 and PRNG with DICE=0.87.

– Time-consuming of *PM*

We compare the time-consuming based on these three kinds of number generators in the table 6.3.

The mean time t_{MSRG} of *mean shift* and *region growing* for each group of random samples is computed based on these three number generators. For each group of parameter, it shows that PRNG takes more time than QRNG. For CGNG, we calculate the average time for 750 group of bandwidth parameters, but it is noticed that the time would have a big variance since the numerous possibility of intervals.

	$nb_{\mathbf{h}_b}$	$\bar{t}_{MSRG}(min)$	DICE*
PRNG	100	4.38	0.8646 ± 0.0094
	500	4.12	0.8707 ± 0.0027
	750	3.6	0.8721 ± 0.0008
CGNG	750	10	0.92
QRNG	100	4.29	0.9097 ± 0.0083
	500	3.79	0.9135 ± 0.0020
	750	3.52	0.9137 ± 0.0003

Table 6.3: Time-consuming for different type of random generators.

However, regarding DICE quantification, the CGNG is better than QRNG and PRNG. We conclude that QRNG is the best in achieving a balance on precision of DICE and time-consuming.

– Convergence of *PM*

In order to understand the relationship between *PM* estimation and the number of samples, bootstrap method [Efron 79] is employed. The procedures are as follows:

1. 1000 groups of samples are generated separately based on PRNG and QRNG, *mean shift* and *region growing* are performed to obtain 1000 binary segmented results;
2. randomly pick 10 binary segmentation from the 1000 segmented results to construct a *PM*, then compute the optimal DICE with the reference;
3. repeatedly 30 times of step 2 to obtain the mean and stand deviation of these 30 optimal DICE;
4. randomly pick numbers from 10 to 500 step by 10, repeat step 2 and step 3.

Figure 6.12 presents the convergence of *PM* estimation based on PRNG and QRNG by using bootstrap re-sampling method. It can be seen that the PRNG gives the worse performance compared with QRNG. Starting from 150 samples, the optimal DICE curve of QRNG tend to a constant 0.91 and the optimal DICE curve of PRNG tend to constant 0.87. As the number of samples increases, the standard deviation gradually decrease.

6.4 Conclusion

In this section, we summarize the contributions as follows:

1. We proposed a automatic segmentation system which combine *mean shift* filtering and *region growing* segmentation. The synthesized data is applied to verify the robustness of proposed segmentation framework and understand the rules of bandwidth's selection. The automatic work flow works ideally on white matter segmentation for the synthesized MRI data and obtains promising segmented results on the blurred and noised synthesized data.
2. We have proposed a new *PM*-based automatic segmentation framework without using reference for optimizing the final result according to different groups of bandwidth parameters. The proposed *PM*-based method also employ the QRNG which has an intrinsic capability

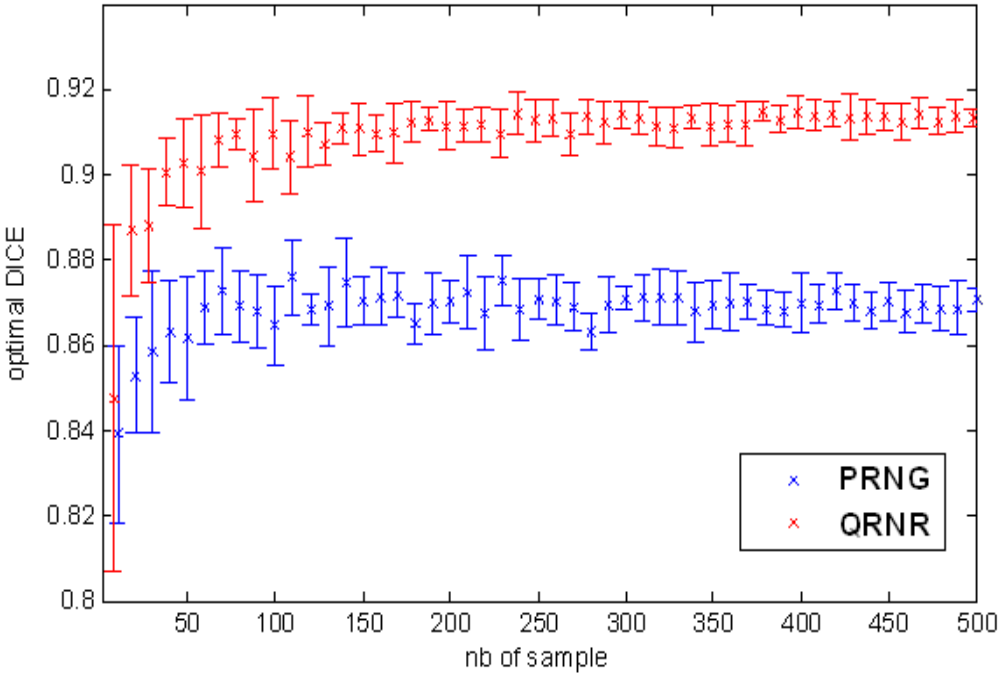

Figure 6.12: Optimal DICE obtained with various random sample numbers

of obtaining more uniformed random samples. The QRNG reduces the computation time compared with PRNG and provides the high possibilities of the final segmentation results compared with PRNG.

3. The generalization of PM-based method could be extended to any other framework, like level set....only if it satisfying some assumptions:
   – Optimal bandwidth $\mathbf{H}_{MS}$ and $\mathbf{H}_{RG}$ matrices producing perfect segmented result exist,
   – Small modifications of optimal $\mathbf{H}$ also get pretty good results,
   – The seeds have the same characteristics with the targeted segmented region.

   The *PM* is able to give a probabilistic information of the final segmentation results. However, there are several problem still needed to be taken into account during probability maps calculation: 1) 'Enough' samples (here are the number of bandwidth parameters) need to be considered. 2) The bandwidth parameters should be randomly selected following uniformed law. 3) The value of the *PM* at a point indicates the similar feature of this point with those of seeds used for the *region growing*.

Chapter 7

Conclusion of Methodological Contribution

In part II, we study the properties which could influence *mean shift* filtering and discuss the mechanism by which they occur. Moreover, for the purpose of segmentation and clustering, we propose an automated framework which combines *mean shift* filtering and *region growing* segmentation and probability map (PM) optimization. We enumerate the conclusions as follows:

1. By summarizing optimal *mean shift* filtered results on various noise and blurring corrupted data, we conclude *mean shift* filtering is robust and efficient on noise effect but not so feasible on recovering blurring effect based on PSNR and SSIM measurements.
2. Univariate PI method for estimating bandwidth matrix during *mean shift* on color noised images fails to improve image quality. Experimental results show the efficiency of multivariate PI method by using diagonal matrix on estimating the bandwidth matrix for *mean shift* filtering.
3. We propose a new PM-based automatic segmentation framework without using reference for optimizing the final result according to different groups of bandwidth parameters. The proposed PM-based method employs the quasi-random number generator (QRNG) which has an intrinsic capability of obtaining more uniformed random samples. The QRNG reduces the computation time compared with the Cartesian-grid number generator (CGNG) and provides the highest possibilities of the final segmentation results compared with the pseudo-random number generator (PRNG).

III APPLICATION to MEDICAL ISCHEMIC DATA

Résumé

L'accident vasculaire cérébral de type ischémique est une maladie grave qui nécessite une prise en charge très rapide pour limiter ses conséquences à moyen terme. Un des traitements consiste, par des moyens chimiques ou mécaniques, à désobstruer le vaisseau responsable de l'accident pour assurer la re-perfusion des tissus cérébraux. Dans ce contexte, une identification et une prédiction des tissus à risque d'infarctus serait une aide précieuse à la décision clinique. Elle peut se baser sur une imagerie IRM multimodale.

La troisième partie de ce manuscrit est dédiée à la mise en oeuvre de notre schéma *mean shift* sur des données d'imagerie IRM multimodale de l'accident vasculaire ischémique.

Le chapitre 9 précise le contexte médical, les objectifs et les challenges cliniques. Ce chapitre présente également les données IRM multimodales qui sont utilisées. Il s'agit d'images de diffusion (DWI), de cartes paramétriques associées (ADC) et d'images de perfusion (PWI) avec des cartes paramétriques caractérisant localement la perfusion tissulaire (CBF, CBV, TTP, MTT, Tmax). L'objectif visé est d'arriver, à partir des données acquises lors de l'accueil du patient, à prédire la zone finale de l'infarctus ischémique et eventuellement identifier la zone réversible. Un corrolaire est d'identifier les données initiales les plus pertinentes pour cette prédiction.

Après un état de l'art des approches existantes, le chapitre 10 détaille la chaîne de traitement d'images proposée qui inclut des prétraitements et post-traitements spécifiques aux données considérées en plus de notre schéma de segmentation basé sur du filtrage *mean shift*, de la croissance de région et une carte de probabilité. Les critères quantitatifs d'évaluation sont explicités : il s'agit du critère DICE, des mesures de sensibilité et de spécificité et de courbes ROC.

Le chapitre 11 présente les données qui seront utilisées pour tester notre approche. Il s'agit de données IRM multimodales 3D de rat ainsi que des données humaines.

Le chapitre 12 expose et commente les résultats obtenus sur les deux jeux de données. Pour les données rats, le schéma proposé permet une bonne estimation de la zone lesion finale. En comparant notre prédiction avec une segmentation manuelle faite par un expert sur les données

obtenuesà J+3, J+4, ou J+12, nous obtenons une valeur de DICE de $0,8$. Ces résultats sont obtenus à partir des données ADC et Peak. La prise en compte des données TTP dégrade le résultat. Avec une valeur de DICE de $0,57$, les résultats préliminaires obtenus sur les données humaines sont moins bons que pour les rats. Ces résultats restent intéressants et sont obtenus à partir des données (TTP, MTT, CBF). L'ajout des données (ADC and DWI) n'augment pas sensiblement la qualité des résultats. La valeur de DICE est une valeur moyenne calculée en 3D et elle n'est pas homogène selon les coupes. Ces résultats, moins bons que pour les rats, peuvent s'expliquer par le fait que, contrairement au rat où on travaille sur un modèle d'accident cérébral provoqué artificiellement, il y a pour l'homme de nombreux facteurs qui ne sont pas connus et qui peuvent compliquer la prédiction. En particulier, pour les patients avec une ischémie cérébrale conduisant à une hypo-perfusion de la région oligemia, la re-perfusion de cette région peut naturellement se faire par d'autres vaisseaux.

Le chapitre 13 propose plusieurs perspectives de travail. Tout d'abord, seul un jeu limité de données a pu être traité. Il sera donc nécessaire de poursuivre les expériences sur des jeux de données plus étendus pour valider l'efficacité et la robustesse de l'approche carte de probabilité proposée. Sur ces jeux de données étendus, il sera également intéressant de comparer notre approche avec des méthodes de classification avec apprentissage.

Chapter 8

Introduction of medical application part

An acute ischemic stroke is a complicated life-threatening disease with possible long term disability. Fast treatment is to deobstruct the vessel as soon as possible by using chemical or mechanical ways to ensure recanalization of the artery and reperfusion of the cerebral tissue. Therefore, the early identification and prediction of tissue at risk of infarction after acute stroke would be helpful in clinical decision making to maximize benefit and minimize side effects of therapeutic interventions.

This part is dedicated to the application of our *mean shift*-based framework to stroke imaging.

In the chapter 9, we start from the medical background of ischemia to introduce its common causes, diagnosis methods and therapy protocols. Then, based on this ischemic context, we illustrate the medical objectives and challenges.

In the chapter 10, we introduce our global framework which integrate the pre-processing, *mean shift* filtering, *region growing* segmentation, *PM*, and post-processing. At last, we expose the segmentation criteria we use.

In the chapter 11, different data we consider are presented. Both rat and human data will be processed to quantify the ischemia.

In the chapter 12, by using the proposed segmentation framework, we show the results obtained and discuss them separately for rat and human.

In the chapter 13, we make the summary of conclusions and we discuss the properties and limitations of our approach to process such data.

Chapter 9

Medical Context and Objectives

9.1 Introduction

In this chapter, we firstly introduce the definition of cerebral ischemia as well as its diagnosis methods and therapy protocols in section 9.2. Imaging plays an important role in ischemic diagnosis and the basics of MRI acquisition is presented in section 9.3. The multi-modality MRI acquisitions are presented in section 9.4 and section 9.5. Then, based on this ischemic context, we illustrate the medical objectives that is to quantify the final ischemic infarct and to verify which parameters of medical imaging can be considered as good predictors.

9.2 What is Stroke?

9.2.1 Definition and causes of stroke

A stroke is the loss of brain function that is caused by a disturbance in the blood supply to the brain [Gonzalez 11]. It is a medical emergency that can cause permanent neurological damage (also called infarct) and death.

There are two classifications of a stroke: ischemic stroke and hemorrhagic stroke. Although they are both caused by the lack of blood supply to the brain, they have different causes. More than eighty percent of strokes are considered ischemic strokes (See Figure 9.1 from copyrighted images) and are usually caused by thrombosis, embolism, systematic hypoperfusion, or venous thrombosis. The other twenty percent is constituted by hemorrhagic stroke which may be caused by a hematoma or bleeding inside or outside of the brain.

In summary, ischemic strokes are caused by a blockage of blood vessels while hemorrhagic

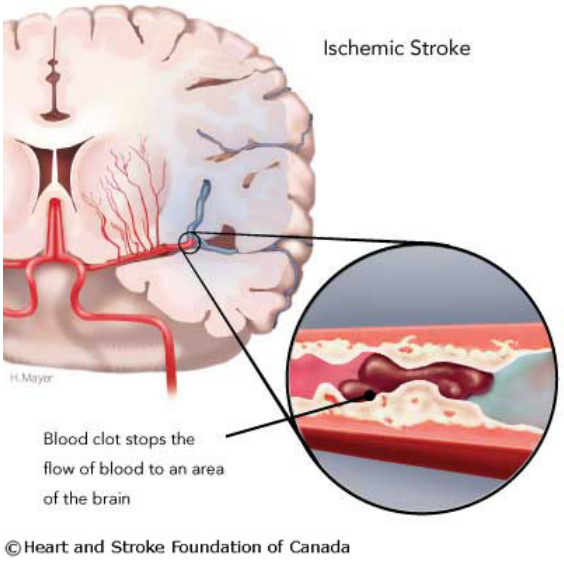

Figure 9.1: Stroke ischemia.

stroke is caused by bleeding. Both of them have almost the same symptoms but sometimes ischemic strokes can be more gradual while hemorrhagic strokes happen suddenly and can be located inside the area of ischemia.

9.2.2 Diagnosis methods

Stroke is a highly time-dependent condition. The survival, extent of damage and recovery depend on time before reperfusion. Reperfusion therapy is approved within the first 4.5 hours after the occurrence of ischemia [Murphy 06].

Imaging plays a central role in estimation and diagnosis of the patients with ischemia [Fisher 03, Hjort 05]. Medical Imaging (CT, MRI) can be useful before and after the occurrence of a stroke. It can also provide doctors with information they need to select the appropriate therapy for treatment after a stroke. The MRI basics and multi-modalities imaging will be illustrated in the next section.

9.2.3 Therapy protocols

Treatment of ischemic stroke is done by thrombolysis which involves the use of thrombolytic agents such as tPA (tissue Plasminogen Activator). Thrombolysis, the action of de-obstructing the vessel through chemical or mechanical procedures [Albers 99], is the one and only treatment available, and must be performed in a very short delay (4.5h after stroke onset) as the infarct evolves very fast. Figure 9.2 illustrates the dynamic evolution of brain ischemia.

The increasing red part (infarction) represents the lesion which is also called 'necrotic tissue' along time. The light blue part region (penumbra) is the 'tissue at risk', that will be damaged if the artery remains permanently obstructed, or salvaged if re-perfusion occurs. The dark blue region (oligema) is a part of brain which is actually hypoperfused but can be naturally re-perfused through other vessels.

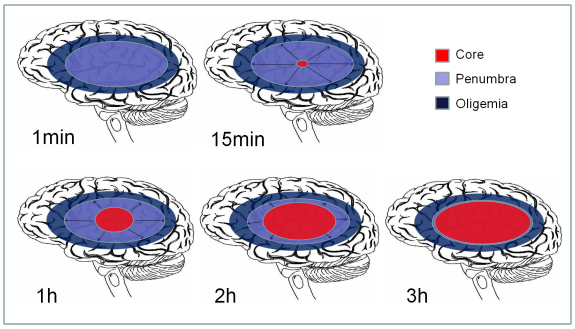

Figure 9.2: Dynamic evolution of brain ischemia.

Using ordinary CT scans which are quick and easy to perform, doctors can identify early (<6h) signs of stroke as well as the type of stroke (hemorrhagic) [Ashok 06]. However, the CT maps looks normal during the first 3-6 hours of an ischemic stroke [Zafar 08].

Normal anatomical MRI is powerless for estimation infarct and tissue at risk while DWI is able to identify ischemic irreversible infarct core (red part) in the acute stroke in the very first minutes [Fisher 03, Hjort 05]. Moreover, PWI and its derivation parameters such as peak or TTP enable the identification and characterization of perfusion deficits both inside and surrounding the infarct core (light blue part). The automatically segmentation of tissue at risk would be meaningful for quantification of final infarct for the further therapy.

9.2.4 Summary of definitions

- *Infarction*: Infarction is the formation of an infarct. An infarct is a region of localized necrosis (or death of living cells) due to obstruction of blood supply. In simple words, an infarct is a region of dead tissues or a region of irreversible damage to cells.
- *Perfusion*: The word "perfusion" is derived from the French verb "perfuser" which means to pour through. It can simple be regarded as the act of pumping a liquid *e.g.* blood, into an organ or tissue (feeding or supplying an organ or tissue with blood).
- *Cerebral Perfusion*: The process by which the brain is kept supplied with oxygenated blood.
- *Reperfusion*: Restoration of blood flow to an area that had previously experienced deficient blood flow.
- *Hypoperfusion*: A medical term for decreased blood flow through an organ.
- *Penumbra*: The portion of the ischemic territory that is still potentially salvageable, if an appropriate treatment is given.
- *Oligema*: The part of brain which is actually hypo-perfused but can be naturally re-perfused through other vessels.
- *Thrombolysis*: Thrombolysis is destructing blood clots by the use of drugs (thrombolytic drugs).

9.3 Basics of MRI

If the human body is placed in a strong constant magnetic field $B0$ and subjected to a second radiomagnetic field (RF), nuclei of hydrogen one in the body absorb RF energy and later completely release or emit the stored energy in a process known as relaxation. The relaxation time is governed by two time constants known as T1 and T2 time constants. The distribution or concentration of excitable nuclei is not the same in each tissue and body part, thus, the amount or intensity of emitted signals will vary. It is this variation of emitted signal that is utilized in building a MRI image.

The human body is predominantly water which is good for MRI because hydrogen protons are excitable by RF pulses when placed in a magnetic field. The following is a list of some common MRI imaging modalities [Sen 11]:

- T1-weighted imaging (T1-WI) in which cerebrospinal fluid (CSF) has a low signal intensity in relation to brain tissue.
- T2-weighted imaging (T2-WI) in which CSF has a high signal intensity in relation to brain tissue.
- Proton density weighted imaging in which CSF has a density similar to brain tissue.
- $T2^*$ imaging which has the highest sensitivity in detecting early hemorrhagic changes.
- Diffusion-weighted imaging (DWI) in which the images reflect microscopic random motion of water molecules.
- Perfusion-weighted imaging (PWI) in which hemodynamically weighted MR sequences are based on passage of MR contrast agent through brain tissue.
- Fluid-attenuated inversion-recovery (FLAIR) sequence, and its variations, null the signal from CSF and produce very heavy T2 weighting as a consequence of very long repetition (TR) and echo (TE) times.

9.4 Diffusion-Weighted Imaging

In order to understand Diffusion-Weighted Imaging, it is necessary to introduce Brownian movement defined as water molecules move or diffuse in a random manner. However, in the brain as in other tissues, the movement of the water molecules cannot be said to be exactly random due to the presence of different obstacles within the tissues, such as cell membranes, fibers etc. For this reason, the micro-movements (or Brownian movement) of the water molecules is referred to as "Apparent diffusion".

Due to the microscopic random motion of the protons of water molecule, diffusion-weighted imaging (DWI) maps is created. The energy failure in neurons and astrocytes results in cytotoxic edema (cell swelling) during ischemia. The cell swelling restrict the diffusion of extracellular water which results in rapid drop of apparent diffusion coefficient (ADC).

Figure 9.3 shows MRI in acute stroke. (a) is Diffusion-weighted MRI in acute ischemic stroke performed one hour after symptom onset and (b) is ADC map obtained from the same patient (named Index177 in our database) at the same time. The red contour is the core of the infarct

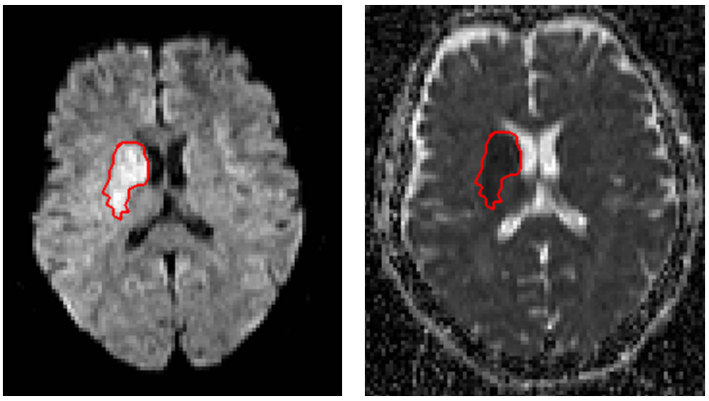

(a) DWI. (b) ADC.

Figure 9.3: DWI(a) and ADC parameters(b) showing core of infarct in acute stroke (Hour 0).

manually delineated by expert.

9.5 Perfusion-Weighted Imaging

As the name suggests, perfusion-weighted imaging (PWI) provides hemodynamic status information (perfusion status) of the brain. The PWI by dynamic susceptibility contrast is acquired by utilizing very rapid imaging to capture the first pass of intravenously bolus of contrast agent.

9.5.1 Bolus-contrast tracking

A bolus is the term used to refer to the contrast agent, instantaneous delivering of the tracers into the blood stream. Tracers can either be:

Endogenous tracing the hydrogen nuclei of water molecules circulating in the blood.

Exogenous the use of an external contrast agent. The most commonly used exogenous tracer in MRI is chelate of Gadolinium. Gadolinium has the desirable properties of being:

1. Paramagnetic: It will only become magnetized only when placed in an external magnetic field and it losses all its magnetism if the external field is removed (paramagnetism = contrast in MRI).
2. Highly-diffusible: It is only present in the vascular space and it will not cross the normal blood-brain barrier. In the case of endogenous tracing, the tracer (hydrogen contained in water) is diffusible since it crosses the blood brain barrier and is exchanged between intra and extravascular compartments.

9.5.2 First pass technique

The first pass technique exploits the magnetic susceptibility of Gadolinium chelate. Magnetic susceptibility is the degree of magnetization of a material in response to an applied magnetic field.

We mentioned previously that an MRI scan involves the use of a $B0$ field which should be constant and homogeneous. When injected into the body during an MRI scan, Gadolinium becomes highly magnetized. This magnetization introduces local inhomogeneities in the $B0$ field in the region where Gadolinium is present. This heterogeneity caused by the presence of the magnetized gadolinium results in a decrease of the $T1$, $T2$ and $T2^*$ relaxation times of the surrounding tissue and consequently, a drop in the received MRI signal. The drop in signal during the first pass of the agent in the vessels of the tissue enables the extraction of perfusion parameters after post-processing.

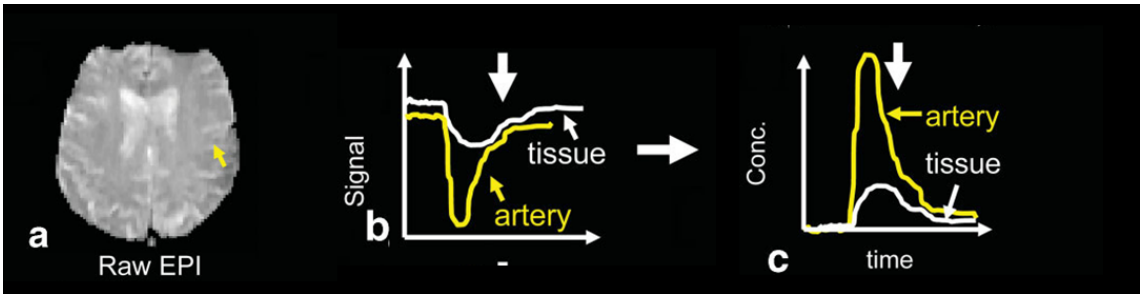

Figure 9.4: Time course of a typical enhanced dynamic susceptibility contrast (DSC) imaging experiment.

After a contrast agent is injected while the raw Echo Planar Imaging (EPI) are acquired in figure 9.4 (a), the contrast agent reaches the brain, causing a substantial signal drop in the tissue and arteries (figure 9.4 (b)), while in turn is converted into contrast agent concentration (figure 9.4 (c)) [Ostergaard 05].

Perfusion-weighted Imaging (PWI) can provide perfusion information on both core infarct region and surrounding regions while DWI provides information on the infarct region. The mismatch between the PWI image and the DWI image can be used to identify the region that can be saved by reperfusion.

The penumbra can be detected by mismatch of PWI and DWI [Fisher 03, Hjort 05]. However, the PWI frequently overestimates the tissue at risk, while parts of acute DWI lesion may reserve, especially after re-perfusion. There are different opinions regarding the predictive role of PWI on the growth of infarction. The most common one indicates that not all tissues in the mismatch area have the same risk of damage [Mezzapesa 06]. However, it is still meaningful to access this salvageable tissue by using mismatch region between the abnormalities delineated on the initial diffusion and perfusion maps acquired in the acute stage of ischemia.

In order to predict the evolution of the infarct, we will mainly focus on images obtained using DWI and PWI imaging techniques. These imaging techniques are deeper presented below. After few days, the infarct can be observed using a T2-weighted imaging. This late acquisition is employed as final estimation of the final infarct. Consequently, it will be used for validation.

9.5.3 Converting time-concentration curves into Perfusion parameter maps

When a bolus is injected, it takes finite time to arrive at the main arteries supplying the brain. When perfusion parameters are measured relatively to the time of injection, we talk of absolute

values. However, finite time also expires before the bolus flows from the arteries to the tissue. When perfusion parameters are measured relatively to the time of arrival at a main artery, it is referred to as relative values. We will consider numerical integration and deconvolution method to evaluate PWI parameters.

1. **Numerical Integration**

   In order to create a measure of blood volume, the easiest way is to measure the area under the time concentration curve (see figure 9.4 (c)) using a simple numerical integration, see the equation 9.1:

   $$rCBV = \int C_{tissue}(t)dt \tag{9.1}$$

   Integration of area under time concentration curve provides an index that is proportional to the relative cerebral blood volume (rCBV) of a given pixel. It should be addressed that this does not provide an absolute value of CBV, but yields an image that may be useful for comparing normal to ischemic or diseased tissue [Filippi 05].

2. **Deconvolution**

   The quantitative values of the CBV, CBF and MTT can be viewed as being embedded into the time-concentration curve. The extraction processes of perfusion parameters are usually described as the deconvolution of the time-concentration curve with the AIF.

   Arterial Input Function (AIF) [Conturo 05] is simply the concentration of contrast agent in the arteries as a function of time. When an artery (e.g. middle central artery) runs through imaged slices of the cortex, the AIF can be obtained non-invasively from the arterial pixels, see the figure 9.5.

   Indicator-dilution theory of perfusion imaging for non-diffusible tracers states that the time concentration profile $C_{Gd}(t)$ is equal to the cerebral blood flow multiply by the convolution of the arterial input function (AIF) and the tissue residue function noted as $R(t)$.

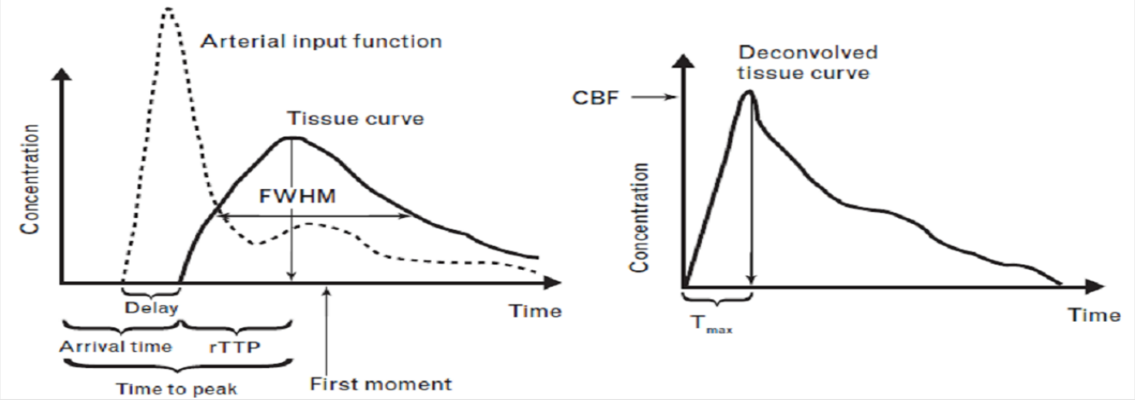

Figure 9.5: Time concentration tracer curve turned into a measure of perfusion.

Using $R(t)$, we measure the fraction of tracer present in the vasculature at time t after injection of contrast agent. $C_{Gd}(t)$ is given by:

$$C_{Gd}(t) = CBF. \int_{u=0}^{t} AIF(u).R(t-u)du \tag{9.2}$$

Deconvolution uses an iterative process to create an estimate of the $R(t)$ if one is given the AIF and the time concentration curve in the tissue of interest [Ostergaard 05, Swanson 05]. Then, a quantitative estimate of the CBF can be determined by:

$$CBF = C_{Gd}(t). \left[\int_{u=0}^{t} AIF(u).R(t-u)du \right]^{-1} \tag{9.3}$$

A quantitative estimate of the Cerebral Blood Volume can be obtained using equation 9.4:

$$CBV = k \int C_{Gd}(t)dt \left[\int AIF(t)dt \right]^{-1} \tag{9.4}$$

with k a scaling factor depending on the hematocrit and the vessel geometry.
Using the central Volume Principle, the Mean Transit Time (MTT) is calculated by

$$MTT = CBV/CBF \tag{9.5}$$

Thus, based on the raw images and AIF, maps of CBV, CBF, MTT are computed. The others parameters such as Peak, TTP and Tmax extracted from these maps are shown in figure 9.5.

9.5.4 Perfusion Parameters

Quantitative assessment of fluid motion is dependent on flow, time and volume. Thus, perfusion imaging is concerned with determining flow parameters related to time/duration of flow, and to volume of blood displaced. Post-processing of the resulting image yields parametric image maps. Some of the important parameter maps are:

Cerebral Blood Volume (CBV) : the blood volume of the cerebral capillaries and venules per cerebral tissue volume.

Cerebral Blood Flow (CBF) : Cerebral blood flow is a measure of the blood volume delivered to a defined unit mass of tissue per unit time.

Mean Transit Time (MTT) : This is a measure of the average time it takes for a tracer to travel through a given region of the brain. The transit time is dependent on the distance travelled between arterial inflow and venous outflow and is related to CBV and CBF according to the Central Volume Principle [Ostergaard 05], which states that: $MTT = CBV/CBF$.

Time to Peak (TTP) : This refers to the time it takes for the contrast agent to reach its peak concentration in the tissue. It is inversely proportional to CBF. If CBF reduces, TTP increases because the contrast agent will take a longer time to reach its peak concentration.

Time of Arrival (TA) : This refers to the time it takes for the contrast agent to arrive at the tissue after injection.

Tmax : Time to reach the max of $R(t)$.

9.6 Objective and strategy

We focus on two majors objectives: 1) Automatically predict the final ischemic infarct. 2) Evaluate the best predictor based on various multi-modality MRI maps.

9.6.1 Automatic estimation of final infarct

It is admitted that stroke is a heterogeneous disorder, and the duration of the penumbra in humans varies substantially from person to person depending on a variety of factors, including location of the vessel occlusion, degree of collateral blood flow supply, intrinsic susceptibility to ischemia of hypo-perfused tissues, and other patient-specific factors [Kidwell 04].

The traditional direct visualization of location and extent of the infarct could greatly improve our ability to decide which patients may benefit from therapy and which patients need specialized determination according their individualization. However, the shortcomings are obvious that it cost so many time on objective visualization directly on so enormous MRI data sets since for ischemic patients, time is life.

Thresholding [Wu 01, Shen 03, Sobesky 05, Takasawa 08, Prakash 08, Olivot 09, Wu 12] is an old and universally applied segmentation technique which is comparatively easy to implement. The problem with thresholding is to choose the right threshold. This is because threshold values vary across images and across different slices in an image; the quality of the process also depends on the separation between the classes.

There are various automatic models, such as Generalized Linear algorithm, Multi-parametric ISODATA technique, Markov Random Field model with Expectation Maximum algorithm, Adaptive Mean Shift with high density clustering algorithm, have been developed for ischemic infarct segmentation [Wu 01, Jacobs 01, Zhang 01, Arnaldo 09]. All of these approaches have demonstrated good overall accuracy. However, they are limited in their generalizations since they have been based largely on relative time after onset. Also, the inter-individual variation in timing of scan acquisition, blood pressure, collateral flow and other metabolic conditions can affect largely the precision. In this medical application, our *PM* framework will be considered in order to improve automatically estimation of ischemic infarct.

9.6.2 Optimal predictor of multiple MRI parameters

Simple mismatches between perfusion defect and ADC lesion has been postulated to be a potential aid to therapeutic decision-making, thereby realizing retrieval of tissue [Baron 05]. However, these mismatches frequently underestimate the amount of salvageable tissue or overestimate the amount of tissue at risk of infarction. It is more likely due to the heterogeneity of tissue response to ischemic stroke and to therapeutic intervention [Lo 05].

Many studies aimed at validating the predictive role of PWI on the infarct expansion [Kidwell 04, Ostergaard 05, Zafar 08]. However, it is still an issue debated that if PWI parameters has the ability to predict tissue at risk. The most common [Kidwell 04] of which asserts that not all tissues in the mismatch area have the same risk of damage.

Combining both diffusion as well as perfusion imaging parameters could help to differentiate between ischemic core and penumbra [Ashok 06].

Therefore, in our study, different combinations of multiple MRI parameters are compared to analysis which combination is the most relevant to identify tissue at risk.

9.7 Conclusion

In this chapter, we introduce the medical context of ischemia as well as its diagnosis and therapy methods. Also, we present the principles of acquisition of multi-modalities MRI maps. The challenging objective of this medical application is to automatically estimate the final infarct based on the combination of various multi-modality MRI maps. In the following chapter, we summarize the recent research efforts focused on infarct segmentation methods and we propose a new automatic estimation framework based on *PM*.

Chapter 10

Global Framework

10.1 Introduction

In this chapter, the state of art of method in brain ischemic segmentation is discussed in section 10.2. Then we propose a new automatic segmentation volume-based framework which combines *mean shift* filtering and *region growing* segmentation as well as *PM* optimization in section 10.3. Each element of this framework was detailed in the chapter 6. Thus in this chapter, we only illustrate some specific parameters setting for each part of the framework. Also, the validation criteria for segmentation is presented in section 10.4 for final evaluation of segmentation result.

10.2 State of art on ischemic segmentation

In recent years, there are various semi-automatic or automatic models for performing the segmentation in image processing community. But the most popular methods applied in the literature to ischemic penumbra segmentation based on multi-modality MRI imaging maps are thresholding [Wu 01, Shen 03, Sobesky 05, Takasawa 08, Prakash 08, Olivot 09], region growing [Rosso 09, Contin 10] and feature space analysis [Jacobs 01, Li 04, Baumgartner 05].

Thresholding is an conventional applied segmentation method which is comparatively easy to implement. Based on 5 patients, Takasawa determined the penumbra normalized thresholds in second for PWI-derived MTT>6, TTP>4.8, Tmax >5.5 against validated probabilistic Positron Emission Tomography (PET) thresholds [Takasawa 08]. Olivot et al statistically summarizes that severely hypoperfused regions (defined by Tmax>8s) had low ADC values and were unlikely to reverse after recanalization based on 32 patients [Olivot 09]. Although thresholding methods are easy to compute and not time consuming, it should come as no surprise therefore that there are no

universally accepted thresholds for different multi-modality maps (*e.g.* ADC, DWI, CBF, MTT).

Region growing segmentation is considered as a preferred method compared to thresholding, especially in case where the boundaries of object of interest are not clearly defined. In [Contin 10], the *region growing* approach was implemented as a semi-automatic segmentation algorithm based on Local Statistics algorithm (LS) which obtains a regional mean and standard deviation extracted from a sample delineated by the user on the ROI. However, LS-based segmentation algorithm processes only perfusion computed tomography (PCT) and can not take into account other multi-modal MRI.

A feature space is an n-dimensional abstract space in which each pattern sample is represented by a single point. The dimension of the feature space depends on the number of features used to represent the pattern. The example of feature space is well explained in section 2.3 of chapter 2.

Some of the feature space analysis methods that have been employed in brain segmentation are K-means clustering [Baumgartner 05], multiscale statistical classification [Li 04], *mean shift* clustering [Arnaldo 09], Multi-parametric ISODATA technique [Jacobs 01] and General Linear Model (GLM) [Wu 01].

In this thesis, a compromised semi-automatic segmentation method which takes into account not only time saving auto-segmentation but also human adjustment should be proposed. Moreover, in order to compare and confirm the efficiency of these approaches, they should be formalized and their robustness should be studied deeply using larger number of samples. In the following section, we introduce framework of our proposed segmentation algorithm.

10.3 Proposed global framework

In this section, according to analysis of obtained DWI and PWI parameters, we present the global image processing framework in figure 10.1.

The pre-processing step includes extraction of brain, registration, noise removing, normalization and interpolation. According to two ways of bandwidth parameters selection, we divide the framework into two parts: CGNG and QRNG.

For the CGNG part, the regular-grid method is employed for bandwidth selection of *mean shift* filtering and *region growing* segmentation. A series of binary images are obtained. After post-processing, the final segmentation result is the result that give the best DICE with the reference data.

Different from CGNG, the quasi-random method (QRNG) is employed for bandwidth selection of *mean shift* filtering and *region growing* segmentation. A series of binary images are obtained and aimed to create a *PM*. The *PM* provides a probabilistic information of the final segmentation.

Following *PM*, the post-processing steps are optional. They can consist of morphological mathematics and a binary segmentation depending on the result of *PM* result.

In the following paragraph, we detail each step of the framework.

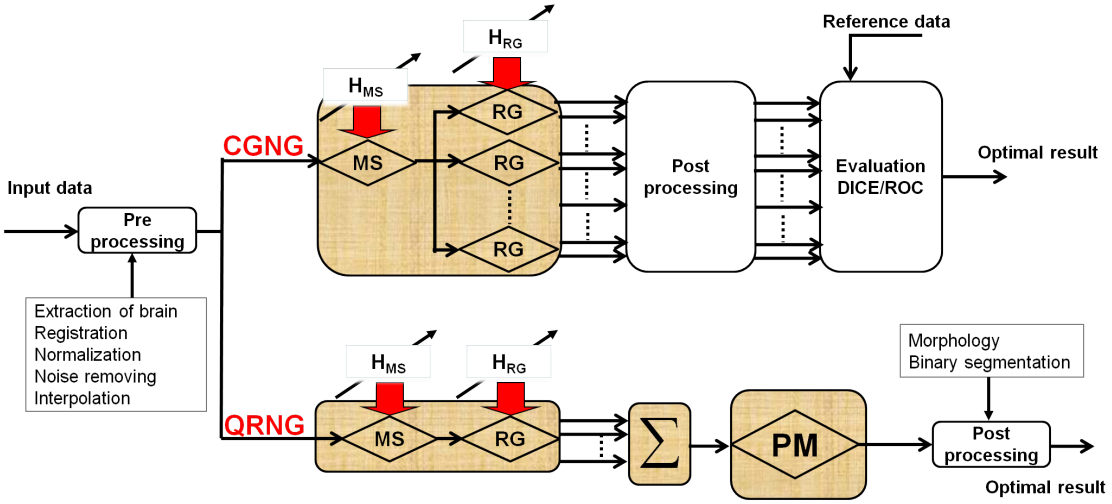

Figure 10.1: Global work flow for predicting the infarct.

10.3.1 Input data in feature space

The input vector $\mathbf{x}$ in the feature space, which combines spatial and range information, is defined as (see the equation 10.1):

$$\mathbf{x} = \begin{bmatrix} \mathbf{x}_s \\ \mathbf{x}_r \end{bmatrix} = \begin{bmatrix} x_x \\ x_y \\ x_z \\ x_{ADC} \\ \vdots \\ x_{MTT} \\ x_{CBV} \end{bmatrix} \tag{10.1}$$

The number of range parameters is selected from 2 to 5 to test the different combinations of multi-parametric MRI maps.

10.3.2 Pre-processing

- Extraction of Brain. Image background usually contains superfluous information which complicates the image analysis and prolongs the processing time. It is beneficial to extract the useful brain information by removing the background before any analysis. In addition, for brain ischemia infarct segmentation, skull, eyes, scalp and other tissues which are intra-cranial are not significant. In our study, the extraction of brain was preceded manually by an expert by segmentation of Region of Interest (ROI) to eliminate the unfavorable background and useless tissues.
- Noise removing. Median filtering which is non-linear filtering with mask $[3, 3]$ is employed to remove the outliers points.
- Registration. Although the advanced equipment is available that can substantially shorten

$Parameters$	$Range$	$Step$
hs_{MS}	1 to 5	0.5
hr_{MS}	5 to 100	5
hs_{RG}	1, to 3	0.5
hr_{RG}	2 to 10	2

Table 10.1: Scale parameter ranges of CGNG for medical data.

$Parameters$	$Range$
hs_{MS}	1 to 5
hr_{MS}	5 to 100
hs_{RG}	1, $\sqrt{2}$, 2, $\sqrt{3}$, 3
hr_{RG}	1 to 10

Table 10.2: Scale parameter ranges of QRNG for medical data.

the data acquired procedure time, we can not assume that there is no movement among the different scans. Registration processing, which transforms different sets of maps into one common coordinate system (based on ADC), will be done first in order to be able to compare or integrate the data obtained from these different maps.

– Normalization. The normalization step is employed to have a common range [0,255] for *mean shift* and *region growing* bandwidth parameters among studies.
– Interpolation. As maps are obtained from curve fitting (*e.g.* MTT and TTP parameters) and feature detection (max), some voxel value can be wrong or set to abnormal value. This interpolation step try to retrieve such values and use a linear interpolation way to modify them.

10.3.3 CGNG for *mean shift* and *region growing*

For CGNG, an exhaustive search on regular-grid sample is utilized for bandwidth selection. The range and interval are in table 10.1. 5000 sets of bandwidth of parameters are generated for *mean shift* filtering and *region growing* segmentation. These experiments are executed in parallel on a cluster of computers and the EGEE Grid for efficiency and time-consuming [Li 10]. With the help of the reference (manually delineation based on T2-FLAIR maps by expert), the best final segmentation of infarct and the best combination of different parameters are chosen.

10.3.4 QRNG with *PM*

For QRNG, we build a four dimensional space according to the range of four parameters, a group of quasi-random parameters which includes 1000 samples is created for *mean shift* filtering and *region growing* segmentation. The ranges of the parameters are in table 10.2. The *PM* is summed from a series of *mean shift* filtering and *region growing* segmentation results. The values of *PM* are normalized from [0, 1].

10.3.5 Seeds selection in *region growing* segmentation

The selection of seeds is crucial as it determines what are the feature of interest of the data and what is irrelevant. The manually uniformed distributed seed selection according to PWI parameter (TTP) is applied for rats' application for the sake of consideration of accuracy and time-consuming (17 seeds). For the human data, the seeds are derived from manually delineation of expert based on DWI map as the mask of DWI map can be considered as the core of infarct [Wu 01, Rosso 09, Olivot 09].

10.3.6 Post-processing

Post-processing step is an optional step depending on the segmentation result and the expected result, *i.e.* morphological mathematics processing might be helpful in order to obtain homogeneous maps. Indeed, in our context, we perform two times dilation and two times erosion with a "disk" of radius=2 as structuring element (two consecutive opening operations). Moreover, an optimized thresholding method can be employed to acquire the binary segmentation result.

10.4 Segmentation validation criteria

In order to validate the quantification of infarct, we first present some concept of statistical hypothesis testing [Fawcett 04].

A statistical hypothesis testing is a method of making decisions using data, whether from a controlled experiment or an observational study. The test requires an unambiguous statement of a null hypothesis, which usually corresponds to a default statement like in our case is that all the white points delineated by expert are infarct. An alternative hypothesis is the negation of null hypothesis, for example, all the black points outside the infarct are not the infarct. The golden standard of final infarct delineated by expert is also called reference infarct. The goal of the test is to determine if the null hypothesis can be rejected.

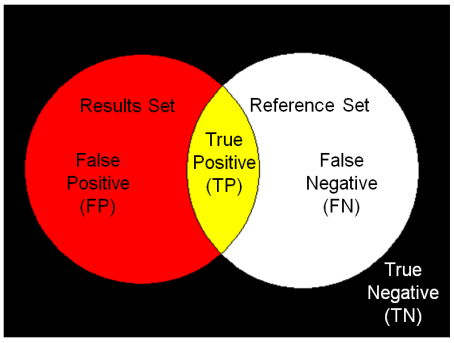

Figure 10.2: Statistical Error Description.

As explained in Figure 10.2, the desired outcomes of the test are called true positive (TP) and true negative (TN). TP means rejecting null hypothesis when it is false and TN means not rejecting null hypothesis when it is true. In our case, the correct decision has been made when segmented

results totally in correspondence with the reference infarct (binary prediction manually by expert). However, if the result of the test does not correspond with reference, then two kinds of error occur.

A type I error, also known as a false positive (FP), occurs when the tested pixel detected as infarct, but it not belongs to the reference infarct. A type II error, also known as a false negative FN, occurs when the pixel of Results Set fails to be recognized as the infarct when this pixel indeed belongs to Reference Set.

Note that during penumbra segmentation, the DICE criteria (in section 6.2.3) is also employed as the critical criteria used to choose the best segmentation result.

10.4.1 Sensitivity and specificity

Sensitivity and specificity are two statistical measures which are closely related to the concepts of type I and type II errors. Sensitivity measures the fraction of true positives that were included in a segmentation, as given by the formula: TP/(TP+FN). A score of 1 indicates that all members in Reference Set were in the Results Set, *i.e.* all voxels in the ground truth infarct were included in the segmentation result.

This measure does not include False Positives or True Negatives, and thus only indicates what fraction of the Reference Set was included in the Results Set. It should be applied with the specificity measurement to measure segmentation quality. Specificity measures the fraction of negatives that are correctly detected, as determined by the formula TN/(TN+FP). For brain infarct segmentation, this is measuring which fraction of non-infarct voxels in the image were excluded. For any test, there is usually a trade-off between the measures.

10.4.2 ROC curve

A perfect situation would have 100% sensitivity and 100% specificity, while which could not be achieved in the real life. Scientists try to strike a balance between sensitivity and specificity. To do this, they plot "sensitivity" and "1-specificity" on a graph, called a 'ROC curve' (ROC means Receiver-Operator-Characteristic) .

10.5 Conclusion

In this chapter, we propose specified framework for automatically estimate the ischemic penumbra according to different ways of choosing bandwidth parameters. Also, we present several evaluation criteria (DICE see equation 6.1 Sensitivity and specificity, ROC curve) used for segmentation result. In the following chapter, we detail the medical data and its properties.

Chapter 11

Data and Materials

11.1 Introduction

In this chapter, two groups of data set and their properties are introduced for quantifying the ischemic infarct. First group is animals' data presented in section 11.2 and the second is patients' data presented in section 11.3.

11.2 Rats' data

The input data used for our application are obtained by mechanically provoking an ischemic stroke in rats. Further information are given in [Chauveau 11]. Such rats' data are employed as an instructive research for ischemic patients.

11.2.1 Description of rats' data

In this study, two groups of male Wistar rats with acute ischemia stroke were included in the table 11.1.

$index$	$pMCAO$	$Reperfused$
pMCAO2	yes	
pMCAO4	yes	
dha81		yes
dha82		yes

Table 11.1: Information of the rats.

All the rats were subjected to unilateral middle cerebral artery occlusion (MCAO) by insertion of an intraluminal filament on the rat's brain using a filament inserted in External Carotid Artery (ECA)(see figure 11.1). For the two first rats (Index: pMCAO2, pMCAO4), no re-perfusion were done. In another word, the MCA will be permanently occluded for these rats. The CCA is common carotid arteries.

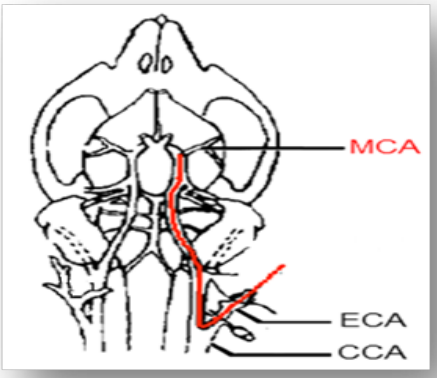

Figure 11.1: Ischemia on rat's brain.

11.2.2 Information about MRI acquisition [Chauveau 11]

MRI experiments were performed on a Bruker Biospec 7T/12cm horizontal magnet equipped with Paravision 4.0. A birdcage head-coil of 72mm inner diameter was used for RF transmission and a 15mm diameter surface coil for reception. The rats were placed in a cradle equipped with a stereotaxic holder, an integrated heating system to maintain body temperature at $37 \pm 1°$C, and a pressure probe to monitor respiration. Time of flight (TOF) MRA was performed using a two-dimensional multislice gradient echo sequence with 256*128 matrix, a FOV of $3.7 \times 2.5cm^2$, 80 non-contiguous slices (slice thickness is 1mm and the interslice overlap is 0.15mm), TE/TR$=$ $5/25$ms and 2 averages (the duration of TOF sequence is 6min 24sec).

T2-weighted images were acquired using a RARE sequence with a 256*256 matrix, FOV=4*4cm^2, TE/TR$=$ $75/3000$ms, 2 averages and 7 non-contiguous slices (slice thickness is 1.5mm and interslice gap is 0.5mm), covering the entire MCA territory (the duration of TOF sequence is 3min 12sec).

DWI echo planar imaging (EPI) spin-echo images were acquired using the same FOV and slice characteristics as before, with matrix 128*128, TE/TR=$25/2000$ms and 3 b-values of 0, 1500, and 3000s/mm^2 (7min 28sec). PWI was performed with multislice dynamic susceptibility contrast-enhanced MRI (DSC-MRI) using a gradient-echo sequence with the same FOV and slice characteristics (acquisition with matrix 96*96 and TE/TR=$4.84/100$ms, reconstruction with matrix 128*128). One hundred consecutive images were acquired per slice with temporal resolution of 0.6s (1min), with a 0.5mL i.v. bolus of gadolinium (Dotarem, Guerbet, Aulnay-sous-Bois,

France) injected after acquisition of the 15th image.

11.2.3 Derivation of multi-parametric maps on rats

See figure 11.2, the functional multi-parametric MRI are acquired: DWI to characterize core of infarct and PWI to test the tissue at risk. From an image acquired by DWI, it is possible to extract the ADC for each voxel and to obtain a map representing local diffusion properties. PWI by DSC MRI utilizes very fast imaging to capture the first pass of intravenously injected paramagnetic contrast agent, hence the bolus tracking to obtained the maximum peak concentration (MPC) parameters (peak, TTP). Only peak and TTP maps are available in animals as other parameters require AIF which do not has sufficient spatial and temporal resolution in small animals.

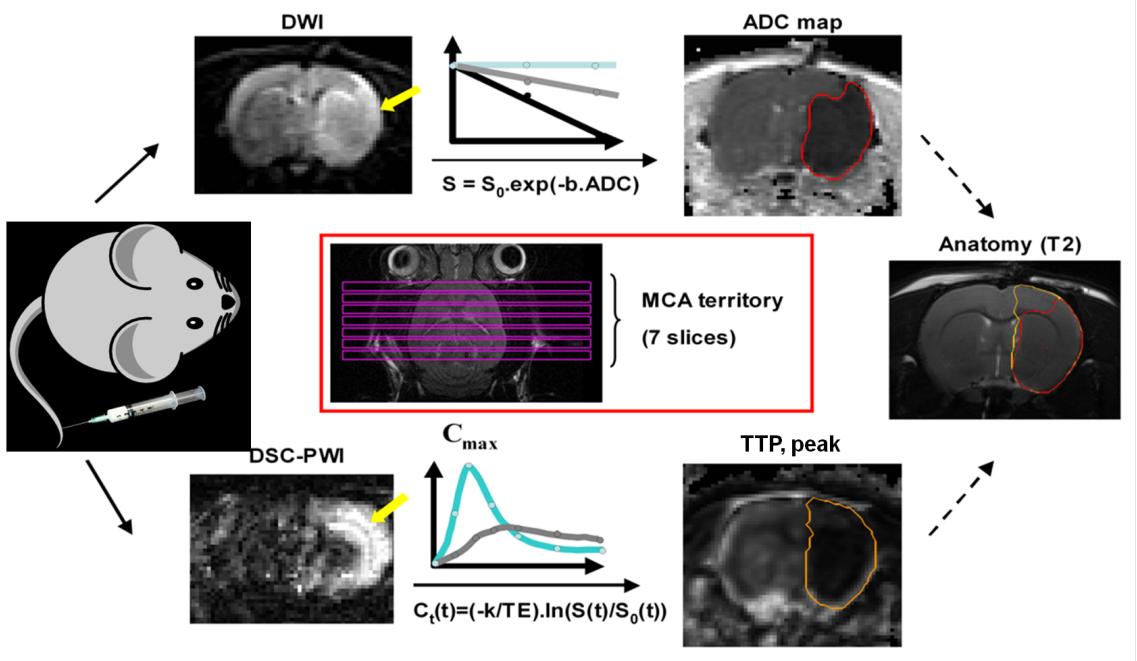

Figure 11.2: Multiparametric MRI acquisition of rats study.

The anatomical MRI were performed again at 1 day or 4 days after ischemia onset. Each rats has the complete DWI with the ADC parameter (*e.g.* figure 11.4) and the PWI with the peak and TTP parameters (*e.g.* figure 11.5) at day 0 as well as anatomical T2 map at day 4 or subsequent days (*e.g.* figure 11.6).

TTP is the most used parameter in the clinic owing to its robustness and simpleness to compute as well as its obvious interpretation of images. However, it can not solve the problem of isolation points. We only observe the region where the contrast agent arrival is severely delayed due to the limited temporal resolution (0.6 s).

The ghosting effect of ADC in figure 11.4 is due to the fast EPI acquisition. See the acquisition information in figure 11.3.

Figure 11.3: Rat data description along time.

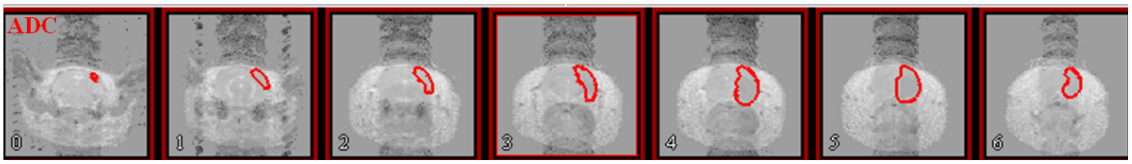

Figure 11.4: ADC at day 0 with reference infarct (seven slices of rat pMCAO2).

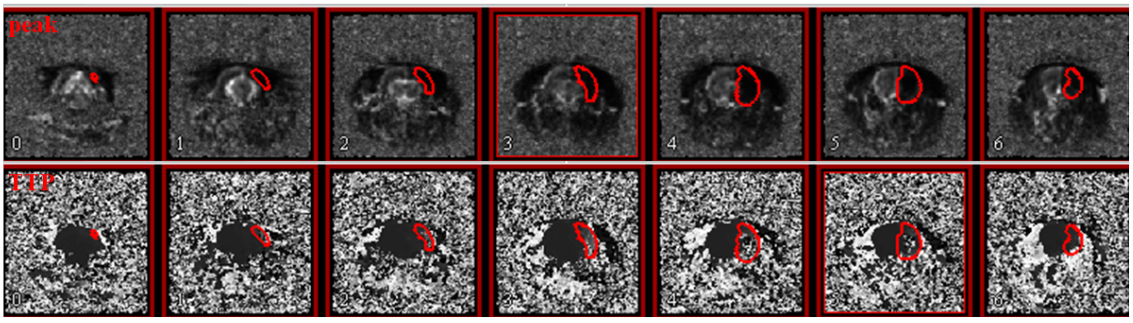

Figure 11.5: peak and TTP at day 0 with reference infarct(seven slices of rat pMCAO2).

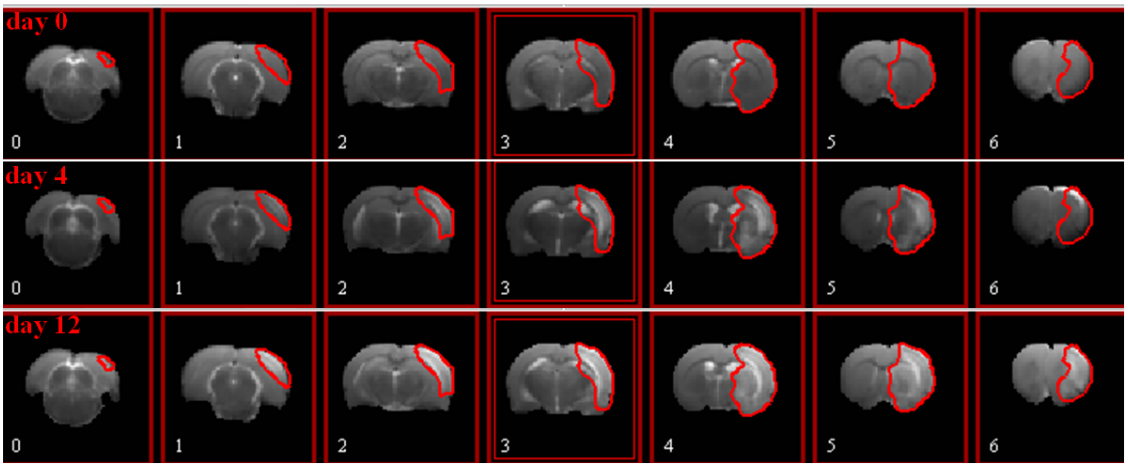

Figure 11.6: T2 anatomical image at day 0, day 4 and day 12 with reference infarct (seven slices of rat pMCAO2).

11.2.4 Properties of rats' data

The primary aim of this study is to estimate the evolution of penumbra, which means predict the infarct at day 4 or day 12 based on both DWI and PWI parameters at day 0. However, we still need to face these problems derived from rats' data.

1. Limited numbers of pixels and low resolution: Although the number of pixels acquired for brain rat consists of 7 slices of 128×128 pixels, the actual region of interest containing the brain is only around 50×50 pixels.
2. Artefacts and deformation: The artefacts are inevitable due to the EPI acquisition technique. All the sequences are optimized so that deformation is minimal, but ghosting effects remain on DWI.
3. Visual bias: The final validation is manually delineated by experts. It might be not so accurate due to the highly noisy background.

11.3 Humans' data

11.3.1 I-KNOW database

The data used in this thesis are from the 'I-KNOW database' consisting of real images of people who have suffered stroke (http://www.i-know-stroke.eu/). This database is aim in developing advanced models of the progression of brain damage immediately after acute stroke. The maps are all of dimension 128*128*20 (20 slices each of spatial dimension 128 by 128 pixels). Currently, there are over 80 patients available for developing advanced models of the progression of brain damage immediately after acute stroke. The detailed explanation and analysis are provided in [Ritzenthaler 05]. We have only carried out tests on 2 selected patients without reperfusion: patient171, patient255.

Different from the traditional segmentation problem, the final infarct observed thirty days after the stroke (day 30) using the data acquired immediately after the stroke (0<t<4.5h). This observation is based on the hypothesis that DWI map presents the core of infarct and mismatch DWI/PWI presents penumbra. Therefore, despite the large number of patients available, choosing suitable candidates for the study should be done carefully, considering the following points.

1. As the treatment will reduce the final infarcted volume, the reference manually segmented at day 30 will be smaller than any estimation based on the first hour data.
2. The patients have different degrees of self-recovery for injured tissues. It results in a diversity of lesion after several days.
3. If the stroke is on a small vessel (and so natural re-perfusion can appear), then the degrees of self-recovery for injured tissues is often better than a stroke on an "important" vessel.

11.3.2 Derivation of multi-parametric maps on human

The derivation of multi-parametric maps of human data are identical with the one used for rats in the figure 11.2. For each patient, the perfusion and diffusion maps are acquired after ischemic onset (<3h). Also, a fluid attenuated inversion recovery image (FLAIR) is acquired 30 days after the initial scan (see figure 11.7).

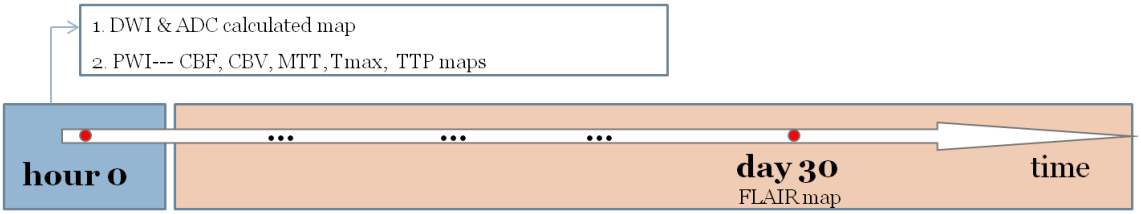

Figure 11.7: Human data description along time.

11.3.3 Properties of human's data

One slice of each available parameter is illustrated by figure 11.8.

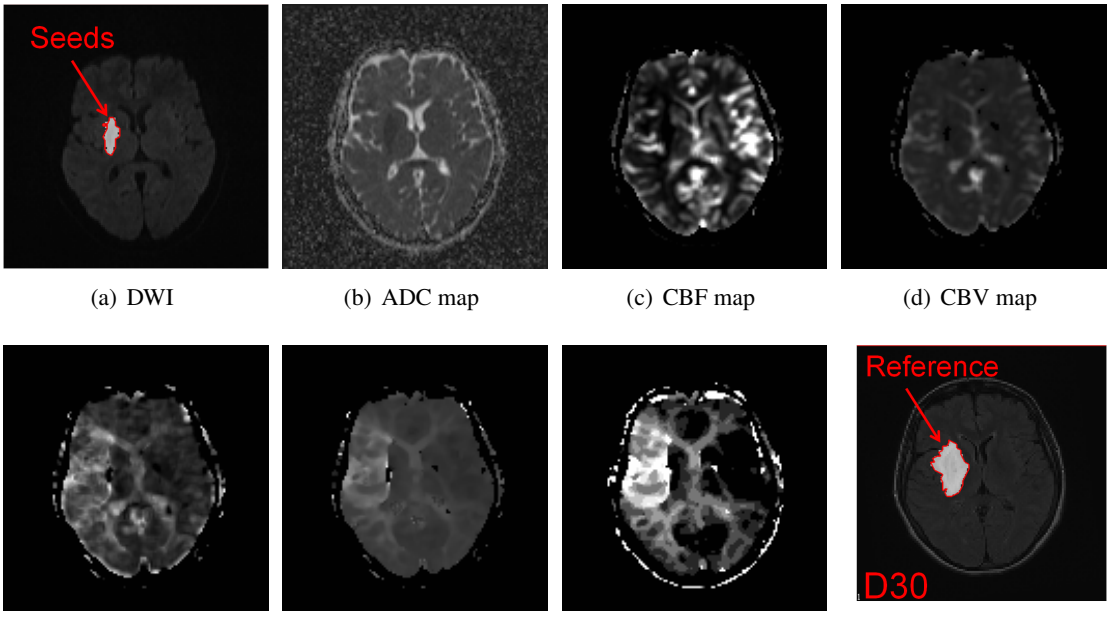

(a) DWI (b) ADC map (c) CBF map (d) CBV map

(e) MTT map (f) TTP map (g) Tmax map (h) T2 FLAIR map

Figure 11.8: Human ischemic multi-modal MRI parameters illustration (11th slice of patient171).

Since both of the microscopic diffusion of water molecules and the blood perfusion characteristics are affected seriously in the condition of ischemic onset, ischemia condition alters the values of these parameters (*e.g.* ADC, CBV, CBF, MTT, TTP) in the ischemic regions as compared to the non-ischemic regions of the brain. The hypothesis is that these parameters are able to characterize the ischemic conditions and are thus referred to as characteristics or features of the ischemic condition.

Analogically to the rats' data, human ischemic data suffered from high noisy background and deformation problems. Besides, the MTT and TTP parameters are suffering dark points problems as a result of fit error during the deconvolution process.

11.4 Conclusion

In this chapter, we present the specified rat and human data on which we have tested our framework. The results obtained on these multi-slice for the infarct prediction as well as a framework evaluation are presented in the next chapter.

Chapter 12

Results

12.1 Introduction

In this chapter, we present results obtained from preclinical and clinical in two parts. The first part deals with rats data where ischemia is provoked in the MCA temporary to quantify evolutionary infarct. The second part deals with human ischemic data.

For each part, by using CGNG method, we present the final segmented results compared with the reference infarct which are delineated by a medical expert. Moreover, the ability of different combinations of multiple MRI parameters is evaluated. Finally, we analyze the ability of *PM* to provide the favorable final infarct segmentation by combining some of the available MRI modalities.

12.2 Results of rats data

The experiment on rats' data is performed in voxel-based techniques that combine multiple MRI modalities. The different feature properties possible with DWI and PWI mismatch information are synthesized in a unique feature space.

In this study, four rats are employed in predicting infarct, and we test the three following combinations of parameters:

– ADC and peak,

– ADC and TTP,

– ADC, peak and TTP.

Final reference T2 map at day 4 is registered based on the T2 map on day 0 using 3D optimized automatic registration in MIPAV software (http://mipav.cit.nih.gov/). The 3D optimized automatic

registration determines a transformation that minimizes a correlation ratio and evaluates the correlation ratio at several different image resolutions, starting with the lowest resolution. Each step of increasing resolution utilizes the previously determined optimal transformation as a starting point and further refines its values.

The brain mask is employed separately for DWI and PWI parameters (ADC, peak and TTP in figure 12.1). Additionally, the seeds are manually selected based on TTP map. All the input maps of day 0 are normalized into a range [0,255]. The final reference is delineated manually by the expert based on the T2 map of day 4 or day 12.

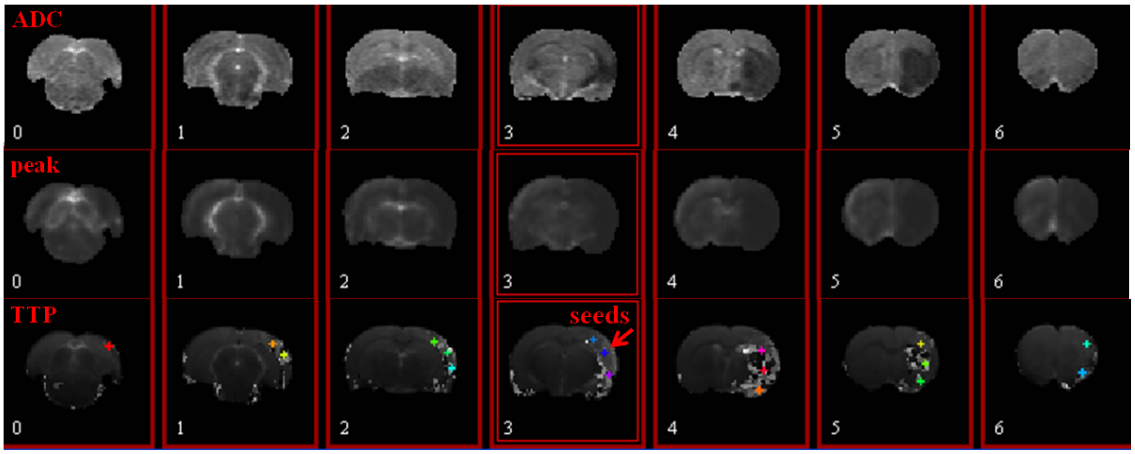

Figure 12.1: ADC, peak and TTP (with manually selected seeds) after using brain mask (seven slices of rat pMCAO2).

DICE coefficient is applied as a global standard to evaluate our algorithm as well as the best segmentation result. The next section introduce firstly the results of proposed framework by using CGNG.

12.2.1 Final infarct segmentation by using CGNG

Infarct segmentation result

In figure 12.2, we present the final infarct segmentation obtained on the rat pMCAO2 with combination of ADC and peak by using CGNG. The whole slices of ADC, ttp, and peak of day 0 are shown as input. Additionally, the T2 maps of day 0 and day 12 are presented as reference. There is no visible infarct from the T2 map of day 0. We perform the experiments into two ways: single *region growing* (onlyRG) and hybrid *mean shift* and *region growing* (MS+RG) for segmenting infarct.

The final segmentation is compared with the reference based on T2 map of D12. The global optimal DICE$^* = 0.81$ computed on the whole seven slices based on hybrid MSRG method. The bandwidth parameters are selected separately for *mean shift* and *region growing*. The hs_{MS} varies from 0.5 to 5 using an interval of 0.5 and hr_{MS} varies from 5 to 100 using an interval of 5, hs_{RG} varies from 1 to 3 using an interval of 0.5 and hr_{RG} varies from 2 to 10 using an interval of 2.

Performed by using four parameters with refined intervals, 6000 binary segmentation results

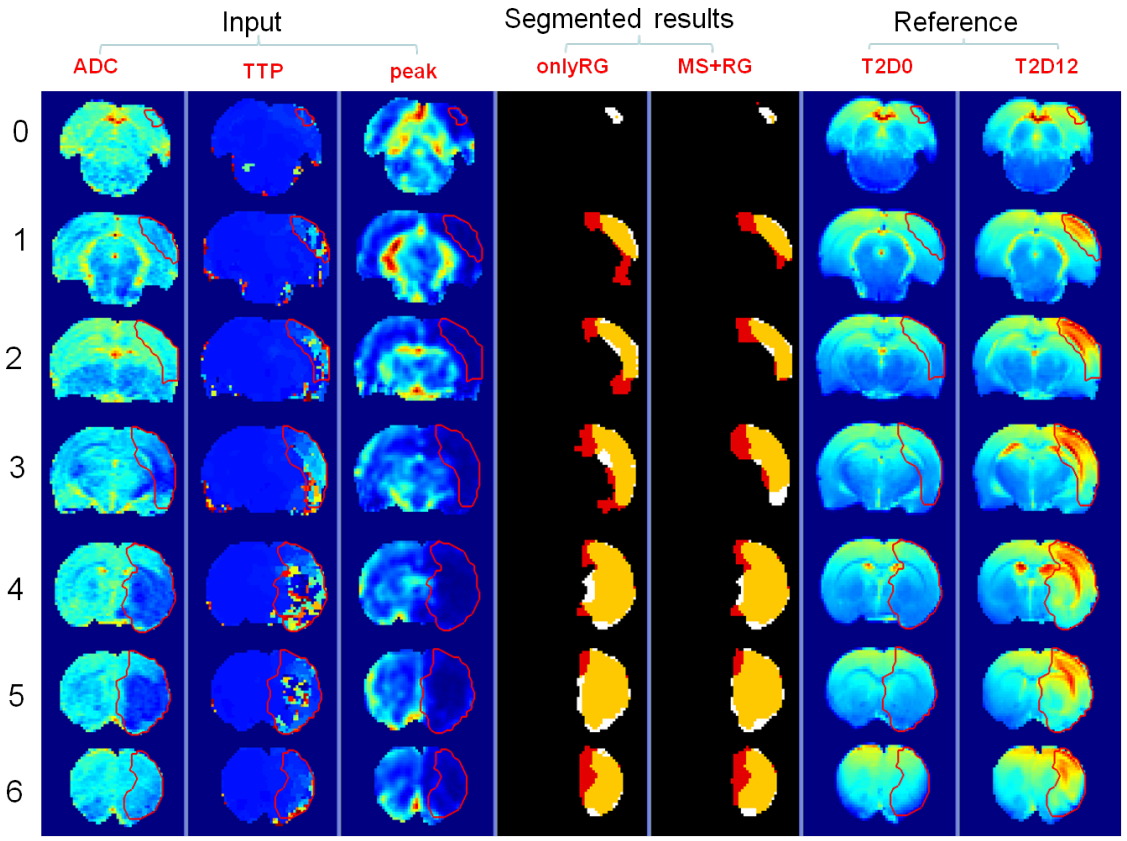

Figure 12.2: Optimal final infarct segmentation of 'pMCAO2' with ADC and peak.

are obtained. The average computational time for one group of parameters is 2.5 minutes and the total time is 245 hours.

Comparing to the single *region growing*, the hybrid algorithm which combines *mean shift* and *region growing* always obtains better results for all the combinations according to the optimal DICE, see the table 12.1.

DICE*	ADC, peak	ADC, TTP	ADC, peak, TTP
MS+RG	0.81	0.66	0.65
onlyRG	0.67	0.29	0.59

Table 12.1: Proposed framework compared with 'onlyRG' framework according to DICE coefficient.*

Comparison of multiple MRI parameters

DICE*	ADC, peak	ADC, TTP	ADC, peak, TTP
$pMCAO2$	0.81	0.66	0.65
$pMCAO4$	0.86	0.72	0.78
$dha81$	0.79	0.49	0.74
$dha82$	0.81	0.53	0.76

Table 12.2: Comparison of different combination of multi-model MRI parameters on rats according to optimal DICE coefficient by using proposed framework.

Table 12.2 shows the comparison of different combination of multi-model MRI parameters. According to the optimal value of DICE, the "ADC and peak" always has a trend to acquire the best results of prediction for rats' experiment. For rats' data, TTP is not highly recommended in our framework, since it is a uncomplete parametric map with the discontinuousness in the penumbra region.

We present the ROC curve of final infarction results according to the 5000 groups of parameters tested. The ROC curve is delineated according to the "sensitivity" and "1-specificity" in figure 12.3. We employ three order polynomial regression of figure 12.3 in figure 12.4. The optimal result should be the shortest distance to the red star.

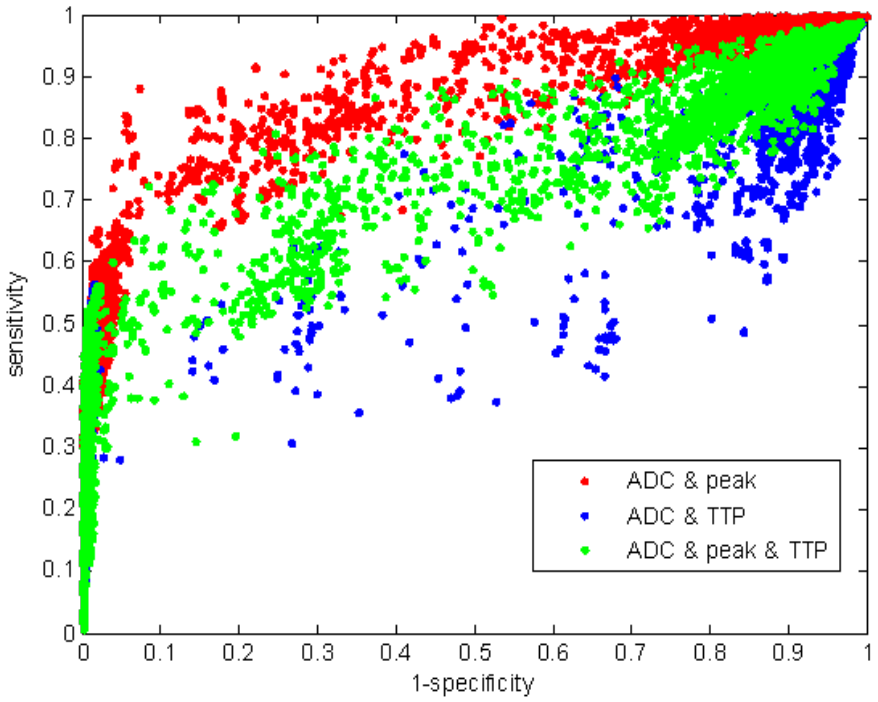

Figure 12.3: Optimal predictor of different combination of multi-modal MRI parameters based on ROC curve before polynomial regression (pMCAO4).

According to figure 12.4, the combination of "ADC and peak" is shown to be always the best predictor for final segmentation compared with combination of "ADC and TTP" and "ADC and peak and TTP".

12.2.2 *PM* by using QRNG

Illustration of PM results

In this subsection, 1000 groups of bandwidth parameters are created by using QRNG method. After *mean shift* filtering and *region growing* segmentation, we build the *PM* for three combination of parameters.

Figure 12.5 shows a *PM* example for rat 'pMCAO2'. The *PM* would be helpful to provide possible probabilistic information of the tissue in cerebral as the final infarct. The higher value

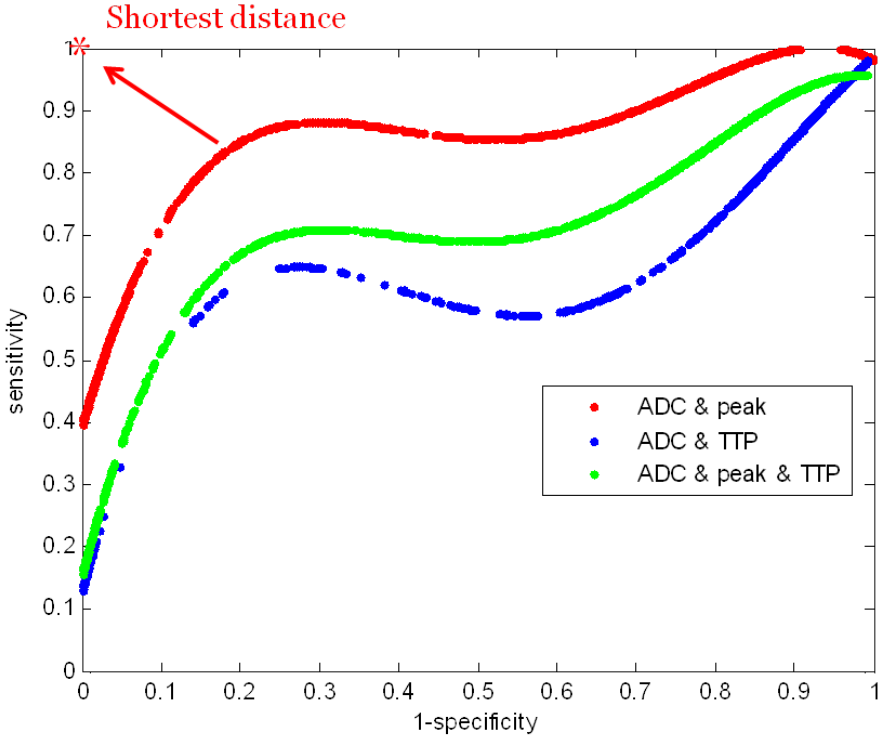

Figure 12.4: Optimal predictor of different combination of multi-modal MRI parameters based on ROC curve (pMCAO4).

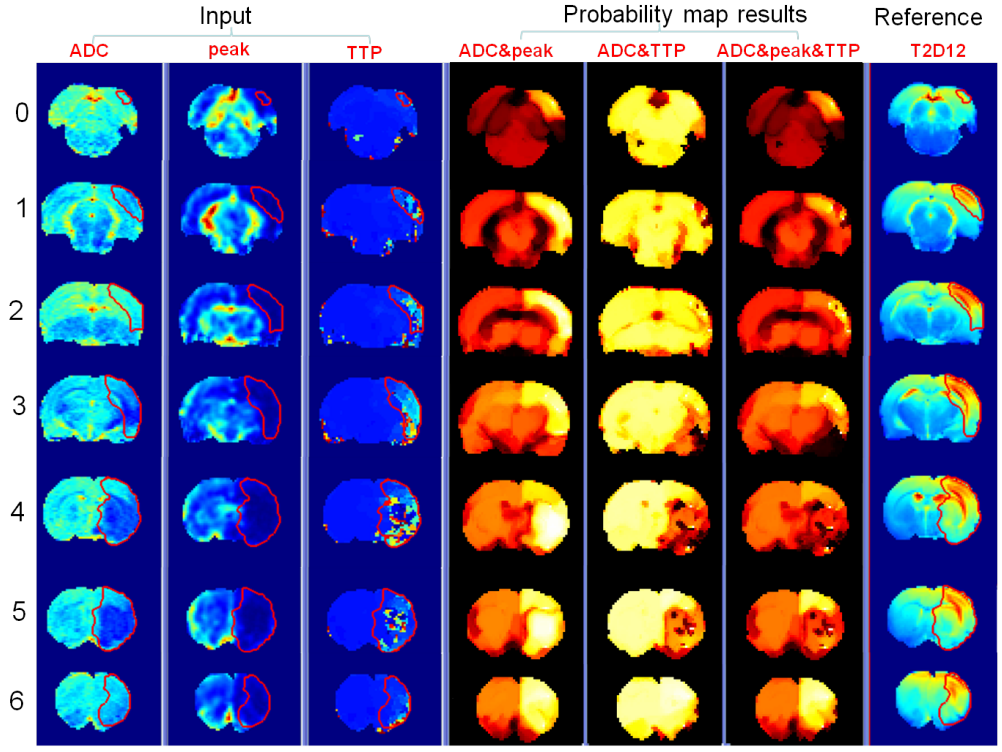

Figure 12.5: PM for predicting infarct of pMCAO2 with three combinations.

of the *PM* indicate the higher possibility of cerebral tissues belong to the final infarct. In the following step, the optimal morphological processing or a binary segmentation would be employed to quantify the final infarct easily. In the following, we discuss the convergence properties of *PM* by using bootstrap method.

Convergence properties of PM

The *PM* can be seemed as an estimation of final ischemic infarct. In order to validate the efficiency of this estimation, bootstrap method is employed to assess the bias and variance.We observe the convergence of the bias and variance of *PM* estimation according to the increase of samples (groups of bandwidth parameters).

The figure 12.6 presents the convergence of bias and variance of *PM* based on DICE criteria. We randomly and repetitiously (30 times) sample the 1000 groups of bandwidth (from 10 to 500) to build a *PM* and then we employ optimized binary segmentation method to obtain the optimal DICE. We compute the mean and standard deviation of 30 times selection of certain groups of bandwidth.

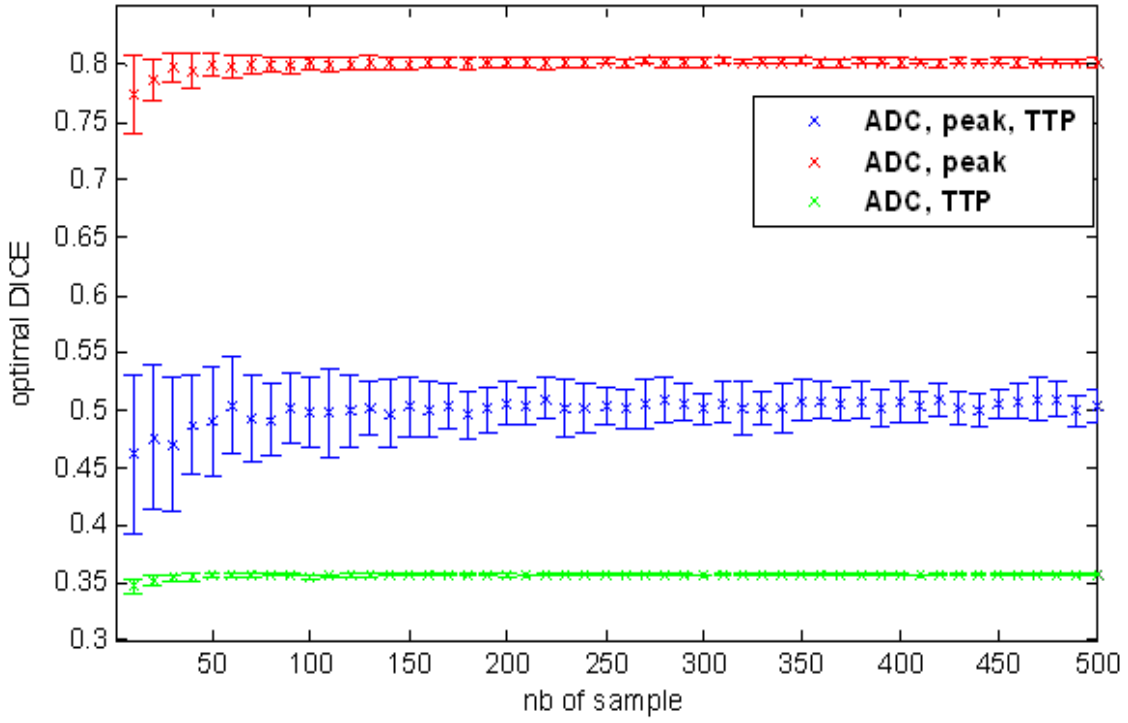

Figure 12.6: Convergence of bias and variance of PM by using bootstrap method (rat pMCAO2).

From figure 12.6, the combination of ADC and peak, we observe that the optimal DICE converge at over 0.8 before number of samples equal to 100. The standard deviation decrease to 0.01 as the increase of number of sample. Reminding that consuming time of one group of parameters is 2.5 minutes. The total time for these 100 samples is 4 hours. The QRNG is less time-consuming than CGNG in optimizing final ischemic infarction.

This re-sampling method is employed on the three combinations of DWI and PWI parameters. Same with the previous conclusion of best predictor of various multi-modal parameters, the ADC

and peak has the trend to best estimate the final infarct at D12 based on rat pMCAO2. The optimal DICE for these three combinations is obtained before number of samples at 100.

After the ischemic onset (day 0), the *PM* is able to provide information of the possible final infarct at several days after (day 12) without using any reference infarct. However, there are several precautious to take for such *PM* computation: 1) 'Enough' samples (here are the number of bandwidth parameters) need to be considered. 2) The bandwidth parameters should be randomly selected following uniformed law.

12.3 Results of patients' data

In this preliminary study, two patients are included with PWI/DWI performed in predicting infarct test with multiple MRI modalities: ADC, CBF, CBV, Tmax, DWI, MTT, TTP with the first hour following stroke onset. Also, we have the final validation reference mask of MRI T2 FLAIR map after 30 days. The five combinations of multiple MRI parameters are selected as follows:

- TTP, MTT
- ADC, DWI
- TTP, MTT, CBF
- TTP, MTT, DWI
- TTP, MTT, ADC, DWI, CBF.

A whole brain mask is delineated by an expert for decreasing disturbing tissue exterior brain. All maps were co-registered using optimized automatic registration 3D in MIPAV software to one another based on the ADC parameter of hour 0. All the input maps are normalized into a range [0,255]. The seeds are manually delineated by doctors based on DWI map which shows the core of infarct during early period. The final reference is delineated manually by the expert based on T2 FLAIR map on day 30.

As a results of better efficiency of the QRNG method, the results of human are shown only using QRNG. Firstly, we present the final segmentation as well as the best predictor of multiple MRI modalities according to the DICE coefficient. Secondly, we illustrate the results of *PM* and its properties based on human data.

12.3.1 Final segmentation

Final segmentation illustration by using QRNG

The proposed framework is employed on the human171 data based on these previously defined five combinations. We present the final segmentation on 20 slices based on combination of TTP, MTT, ADC, DWI, and CBF as an illustration (see figure 12.7).

From figure 12.7, we can clearly see there is no infarct from slice 0 to slice 6 and from slice 17 to slice 19. In the middle slices 13 to 15, the segmented results are pretty good (according to the DICE computation in figure 12.8). However, for the upper slice 16 and bottom slices 9 to 12, the results are not so satisfying. This can be explained from the medical point of view that these slices contain the oligemia region which is actually hypo-perfused but can naturally re-perfused through

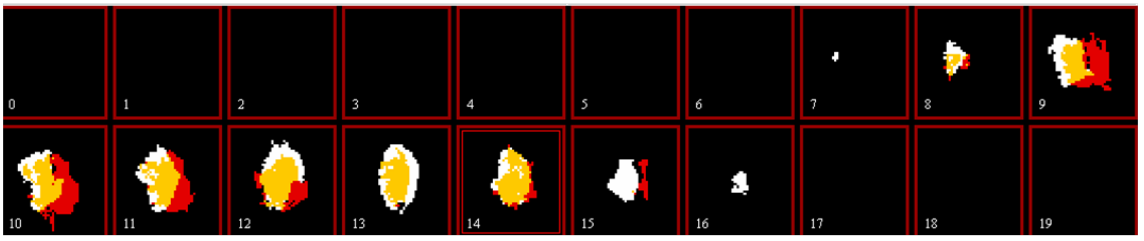

Figure 12.7: Infarct segmentation of combination of 5 *parameters (Patients171).*

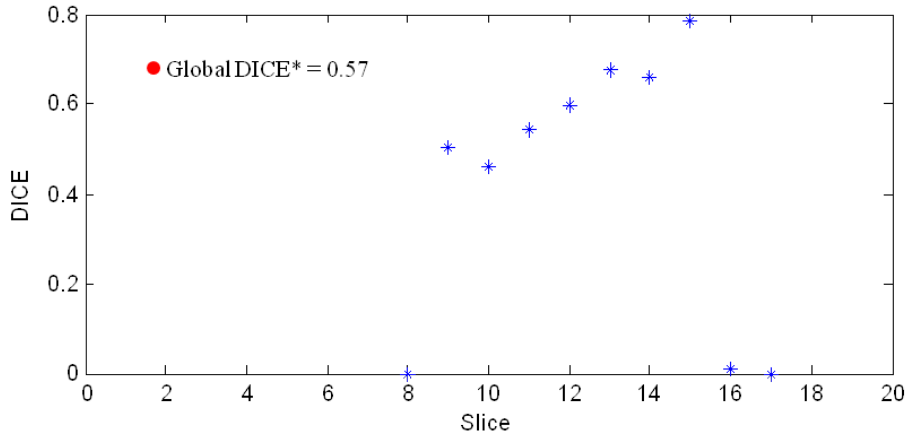

Figure 12.8: DICE for each slices of figure 12.7, the yellow region is the true segmented points, the red region is over-segmented points and the white region is under-segmented points (Patients171).

other vessels. These effects could hardly be anticipated and prevented. As a consequence, it will seriously influence the quality of segmented infarct since the global DICE* =0.57 is computed by all the slices.

Comparison of multiple MRI parameters

We present the comparison of different combinations of multi-model MRI parameters on human infarct segmentation in table 12.3. According to the global DICE*, the combination of TTP, MTT, ADC, DWI, and CBV gives the best predictor of the final infarct. The TTP, MTT and CBF are the most helpful, and adding ADC and DWI have a slight improvement with patient 255.

DICE*	TTP, MTT	ADC, DWI	TTP, MTT, CBF	TTP, MTT, DWI	TTP, MTT, ADC, DWI, CBF
Patient171	0.54	0.54	0.57	0.55	0.57
Patient255	0.32	0.42	0.45	0.38	0.47

Table 12.3: Comparison of different combination of multi-model MRI parameters on human according to optimal DICE coefficient by using proposed framework.

As a conclusion, the segmentation work flow is feasible in predicting irreversible infarction. The combination of multiple MRI modalities is more flexible and precise in allowing therapeutic decisions to be based on individual patient pathophysiological information. The first results obtained with our segmentation framework show that using mainly (TTP, MTT and CBF), a prediction of irreversible infarction is partly possible, but will be limited depending of the slice position.

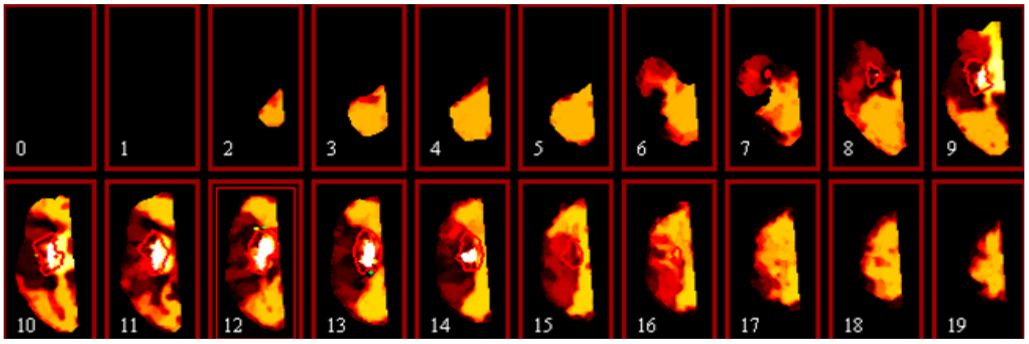

Figure 12.9: PM of multi-parameters: TTP and MTT for 20 slices with reference segmented results at days 30 *(Patients171).*

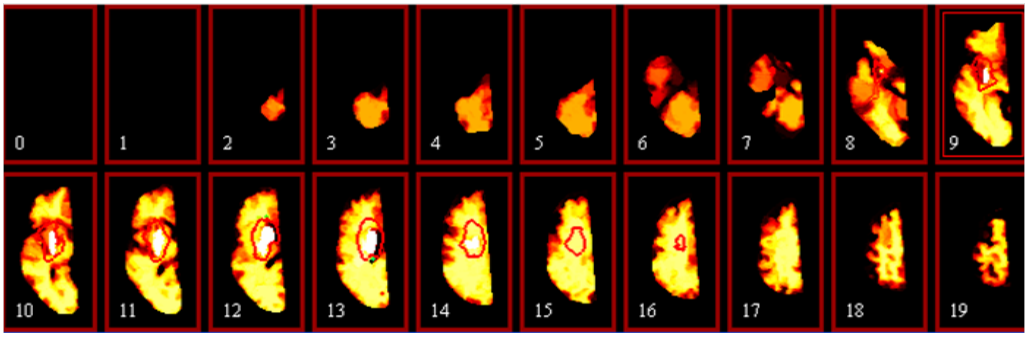

Figure 12.10: PM of multi-parameters: ADC and DWI for 20 slices with reference segmented results at days 30 *(Patients171).*

12.3.2 Analysis of probability map

In this section, we discuss the *PM* results.

Illustration of PM results

Figure 12.9, 12.10, 12.11, 12.12 and 12.13 are the probability map obtained on human171 with 100 groups of bandwidth parameters based on the various combinations of available DWI/PWI maps .

According to the combination of various multi-modal parameters, we synchronize more information to segment the penumbra at the first time after ischemic onset. Based on the hypothesis

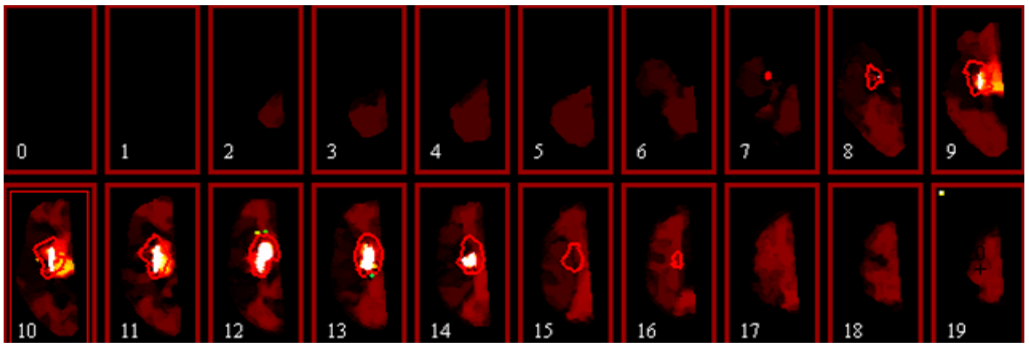

Figure 12.11: PM of multi-parameters: TTP, MTT and CBF for 20 slices with reference segmented results at days 30 *(Patients171).*

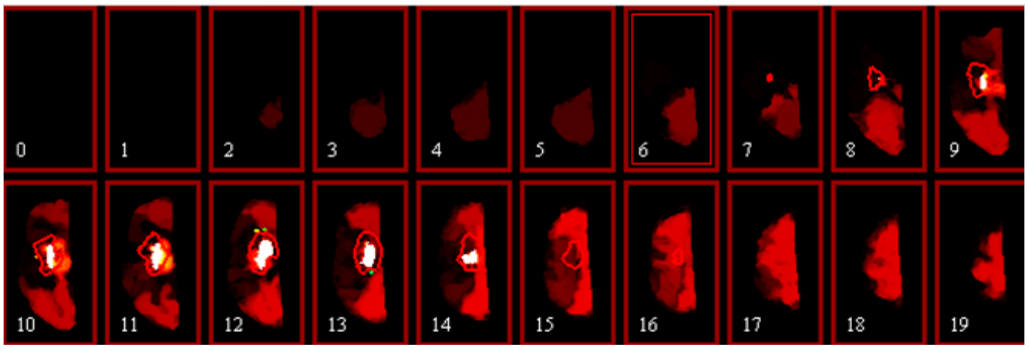

Figure 12.12: PM of multi-parameters: TTP, MTT and DWI for 20 slices with reference segmented results at days 30 *(Patients171).*

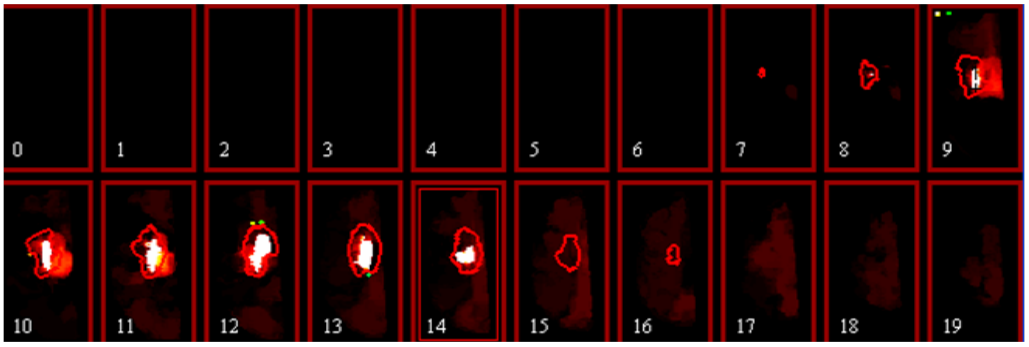

Figure 12.13: PM of multi-parameters: TTP, MTT, CBF, ADC and DWI with reference segmented results at days 30 *(Patients171).*

that the PWI could give the propagation information of penumbra evolution. The *PM* results are able to provide the estimation of final infarct at following days. Visually, as we measure it for the QNRG framework, the TTP, MTT, CBF, ADC and DWI combination provides the best result, close to the final reference infarct.

Following *PM*, a threshold optimized method is employed to search the optimal DICE result for the five combinations (figure 12.14). Figure 12.14 shows that the (TTP, MTT, CBF, ADC and DWI) presents the best DICE (0.55) with a small improvement ($+0.01$) compared to (TTP, MTT, and CBF).

The DICE of optimal threshold of PM calculated from five combinations is 0.55 for patient171 and 0.50 for patient255.

12.4 Conclusion

In this chapter, we present ischemic infarct results of rat and human based on the proposed *PM* framework. For rats, it is shown that *PM* framework is efficient in estimating the penumbra evolution based on ischemic onset data. The best results are obtained from ADC and peak data, which adding TTP information degrades the results. For human, the preliminary results are not as good as rat's data with some inhomogeneity along slices. Anyway, *PM* method is valid with (TTP, MTT anc CBF) input but note that adding (ADC and DWI) may increase slightly the results.In the

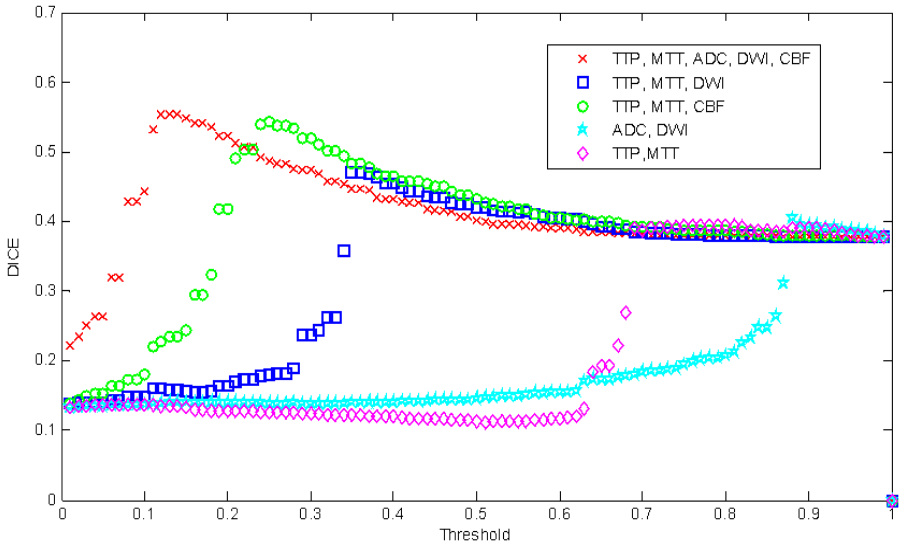

Figure 12.14: Threshold of PM for various combination of multi-parameters (Patient171).

following chapter, we summarize all the discussion and conclusion based on medical data.

Chapter 13

Conclusion and perspectives

13.1 Conclusion

1. The challenge of this medical data is much more than simple segmentation of infarction. It is more like an estimation problem which aims to predict the penumbra evolution after several days by only using the multi-modal MRI parameters obtained from the early period (*e.g.* hour 0 or day 1). In this context, starting from several points of infarct (seeds), the proposed segmentation framework performs on estimating ischemic penumbra based on rats and human data.

   For the rats, the global DICE reaches the value of over 0.8 with the price of high computation according to the exhaustive CGNG method. By using the proposed *PM* with QRNG, we obtain the probabilistic information for estimating the final infarct. Associated to an optimized threshold method, the *PM* method with QRNG can easily converge to the optimal result with hundreds times less time consuming than CGNG method. Additionally, the most attractive aspect of the *PM* method is it does not require any learning step of reference to estimate the final infarct.

   Regarding the human preliminary results, the situation is not so optimistic as there are more factors which influence the final validation of human data. In particular, cerebral of ischemic patients contain the oligemia region which is actually hypo-perfused but can naturally reperfused through other vessels. This case could result in the true penumbra region during the early period change to be recovered after several days after. Thus it brings difficulties to estimate the final infarct and conduct to heterogeneous results depending of the slice positions.

2. We compare the estimation results based on various combination of MRI parameters according to the DICE efficient, ROC curve as well as the convergence of *PM* estimation. We can conclude that combining several multi-modalities of MRI parameters is helpful to improve the final segmentation. But it is not always the more parameters, the better results (see the "ADC, peak, TTP" of rats example). As a consequence, the combinations of input parameters need to be considered carefully.

13.2 Perspectives

In the future, we suggest several perspectives concerning with this medical application as follows:

1. Regarding basic time schedule constraints, we conducted a limited number of data. More real data need to be performed by using the proposed *PM* framework in order to verify its robustness and efficiency.

2. Even if through the *PM* method, the bandwidth choice is used as a 'solution'. The selections of bandwidth parameters for *mean shift* filtering and *region growing* segmentation are of importance to limit computation time. Thus, optimizing the bandwidth parameters is likewise a interesting problem. See the ROC curve with all the DICE coefficients in figure 13.1 based on rat pMCAO4 with combination ADC and peak. For the future work, by using clustering of the bandwidth matrix of pretty good DICE results, we hope to localize several scope of bandwidth parameters that will give high quality of segmentation results.

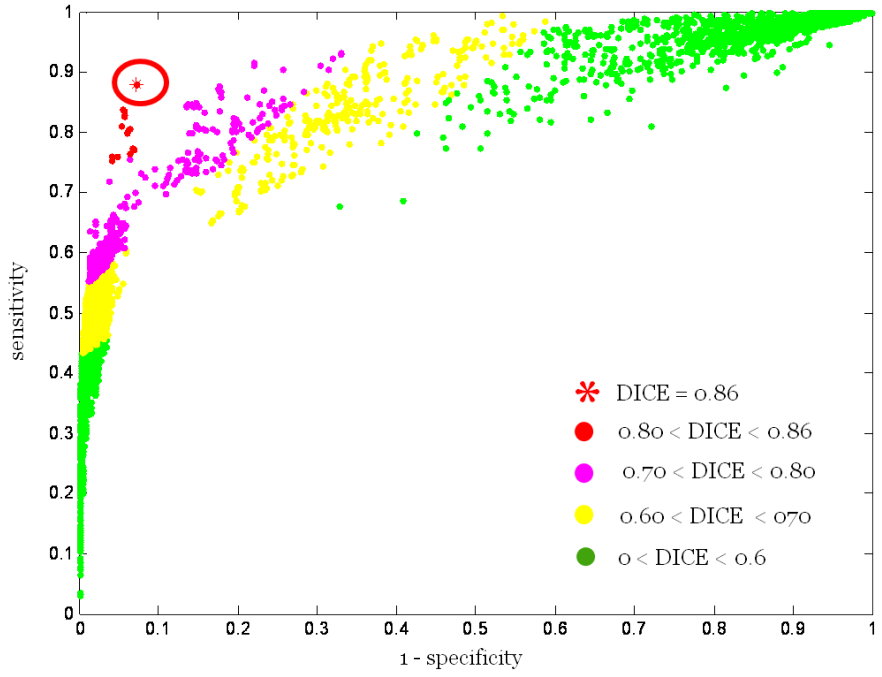

Figure 13.1: ROC curves of 'pMCAO4' reflecting performance of algorithm with DICE.

3. By using *PM* method, we demonstrate that the initial MRI data contain pieces of information that enable some prediction of the final infarct. We will have to compare what kind of results can be obtained by other algorithms (*e.g.* 2D threshold segmentation, adaptive mean shift with high density clustering), including also some with learning step: support vector machine (SVM).
4. It will also interesting to compare *PM* algorithm based results with results of some experts.

IV CONCLUSION and PERSPECTIVES

Chapter 14

General Conclusion and Perspectives

This thesis is devoted to the optimization of *mean shift* filtering and segmentation and its application to multi-modal MRI ischemic data.

In the first part, we present the *mean shift* method based on multi-dimensional feature space analysis and on non-parametric kernel estimation. The procedures of *mean shift* and its advantages and limitations are also detailed.

In the second part, we enumerate the factors which can influence *mean shift* filtering and discuss the mechanism by which they occur. This is the first time that the various noise and blurring effects on *mean shift* filtering are studied in feature space. The parameterizations of the bandwidth matrix is the key point in *mean shift* filtering. Finally, by researching on the influence of bandwidth parameters, a multi-parametric bandwidth estimation Plug-In method is employed on *mean shift* to automatically obtain the optimal global bandwidth parameters.

For the purpose of segmentation and clustering, a new automated segmentation framework which combines *mean shift* filtering and *region growing* segmentation based on regular-grid sampling is proposed. However, the implementation of the framework is such that a reference image is required to optimize the final segmentation results. This is fine when a reference image is available and useful for fine tuning parameters, but it is impractical in real life situations where no reference is available (the reference is the gold standard for comparison - the existence of a reference goes away with the need for an algorithm). In order to eliminate the need for a reference image, we propose a *PM* framework which also reduces the time required for fine tuning all the necessary parameters.

In the third part, the new automatic segmentation volume-based framework which combines *mean shift* filtering and *region growing* segmentation as well as *PM* optimization is applied to the medical ischemic data. With the aim of predicting the penumbra evolution after several days by

only using the multi-modal MRI parameters obtained from the early period (*e.g.* hour 0 or day 1), the proposed segmentation framework gives promising results on predicting final infarct based on rats and should be improved to process with the same quality the human data. Additionally, the most relevant combination of multi-modalities of MRI parameters is obtained.

14.1 Plan of Contribution

We summarize the contributions based on methodology and medical application as follows:

1. Based on the research on *mean shift*, we discuss the properties (*e.g.* blurring, noise, mixed blurring and noise, bandwidth parameters) which could influence *mean shift* filtering and how the *mean shift* filtering process is affected by these factors.
2. Verified by exhaustive search of bandwidth parameters, the proposed multi-dimensional *Plug-In* method is able to give the best estimation of optimal global bandwidth parameters based on *mean shift* filtering compared to the mono-dimensional *Plug-In*.
3. We proposed the new automated hybrid segmentation framework which combines *mean shift* filtering and *region growing* segmentation as well as the *PM* method for quantifying the target segmented region.
4. The new automatic segmentation volume-based framework is employed in predicting and estimating the final ischemic infarction based on results from rats' data and preliminary results from human's data. The most favourable combination of multi-modalities of MRI parameters is obtained.

14.2 Perspectives

For future work, we summarize several of the methodological perspectives on *mean shift* algorithm as follows:

1. We studied the noise (Gaussian) and the blurring influence on *mean shift* filtering. More experiments need to be performed using other types of noise and blurring to verify the conclusion.
2. We conclude that *mean shift* is not robust for blurring. Another method can be considered to reduce the blurring effect. Thank to our observations, *mean shift* filtering can be improved to detect the blurring effect in the feature space and adapts its parameters (*i.e.* automatically tunes the bandwidth matrix to fit the blur effect direction in the feature space).
3. PI bandwidth selector is performed in order to optimize bandwidth parameters during *mean shift* filtering based on the three dimensional case (*e.g.* color images and synthesized data set). Multi-dimensional (d = 4, 5, 6) cases need to be conducted by using multi-variate PI methods in order to verify its robustness.

Moreover, we suggest several perspectives concerned with the medical application as follows:

1. We conducted the *PM* framework on a limited number of synthesized data, animal data and human data. More experiments using the proposed *PM* framework need to be performed on real data in order to verify its robustness and efficiency.
2. Optimization of bandwidth is an interesting topic in *PM* framework. By identifying clusters of bandwidth matrices that give good dice results, it should be possible to localize several ranges of bandwidth parameters that will give high quality segmentation results.
3. We will have to compare the *PM* framework with other algorithms (*e.g.* 2D threshold segmentation, adaptive mean shift with high density clustering), including those that involve a learning step such as support vector machine (SVM). Additionally, It will also be interesting to compare the *PM* algorithm based results with results of some experts.

Appendix

Appendix A

Effect of PCA on *mean shift*

Principal component analysis (PCA) is a dimension reduction technique by the number of variables into a few principal components (*e.g.* integrated variables). The main components of the original variables enable reflect most of the information, which is expressed as a linear combination of the original variables.

The PCA aims to find an orthonormal transformation $\mathbf{T}_{PCA}$ to de-correlate $\overline{\mathbf{X}}$: $\overline{\mathbf{Y}} = \mathbf{T}_{PCA}\overline{\mathbf{X}}$, where $\overline{\mathbf{X}}$ is a matrix with zero empirical mean obtained from the sample matrix $\mathbf{X}$ after subtraction the empirical mean of the distribution. Thus, the co-variance matrix of $\overline{\mathbf{Y}}$ is diagonal. As the co-variance matrix $\mathbf{\Sigma}$ of $\overline{\mathbf{X}}$ is symmetrical, we can compute the orthonormal eigenvectors matrix $\mathbf{V}$ which diagonalizes $\mathbf{\Sigma}$.

$$\mathbf{\Sigma} = \mathbf{V}\mathbf{\Lambda}\mathbf{V}^T \tag{A.1}$$

where $\mathbf{\Lambda} = diag\{\lambda_1, \lambda_2, ..., \lambda_d\}$ is the diagonal eigenvalues matrix with $\lambda_1 \geq \lambda_2 \geq ... \geq \lambda_d$. Therefore $\mathbf{T}_{PCA}$ is equal to $\mathbf{V}^T$. As $\mathbf{V}$ is an orthogonal matrix ($\mathbf{V}^T\mathbf{V} = \mathbf{I}$) and as *mean shift* are based on the Mahalanobis distance, we can easily show in equation A.2 that applying a PCA transformation is useless on *mean shift* if no dimension reduction is done.

$$\begin{aligned}
&d_M^2(\mathbf{T}_{PCA}.\mathbf{x}_r, \mathbf{T}_{PCA}.\mathbf{y}_r, \mathbf{H}) \\
&\quad = (\mathbf{T}_{PCA}.\mathbf{x}_r - \mathbf{T}_{PCA}.\mathbf{y}_r)^T\mathbf{H}^{-1}(\mathbf{T}_{PCA}.\mathbf{x}_r - \mathbf{T}_{PCA}.\mathbf{y}_r) \\
&\quad = (\mathbf{x_r} - \mathbf{y}_r)^T\mathbf{T}_{PCA}^T\mathbf{H}^{-1}\mathbf{T}_{PCA}(\mathbf{x}_r - \mathbf{y}_r) \\
&\quad = (\mathbf{x}_r - \mathbf{y}_r)^T\mathbf{T}_{PCA}\mathbf{T}_{PCA}^T\mathbf{H}^{-1}\mathbf{T}_{PCA}\mathbf{T}_{PCA}^T(\mathbf{x}_r - \mathbf{y}_r) \\
&\quad = d_M^2(\mathbf{x}_r, \mathbf{y}_r, \mathbf{H})
\end{aligned} \tag{A.2}$$

Consequently, we do not consider PCA transformations for *mean shift* filtering if no decrease of dimension is done in this thesis any more.

V Bibliography

Bibliography

[Aja-Fernandez 08] S. Aja-Fernandez, Alberola-Lopez & CF. C. Westin. *Noise and signal estimation in magnitude MRI and Rician distributed images: a LMMSE approach*. IEEE Transactions on Image Processing, vol. 17(8), pages 1383–1398, 2008.

[Albers 99] GW. Albers. *Expanding the window for thrombolytic therapy in acute stroke. The potential role of acute MRI for patient selection*. Stroke, vol. 30, pages 2230–2237, 1999.

[Arnaldo 09] G. Arnaldo M. Hayit. *An adaptive mean-shift framework for MRI brain segmentation*. IEEE Transactions on Medical Imaging, vol. 28, page 1238ï£¡1250, 2009.

[Ashok 06] Srinivasan. Ashok, Goyal. Mayank, Azri. FA & Lum. Cheemun. *State-of-the-art imaging of acute stroke1*. Stroke, vol. 26(suppl 1), pages S75–S95, 2006.

[Barash 04] D. Barash D. Comaniciu. *A common framework for nonlinear diffusion, adaptive smoothing, bilateral filtering and mean shift*. Image and Vision Computing, vol. 22, no. 1, pages 73–81, 2004.

[Baron 05] S. Baron JC. Warach. *Imaging*. Stroke, vol. 36, pages 196–199, 2005.

[Baumgartner 05] Christian Baumgartner, Kurt Gautsch, Christian Bï£¡hm & Stephan Felber. *Functional Cluster Analysis of CT Perfusion Maps: A New Tool for Diagnosis of Acute Stroke?* Journal of digital imaging the official journal of the Society for Computer Applications in Radiology, vol. 18, no. 3, pages 219–226, 2005.

[Bowman 84] Adrian W Bowman. *An alternative method of cross-validation for the smoothing of density estimates*. Biometrika, vol. 71, no. 2, pages 353–360, 1984.

[Buades 05] B. Buades A. Coll & JM. Morel. *A Review of Image Denoising Algorithm, with a New One*. Multiscale Modeling & Simulation, vol. 4(2), pages 490–530, 2005.

[Carreira-Perpiï£¡ï£¡n 06] M. ï£¡. Carreira-Perpiï£¡ï£¡n. *Fast nonparametric clustering with Gaussian blurring mean-shift*. In 23rd Int. Conf. Machine Learning (ICML 2006), pages 153–160, 2006.

[Carreira-Perpinan 07] Miguel A. Carreira-Perpinan. *Gaussian mean-shift is an EM algorithm*. IEEE Transactions on Pattern Analysis and Machine Intelligence, vol. 29, no. 5, pages 767–776, 2007.

[Chacï£¡n 09] J E Chacï£¡n & T Duong. *Multivariate plug-in bandwidth selection with unconstrained pilot bandwidth matrices*. Test, vol. 19, no. 2, pages 375–398, 2009.

[Chatterjee 10] Peyman. Chatterjee Priyam. Milanfar. *Is Denoising Dead*. IEEE Transactions on Image Processing, vol. 19(4), pages 895–911, 2010.

[Chauveau 11] F Chauveau, TH Cho, M Perez, M Guichardant, A Riou, P Aguettaz, M Picq, M Lagarde, Y Berthezï£¡ne, N Nighoghossian & et al. *Brain-targeting form of docosahexaenoic acid for experimental stroke treatment: MRI evaluation and anti-oxidant impact*. Current Neurovascular Research, vol. 8, no. 2, pages 95–102, 2011.

[Cheng 95] Y. Cheng. *Mean Shift, Mode Seeking, and Clustering*. IEEE Trans. Pattern Anal. Mach. Intell., vol. 17, no. 8, pages 790–799, 1995.

[Collins 03] Robert T. Collins. *Mean-shift blob tracking through scale space*. In 2003 IEEE Computer Society Conference on Computer Vision and Pattern Recognition, Jun 18-20 2003, volume 2 of *Proceedings of the IEEE Computer Society Conference on Computer Vision and Pattern Recognition*, pages 234–240, Madison, WI, United States, 2003. Institute of Electrical and Electronics Engineers Computer Society.

[Comaniciu 99] D. Comaniciu & P. Meer. *Mean shift analysis and applications*. In Proceedings of the IEEE International Conference on Computer Vision, volume 2, pages 1197–1203, Kerkyra, Greece, 1999.

[Comaniciu 01] D. Comaniciu, V. Ramesh & P. Meer. *The Variable Bandwidth Mean Shift and Data-Driven Scale Selection*. In Proc. 8th Intl. Conf. on Computer Vision, pages 438–445, 2001.

[Comaniciu 02] D. Comaniciu & P. Meer. *Mean shift: A robust approach toward feature space analysis*. IEEE Transactions on Pattern Analysis and Machine Intelligence, vol. 24, no. 5, pages 603–619, 2002.

[Comaniciu 03] D. Comaniciu. *An Algorithm for Data-Driven Bandwidth Selection*. IEEE Trans. Pattern Anal. Mach. Intell., vol. 25, pages 281–288, February 2003.

[Contin 10] Lilian Contin, Christopher Beer, Michael Bynevelt, H J Wittsack & G J Garrido. *Semi-automatic segmentation of core and penumbra regions in acute ischemic stroke: preliminary results*. creactevecombr, pages 5–8, 2010.

[Conturo 05] TE. Conturo, E. Akbudak, MS. Kotys, ML. Chen, SJ. Chun, RM. Hsu, CC. Sweeney & J. Markham. *Arterial input functions for dynamic susceptibility contrast MRI: requirements and signal options.* J Magn Reson Imaging, vol. 22(6), pages 697–703, 2005.

[Dabov 07] Alessandro. Dabov Kostadin. Foi, Vladimir. Katkovnik & Karen Egiazarian. *Image Denoising by Sparse 3-D Transform-Domain*

Collaborative Filtering. IEEE Transactions on Image Processing, vol. 16(8), pages 2080–2095, 2007.

[Diaz 10] NC. Diaz, AV. Gil & MJ. Vargas. *Assessment of the suitability of different random number generators for Monte Carlo simulations in gamma-ray spectrometry*. Applied Radiation and Isotopes, vol. 68(3), pages 469–473, 2010.

[Dice 45] L R Dice. *Measures of the amount of ecologic association between species*. Ecology, vol. 26, no. 3, pages 297–302, 1945.

[Domï£¡nguez 03] Gustavo Fernï£¡ndez Domï£¡nguez, Horst Bischof & Reinhard Beichel. *Fast 3D Mean Shift Filter for CT Images.* In Josef Bigï£¡n & Tomas Gustavsson, editeurs, SCIA, volume 2749 of *Lecture Notes in Computer Science*, pages 438–445. Springer, 2003.

[Duong 03] Martin Duong Tarn ; Hazelton. *Plug-in bandwidth matrices for bivariate kernel density estimation*. Journal of Nonparametric Statistics Volum, vol. 15(1), pages 17–30, 2003.

[Duong 07] T Duong. *ks. Kernel Density Estimation and Kernel Discriminant Analysis for Multivariate Data in R*. J Stat Soft, vol. 21, no. 7, pages 1–16, 2007.

[Efron 79] B Efron. *Bootstrap methods: another look at the jackknife*. Annals of Statistics, vol. 7, no. 1, pages 1–26, 1979.

[Fan 05] Jianping Fan, Guihua Zeng, Mathurin Body & Mohand-Said Hacid. *Seeded region growing: an extensive and comparative study*. Pattern Recognition Letters, vol. 26, no. 8, pages 1139 – 1156, 2005.

[Fashing 05] Mark Fashing & Carlo Tomasi. *Mean shift is a bound optimization*. IEEE Transactions on Pattern Analysis and Machine Intelligence, vol. 27, no. 3, pages 471–474, 2005.

[Fawcett 04] Tom Fawcett. *ROC Graphs : Notes and Practical Considerations for Researchers*. Kluwer Academic Publishers, vol. 1, no. HPL-2003-4, pages 1–38, 2004.

[Feller 68] W. Feller. *The Strong Law of Large Numbers*. An Introduction to Probability Theory and Its Applications 243-245, 1968., vol. 1, pages 243–245, 1968.

[Fernandez-Maloigne 12] Christine Fernandez-Maloigne, Ludovic Macaire & Frï£¡dï£¡rique Robert-Inacio. Advances in color imagingï£¡. Wiley, 2012.

[Filippi 05] N. et al Filippi M. Stefano, editeur. Mr imaging in white matter diseases of the brain and spinal cord. Springer, 2005.

[Fisher 03] M. Fisher. *Recommendations for advancing development of acute stroke therapies: Stroke Therapy Academic Industry Roundtable 3*. Stroke, vol. 34, pages 1539–1546, 2003.

[Freedman 09] D. Freedman & P. Kisilev. *Fast Mean shift by compact density representation*. In 2009 IEEE Computer Society Conference on Computer Vision and Pattern Recognition Workshops, CVPR Workshops 2009, pages 1818–1825, Miami, FL, United states, 2009. IEEE Computer Society.

[Fukunaga 75] K. Fukunaga & L. D. Hostetler. *Estimation of the gradient of a density function with applications in pattern recognition.* IEEE Transaction on Information Theory, vol. 21, no. 1, pages 32–40, 1975.

[Gan 07] Guojun Gan, Chaoqun Ma & Jianhong Wu. Data clustering - theory, algorithms, and applications. SIAM, 2007.

[Gonzalez 11] RG. Gonzalez. Acute ischemic stroke: Imaging and intervention. Springer, 2011.

[Gorry 07] B. Gorry, Z. Chen, K. Hammond, A. Wallace & G. Michaelson. *Using Mean-Shift Tracking Algorithms for Real-Time Tracking of Moving Images on an Autonomous Vehicle Testbed Platform*. In C. Ardil, editeur, Conference of the World-Academy-of-Science-Engineering-and-Technology, pages 356–361, Venice, ITALY, 2007. World Acad Sci, Eng & Tech-Waset.

[Grenier 05a] T. Grenier, C. Revol-Muller, F. Davignon, O. Basset & G. Gimenez. *Multiparametric Smoothing Based On Mean Shift Procedure For Ultrasound Data Segmentation*. In Proceedings of the EUSIPCO'05, pages Article ID cr1461, 4 pages, Antalya, Turkey, 2005.

[Grenier 05b] T. Grenier, C. Revol-Muller, F. Davignon, O. Basset & G. Gimenez. *Variable bandwidth Mean Shift for Smoothing ultrasonic images*. In Proceedings of the EUSIPCO'05, pages Article ID cr1454, 4 pages, Antalya, Turkey, 2005.

[Grenier 06] T. Grenier, C. Revol-Muller & G. Gimenez. *Hybrid approach for multiparametric mean shift filtering*. In Proceedings of the IEEE International Conference on Image Processing, pages 1541–1544, Atlanta, USA, 2006.

[He 09] J. He KM. Sun & XO Tang. *Single image haze removal using dark channel prior*. In Computer Vision and Pattern Recognition, 2009.

[Hjort 05] N. Hjort, K. Butcher, S. M. Davis, C. S. Kidwell, W. J. Koroshetz, J. Rother, P. D. Schellinger, S. Warach & L. Ostergaard. *Magnetic Resonance Imaging Criteria for Thrombolysis in Acute Cerebral Infarct*. Stroke, vol. 36, pages 388–397, 2005.

[Hong 07] Y. Hong, J. Yi & D. Zhao. *Improved mean shift segmentation approach for natural images*. Applied Mathematics and Computation, vol. 185, no. 2, pages 940 – 952, 2007.

[Hua 81] Y Hua LK; Wang. Applications of number theory to numerical analysis. 1981.

[Jacobs 01] MA Jacobs, P Mitsias, H Soltanian-Zadeh, S Santhakumar, A Ghanei, R Hammond, DJ Peck, M Chopp & S Patel. *Multiparametric MRI tissue characterization in clinical stroke with correlation to clinical outcome: part 2.* Stroke: A Journal of Cerebral Circulation, vol. 32, no. 4, pages 950–957, 2001.

[Jones 96] M. Jones, J. Marron & S. Sheather. *A Brief Survey of Bandwidth Selection for Density Estimation*. J. Amer. Statist. Assoc, vol. 91, pages 401–407, 1996.

[Kalos 08] PA. Kalos MH. Whitlock. Monte carlo methods. Wiley-VCH Verlag GmbH & Co. KGaA, 2008.

[Kervrann 06] Jerome Kervrann Charles. Boulanger. *Optimal Spatial Adaptation for Patch-Based Image Denoising*. IEEE Transactions on Image Processing, vol. 15(10), pages 2866–2878, 2006.

[Kidwell 04] CS. Kidwell, JR. Alger & GL. Saver. *Evolving Paradigms in Neuroimaging of the Ischemic Penumbra*. Stroke, vol. 35, pages 2662–2665, 2004.

[Kuipers 74] H Kuipers L. Niederreiter. Uniform distribution of sequences. A WILEY-INTERSCIENCE PUBLICATION, 1974.

[Kurimo 09] Leena. Kurimo Eero. Lepissto, Jarno. Nikkanen, Juuso. Gren & Iivari. Kunttu. *The Effectof Motion Blur and Signal noise on Image Quality in Low Light Imaging*. In Scandinavian Conference on Image Analysis, 2009.

[Li 04] Wu Li, Jie Tian, Enzhong Li & Jianping Dai. *Robust unsupervised segmentation of infarct lesion from diffusion tensor MR images using multiscale statistical classification and partial volume voxel reclassification*. NeuroImage, vol. 23, no. 4, pages 1507 – 1518, 2004.

[Li 10] T Li, S. Camarasu-Pop, T. Glatard, T. Grenier & H. Benoit-Cattin. *Optimization of Mean-Shift scale parameters on the EGEE grid*. In Studies in health technology and informatics, Proceedings of Healthgrid 2010, volume 159, pages 203–214, 2010.

[Li 11] T Li, T. Grenier & H. Benoit-Cattin. *Color space influence on mean shift filtering*. In Proceedings - International Conference on Image Processing, ICIP, pages 1469 – 1472, Brussels, Belgium, 2011.

[Lo 05] EH. Lo, MA. Moskowitz & TP. Jacobs. *Exciting, Radical, Suicidal: How Brain Cells Die After Stroke*. Stroke, vol. 36, pages 189–192, 2005.

[Mezzapesa 06] DM. Mezzapesa, M. Petruzzellis, V. Lucivero, M. Prontera, A. Tinelli, M. Sancilio, A. Carella & F. Federico. *Multimodal MR examination in acute ischemic stroke.* Neuroradiology, vol. 48(4), pages 238–246, 2006.

[Murphy 06] B D Murphy, A J Fox, D H Lee, D J Sahlas, S E Black, M J Hogan, S B Coutts, A M Demchuk, M Goyal, R I Aviv & et al. *Identification of penumbra and infarct in acute ischemic stroke using computed tomography perfusion-derived blood flow and blood volume measurements.* Stroke: A Journal of Cerebral Circulation, vol. 37, no. 7, pages 1771–1777, 2006.

[Niederreiter 92] H. Niederreiter. Random number generation and quasi-monte carlo methods. SOCIETY FOR INDUSTRIAL AND APPLIED MATHEMATICS, 1992.

[Nishimura 96] D.G. Nishimura. Principles of magnetic resonance imaging. Stanford University, 1996.

[Olivot 09] M. Olivot JM. Mlynash & VN. et al. Thijs. *Relationships between cerebral perfusion and reversibility of acute diffusion lesions in DEFUSE: insights from RADAR.* Stroke, vol. 40(5), pages 1692–1697, 2009.

[Ostergaard 05] L. Ostergaard. *Principles of cerebral perfusion imaging by bolus tracking*. JOURNAL OF MAGNETIC RESONANCE IMAGING, vol. 22(6), pages 710–717, 2005.

[Parzen 62] E. Parzen. *On estimation of a probality density function and mode*. Annals of Mathematical Statistics, vol. 33, pages 1065–1076, 1962.

[Prakash 08] Bhanu K N Prakash, Varsha Gupta, Hu Jianbo & Wieslaw L Nowinski. *Automatic processing of diffusion-weighted ischemic stroke images based on divergence measures: slice and hemisphere identification, and stroke region segmentation*. International Journal of Computer Assisted Radiology and Surgery, vol. 3, no. 6, pages 559–570, 2008.

[Puetter 05] TR. Puetter RC. Gosnell & Amos. Yahil. *DIGITAL IMAGE RECONSTRUCTION: Deblurring and Denoising*. Annu. Rev. Astron. Astrophys, vol. 43, page 139ï£¡194, 2005.

[Rao 09] S. Rao, A. de Medeiros Martins & J. C. Principe. *Mean shift: An information theoretic perspective*. Pattern Recognition Letters, vol. 30, no. 3, pages 222–230, 2009.

[Ritzenthaler 05] Thomas. Ritzenthaler. Etude sequentielle en irm multimodale des parametres hemodynamiques au sein de la zone a risque lors dï£¡un accident ischemique cerebral du territoire carotidien. Master's thesis, L'Institut des sciences et techniques de l'ingï£¡nieur de Lyon, 2005.

[Rosenblatt 56] Murray Rosenblatt. *Remarks on Some Nonparametric Estimates of a Density Function*. Annals of Mathematical Statistics, vol. 27, pages 832–837, 1956.

[Rosso 09] Charlotte Rosso, Nidiyare Hevia-Montiel, Sandrine Deltour, Eric Bardinet, Didier Dormont, Sophie Crozier, Sylvain Baillet & Yves Samson. *Prediction of Infarct Growth Based on Apparent Diffusion Coefficients: Penumbral Assessment without Intravenous Contrast Material*. RADIOLOGY, vol. 250, no. 1, pages 184–192, JAN 2009.

[Rudemo 82] M Rudemo. *Empirical Choice of Histograms and Kernel Density Estimators*. Scandinavian Journal of Statistics, vol. 9, no. 2, pages 65–78, 1982.

[Scholkopf 99] B. Scholkopf, S. Mika, C.J.C. Burges, P. Knirsch, K.-R. Muller, G. Ratsch & A.J. Smola. *Input space versus feature space in kernel-based methods*. Neural Networks, IEEE Transactions on, vol. 10, no. 5, pages 1000 –1017, sep 1999.

[Scott 77] RA Scott DW. Tapia & JR. Thompson. *Kernel density estimation revisited*. Nonlinear Analysis, Theory, Methods and Applications, vol. 1, pages 339–372, 1977.

[Sen 11] Souvik. Sen. Magnetic resonance imaging in acute stroke. 2011.

[Sheather 91] S. J. Sheather & M. C. Jones. *A reliable data-based bandwidth selection method for kernel density estimation*. J.Roy.Statist.Soc.Ser B, vol. 53, pages 683–690, 1991.

[Shen 03] Qiang Shen, Xiangjun Meng, Marc Fisher, Christopher H Sotak & Timothy Q Duong. *Pixel-by-pixel spatiotemporal progression of focal ischemia derived using quantitative perfusion and diffusion imaging*. Journal of cerebral blood flow and metabolism official journal of the International Society of Cerebral Blood Flow and Metabolism, vol. 23, no. 12, pages 1479–1488, 2003.

[Sobesky 05] Jan. et al Sobesky. *Does the mismatch match the penumbra? Magnetic resonance imaging and positron emission tomography in early ischemic stroke.* Stroke: A Journal of Cerebral Circulation, vol. 36(5), pages 980–985, 2005.

[Swanson 05] Scott Swanson. *MR Imaging in White Matter Diseases of the Brain and Spinal Cord.* Medical Radiology, vol. 1, pages 83–91, 2005.

[Takasawa 08] P. et al. Takasawa Massashi. Simon Jones. *How Reliable Is Perfusion MR in Acute Stroke?* Stroke, vol. 39(3), pages 870–877, 2008.

[Tek 01] H. Tek, D. Comaniciu & J.-P. Williams. *Vessel detection by mean shift based ray propagation*. In Workshop on Mathematical Methods in Biomedical Image Analysis, pages 228–235, Kauai, HI, 2001.

[Train 00] Kenneth Train. *Halton Sequences for Mixed Logit*. Power, pages 1–18, 2000.

[Wand 95] M.P. Wand & M.C. Jones. Kernel smoothing. Monographs on statistics and applied probability. Chapman & Hall, 1995.

[Wang 02] Z. Wang, A. C. Bovik & L. Lu. *Why is image quality assessment so difficult?* In ICASSP, IEEE International Conference on Acoustics, Speech and Signal Processing - Proceedings, volume 4, pages IV/3313–IV/3316, Orlando, FL, United states, 2002. Institute of Electrical and Electronics Engineers Inc.

[Wang 04] Z. Wang, A.C. Bovik, H.R. Sheikh & E.P. Simoncelli. *Image quality assessment: from error visibility to structural similarity*. IEEE Transactions on Image Processing, vol. 13, no. 4, pages 600 –612, april 2004.

[Wang 07] Ping Wang, Dongryeol Lee, Alexander Gray & James Rehg. *Fast mean shift with accurate and stable convergence.* In Proceedings of AISTATS 2007, 2007.

[Wang 09] Z. Wang & A. C. Bovik. *Mean squared error: Lot it or leave it? A new look at signal fidelity measures*. IEEE Signal Processing Magazine, vol. 26, no. 1, pages 98–117, 2009.

[Wu 01] O Wu, WJ Koroshetz, L Ostergaard, FS Buonanno, WA Copen, RG Gonzalez, G Rordorf, BR Rosen, LH Schwamm, RM Weisskoff & et al. *Predicting tissue outcome in acute human cerebral ischemia using combined diffusion- and perfusion-weighted MR imaging*. Stroke: A Journal of Cerebral Circulation, vol. 32, no. 4, pages 933–942, 2001.

[Wu 12] Ona Wu. *Evaluating effects of normobaric oxygen therapy in acute stroke with MRI-based predictive models*. BioMed Central, vol. 2(5), pages 1186–2045, 2012.

[Yoder 04] Y. Yoder DA. Zhao, CB. Paschal & JM. Fitzpatrick. *MRI simulator with object-specific field map calculations*. Magn Reson Imaging, vol. 22, pages 315–328, 2004.

[Zafar 08] Sajjad. Zafar. *Perfusion imaging in ischaemic stroke*. Journal of Pakistan Medical Association, vol. 58(7), pages 391–394, 2008.

[Zhang 01] Y. Zhang, M. Brady & S. Smith. *Segmentation of brain MR images through a hidden Markov random field model and the expectation-maximization algorithm.* IEEE Trans Med Imaging, vol. 20, pages 45–57, 2001.

[Zhang 06] Xibin Zhang, Robert D. Brooks & Maxwell L. King. *A Bayesian approach to bandwidth selection for multivariate kernel regression with an application to state-price density estimation*. Journal of Econometrics, vol. 153, no. 1, pages 21 – 32, 2006.

[Zucker 76] SW Zucker. *Region growing: Childhood and Adolescence*. Computer Graphics and Image Processing, vol. 5(3), pages 382–399, 1976.

FOLIO ADMINISTRATIF
THÈSE SOUTENUE DEVANT L'INSTITUT NATIONAL DES SCIENCES APPLIQUÉES DE LYON

NOM : LI **DATE DE SOUTENANCE** : 04/04/12
PRÉNOM : Ting

TITRE : Contributions to Mean Shift filtering and segmentation, Applications to MRI ischemic data.

NATURE : Doctorat **NUMÉRO D'ORDRE** : 2012-****-****
FORMATION DOCTORALE : Sciences de l'Information, des Dispositifs et des Systèmes
FILIÈRE : Instrumentation, Système, Signal & Image

COTE B.I.U. LYON : ****** **CLASSE** : ******

RÉSUMÉ :
De plus en plus souvent, les études médicales utilisent simultanément de multiples modalités d'acquisition d'image, produisant ainsi des données multidimensionnelles comportant un grand nombre d'informations dont l'interprétation et le traitement deviennent délicats. Par exemple, les études sur l'ischémie cérébrale; se basant sur la combinaison de plusieurs images IRM provenant de différentes séquences d'acquisition pour prédire l'évolution de la zone nécrosée, donnent de bien meilleurs résultats que celles basées sur une seule image. Ces approches nécessitent cependant la mise en oeuvre d'algorithmes complexes pour réaliser les opérations de filtrage, de segmentation et de classification.
Une des approches robustes pour répondre à ces problèmes de traitements de données multidimensionnelles est le *mean shift*. Cette approche est basée sur l'analyse de l'espace des caractéristiques et l'estimation non-paramétrique par noyau de la densité de probabilité. Dans cette thèse, nous étudions les paramètres qui influencent les résultats du *mean shift* et nous cherchons à optimiser leur choix. Nous examinons notamment l'effet du bruit et du flou dans l'espace des caractéristiques et comment le *mean shift* doit être paramétré pour être optimiser le débruitage et la réduction du flou. Le succès du *mean shift* est principalement dû au réglage intuitif de ses paramètres. Ces paramètres représentent l'échelle à laquelle le *mean shift* analyse chacune des dimensions. La méthode du *plug-in* (PI) monodimensionnel est fréquemment utilisée en filtrage *mean shift* pour, dans le cadre de l'estimation non-paramétrique par noyau, approximer le paramètre d'échelle optimal. Nous proposons l'utilisation multidimensionnelle du PI pour le filtrage *mean shift* et nous évaluons l'intérêt des matrices d'échelle diagonales et pleines calculées à partir des règles du PI multidimensionnelle sur des images de synthèses et naturelles.
Enfin, nous proposons une méthode de segmentation automatique et volumique combinant le filtrage *mean shift* et la croissance de région ainsi qu'une optimisation basée sur les cartes de probabilité. Cette approche est d'abord étudiée sur des données synthétiques. Elle est ensuite mise en oeuvre sur des données réelles issues d'études sur l'ischémie cérébrale chez le rat et l'homme. L'objectif est d'étudier l'efficacité de l'approche proposée à prédire l'évolution de la zone de pénombre plusieurs jours après l'accident vasculaire et ce, à partir des IRM réalisées peu de temps après la survenue de cet accident. Par rapport aux segmentations manuelles réalisées par des experts médicaux plusieurs jours après l'accident, les résultats obtenus sur les données de rats mesurés avec le critère de DICE sont prometteurs (DICE$= 0.8$). Ces mêmes résultats sont plus mitigés sur les données humaines (DICE$= 0.53$). Toujours en utilisant le coefficient DICE, nous déterminons la combinaison d'images IRM conduisant à la meilleure prédiction.

MOTS CLÉ : filtrage *mean shift*, segmentation par *croissance de région*, *carte de probabilité*, optimisation matrice d'échelle, IRM, ischémie cérébrale.

LABORATOIRE DE RECHERCHES :
CREATIS-LRMN, UMR CNRS 5520, U630 Inserm

DIRECTEURS DE THÈSE : Thomas Grenier, Hugues Benoit-Cattin.

PRÉSIDENT DU JURY : Philippe Bolon.
COMPOSITION DU JURY : Pierre Goutou, Ludovic Macaire, Marlène Wiart, Philippe Bolon, Thomas Grenier, Hugues Benoit-Cattin.